

**MEASUREMENT OF LOW CONCENTRATION AND  
NANO QUANTITY HYDROGEN SULFIDE BY CARBON  
NANOTUBE**

A Dissertation Submitted to the  
College of Graduate Studies and Research  
In Partial Fulfillment of the Requirements for the Degree of  
**Doctor of Philosophy**

In the  
Division of Biomedical Engineering  
University of Saskatchewan  
Saskatoon, Saskatchewan  
Canada

By  
**Xiaochu Wu**

© Copyright Xiaochu Wu, December 2007. All rights reserved.

## **PERMISSION TO USE**

In presenting this dissertation in partial fulfilment of the requirements for a Doctor of Philosophy degree from the University of Saskatchewan, the author agrees that the Libraries of this University may make it freely available for inspection. The author further agrees that permission for copying of this dissertation in any manner, in whole or in part, for scholarly purposes may be granted by the professor or professors who supervised the dissertation work or, in their absence, by the Head of the Department or the Dean of the College in which the dissertation work was done. It is understood that any copying or publication or use of this dissertation or parts thereof for financial gain shall not be allowed without the author's written permission. It is also understood that due recognition shall be given to the author and to the University of Saskatchewan in any scholarly use which may be made of any material in this dissertation.

Requests for permission to copy or to make other use of material in this dissertation in whole or part should be addressed to:

Head of the Division of Biomedical Engineering

University of Saskatchewan

Saskatoon, Saskatchewan S7N 5A9 CANADA

## ACKNOWLEDGEMENTS

My years in PhD study have been exciting, challenging, and above all, rewarding, and for all of these I have my supervisors to thank.

My primary supervisor, Dr. W. J. (Chris) Zhang, has always given me freedom as well as effective and efficient direction, critical comments, and constructive suggestions on my research work. His willingness to treat students as colleagues and not as subordinates is a unique and extraordinary trait, and his kindness and helpfulness will not be forgotten throughout my life. The experience of working with him through the formative years of my career and of having him as a supervisor has been incomparable.

My co-supervisor, Dr. Rui Wang, has always given me strong support in the medical aspects of this work. I am happy to have had the opportunity to receive his excellent advice, and his help contributed greatly to success of this work. His knowledge on H<sub>2</sub>S is incredibly high, and his attitude in making everything described accurately is extremely valuable to my career.

I would thank my committee members for their suggestions and support. I especially thank Dr. R. Sammynaiken for his excellent advice both on this work and also for facilitating my access to the Raman spectroscopy at the Saskatchewan Structural Sciences Center. His knowledge of surface chemistry and materials science is enormous.

I also want to thank Ms. D. Q. Wu for her kind collaboration in the beginning of this work, Dr. W. Yang for preparing the hydrogen sulfide solutions and serum samples, Dr. Q. Meng for helping to measure the proteins in the serum, and Dr. Q. Yang for providing carbon nanotubes.

I would also like to thank Ms. Wanda Drury and Mr. Kirk Backstrom for proof reading this dissertation for structural and grammatical mistakes.

Finally, thank you to my family, who I can honestly say have loved, supported, and encouraged me over the whole period of my studies. I could not have asked for more perfect persons with whom to share my work, my thoughts, and my life.

## ABSTRACT

Traditionally, hydrogen sulfide (H<sub>2</sub>S) has been regarded as toxic. It can affect the various human systems and even cause death. However, research in the 1990's has shown that H<sub>2</sub>S can be endogenously generated by many cells and tissues in mammalian bodies, and that H<sub>2</sub>S also may play physiological roles such as those of neuromodulator and vasorelaxant in the biological system. As such, the precise measurement of the amount of H<sub>2</sub>S in a mammalian body has generated researchers' strong interest. The ultimate goal of such a measurement should be conducted *in-vivo* and in real time.

The existing methods for H<sub>2</sub>S measurement require both a large quantity of tissue samples and a complex procedure, so they are not highly practicable for the purpose of achieving the aforementioned goal. In this dissertation, a new method that uses carbon nanotube as an absorbent or transducer and laser-based microscopy techniques (Raman and confocal laser scanning microscopy) as signal excitation and acquisition is proposed and developed. Experimental studies are described of using this new method for analysis of both distilled water samples and serum samples in which a group of proteins are present.

The study concludes that the new method (1) can measure H<sub>2</sub>S in water solutions down to a low level of concentration of 10 μM, (2) can measure H<sub>2</sub>S in sera down to a low concentration of approximately 20 μM), and (3) has a high feasibility for being used

in the clinical context. Regarding (3), this is confirmed by presenting a control system that allows the laser microscopy to track carbon nanotube in a solution that has Brownian motion.

While not having reached the ultimate goal as mentioned above, this work advances the state-of-the-art of the measurement of low concentration and nano-quantity of H<sub>2</sub>S in water and serum samples, in particular providing a promise toward a real-time and *in-vivo* H<sub>2</sub>S measurement.

# TABLE OF CONTENTS

PERMISSION TO USE .....	i
ACKNOWLEDGEMENTS .....	ii
ABSTRACT .....	iv
LIST OF ABBREVIATIONS .....	xv
CHAPTER 1 .....	1
INTRODUCTION .....	1
1.1 Background and Motivation.....	1
1.1.1 Hydrogen Sulfide .....	3
1.1.2 Endogenously Generated Hydrogen Sulfide and Metabolism .....	8
1.1.3 Physiological Effects of Hydrogen Sulfide.....	13
1.1.4 Significance of Measurement of Low Concentration Hydrogen Sulfide.....	16
1.2 Existing Hydrogen Sulfide Measurement Methods .....	17
1.2.1 Chromatography.....	17
1.2.2 Spectrophotometry .....	19
1.2.3 Sulfide Ion-Specific Electrode .....	21
1.2.4 A New Method for Hydrogen Sulfide Measurement.....	23
CHAPTER 2 .....	27
BACKGROUND KNOWLEDGE .....	27
2.1 Introduction .....	27

2.2 Activated Carbon .....	28
2.3 Carbon Nanotube .....	32
2.4 Blood and Serum.....	35
2.5 Confocal Laser Scanning Microscopy .....	38
2.6 Raman Microscopy .....	40
2.7 Adhesion .....	42
2.7.1 Adhesion Theory.....	42
2.7.1.1 Mechanical Theory.....	43
2.7.1.2 Electrostatic Theory .....	44
2.7.1.3 Diffusion Theory .....	45
2.7.1.4 Adsorption Theory .....	46
2.7.1.5 Summary .....	48
2.7.2 The Structure of Materials in Adhesion .....	49
2.7.3 Adhesion between Biological and Inorganic Interface .....	50
2.8 Brownian Motion .....	53
2.9 Feedback Control System .....	56
CHAPTER 3 .....	61
USING CARBON NANOTUBE TO ADSORB HYDROGEN SULFIDE IN WATER SOLUTION.....	61
3.1 Introduction .....	61
3.2 Materials and Methods.....	62
3.2.1 Carbon Nanotube Acquisition.....	62



3.2.2 H <sub>2</sub> S Preparation.....	66
3.2.3 Data Acquisition .....	67
3.2.4 Procedure.....	67
3.3 Results and Discussion.....	68
3.3.1 Results from Raman Microscopy.....	69
3.3.2 Results from Laser Scanning Microscopy .....	70
3.3.3 Binding of Carbon Nanotube and H <sub>2</sub> S in H <sub>2</sub> S Water Solutions .....	71
3.3.4 Statistic Analysis of the Results from Laser Scanning Microscopy .....	72
3.3.5 Mechanism of the Adsorption of H <sub>2</sub> S with Carbon Nanotube.....	75
3.4 Related Work .....	79
3.5 Conclusions .....	80
CHAPTER 4 .....	82
MEASUREMENT OF HYDROGEN SULFIDE IN SERUM USING CARBON NANOTUBES .....	82
4.1 Introduction.....	82
4.2 Materials and Methods.....	83
4.2.1 Preparation of Carbon Nanotubes .....	84
4.2.2 Measurement of Proteins in the Serum .....	84
4.2.3 Confocal Laser Scanning Microscopy Measurement .....	85
4.2.4 Raman Microscopy Measurement.....	86
4.2.5 Raman Microscopy Measurement of Hemoglobin Samples.....	87
4.3 Results.....	88

4.3.1 Serum Measurement .....	88
4.3.2 Confocal Laser Scanning Microscopy Measurement .....	90
4.3.3 Raman Microscopy Measurement.....	95
4.3.4 Raman Microscopy Measurement of Hemoglobin .....	96
4.4 Discussion .....	99
4.4.1 The Binding of Carbon Nanotube and H <sub>2</sub> S in Sera.....	99
4.4.2 The Binding of Hemoglobin and Carbon Nanotubes in Water Solution .....	101
4.5 Related Work .....	102
4.6 Conclusion .....	103
CHAPTER 5 .....	105
TRACKING OF A SINGLE NANO-PARTICLE .....	105
5.1 Introduction.....	105
5.2 Conceptual Design of the Controller.....	107
5.3 Logical Design of the Controller .....	111
5.4 Laser Scanning Microscopy Implementation.....	119
5.5 Evaluation of the Control System Based on Simulation.....	121
5.6 Related Work .....	132
5.7 Conclusion .....	133
CHAPTER 6 .....	134
CONCLUSIONS AND FUTURE WORK .....	134
6.1 Overview .....	134
6.2 Conclusions.....	136

6.3 Contributions.....	137
6.4 Future Work.....	138
REFERENCES.....	141
APPENDIX A: MOST LIKELIHOOD ESTIMATOR .....	156
APPENDIX B: MATLAB SIMULATION .....	159
A Plot the simulation in x direction .....	159
B Plot the simulation in y direction .....	160
C Plot the simulation in z direction.....	161
D Plot the simulation speed in XY plane.....	162
E Plot the simulation in x direction.....	163
F Plot the simulation error in XY plane.....	165
G Plot the simulation error in z direction.....	166

## LIST OF TABLES

Table 1.1: Some Relevant Chemical and Physical Properties of H <sub>2</sub> S .....	4
Table 1.2: Source Tissues for H <sub>2</sub> S Production in Mammals.....	10
Table 1.3: The H <sub>2</sub> S Content in Rats' Tissues.....	10
Table 1.4: Comparison of the Current Methods for H <sub>2</sub> S Measurement.....	23
Table 2.1: Properties of Carbon Nanotube.....	33
Table 2.2: Serum Constituents .....	36
Table 3.1: Carbon Nanotube Growth Conditions. ....	64
Table 3.2: ANOVA for Linear Relationship between H <sub>2</sub> S Water Solution Concentrations and Fluorescence Intensities .....	72
Table 4.1: Protein Quantities Before and After the Serum was Treated by Carbon Nanotubes .....	89
Table 4.2: ANOVA for Linear Relationship between H <sub>2</sub> S Concentrations in Sera and Fluorescence Intensities.....	92

## LIST OF FIGURES

Figure 1.1: The approximate solubility of hydrogen sulfide as a function of the pH.....	6
Figure 1.2: Endogenous enzymatic production and metabolism of H <sub>2</sub> S .....	11
Figure 1.3: Endogenous nonenzymatic production of H <sub>2</sub> S.....	12
Figure 1.4: Hypothesized scheme of the interactions of H <sub>2</sub> S and NO in vascular tissues .....	15
Figure 1.5: Distribution of analytes between phases. ....	19
Figure 1.6: Circular bending of a cantilever induced by a differential stress .....	24
Figure 2.1: Schematic representation of the different types of pores in an activated carbon particle .....	29
Figure 2.2: Working principle of confocal laser scanning microscopy .....	39
Figure 2.3: Simplified Raman energy level diagram .....	41
Figure 2.4: Schematic view of the attachment of proteins to carbon nanotubes .....	53
Figure 2.5: General configuration of a feedback control system. ....	57
Figure 2.6: State-space control system. ....	58
Figure 3.1: Chemical vapor deposition system.....	63
Figure 3.2: TEM image of carbon nanotubes.....	65
Figure 3.3: Raman luminescence of carbon nanotube treated with different concentrations of H <sub>2</sub> S in water .....	69

Figure 3.4: Confocal laser scanning microscopy fluorescence of the carbon nanotubes treated with distilled water and with different concentrations of H <sub>2</sub> S in water .....	70
Figure 3.5: Line fit plot in H <sub>2</sub> S water solution.....	73
Figure 3.6: Residual plot in H <sub>2</sub> S water solution.....	73
Figure 3.7: Normal probability plot in H <sub>2</sub> S water solution.....	74
Figure 3.8: TEM image of carbon nanotubes after adsorption of H <sub>2</sub> S.....	78
Figure 4.1: Laser scanning microscopy fluorescence response of carbon nanotubes treated with the serum and distilled water .....	90
Figure 4.2: Laser scanning microscopy fluorescence intensities of the carbon nanotubes treated with the serum and distilled water .....	91
Figure 4.3: Line fit plot of H <sub>2</sub> S in sera.....	93
Figure 4.4: Residual plot of H <sub>2</sub> S in sera.....	93
Figure 4.5: Normal probability plot of H <sub>2</sub> S in sera.....	94
Figure 4.6: Raman luminescence response of carbon nanotubes treated with difference concentrations of H <sub>2</sub> S in sera.....	95
Figure 4.7: Raman luminescence responses of carbon nanotubes treated with distilled water and different concentrations of hemoglobin .....	97
Figure 4.8: Raman spectrum responses of carbon nanotubes treated with distilled water and different concentrations of hemoglobin water solution .....	98
Figure 4.9: Enlarged Raman spectrum response of carbon nanotubes treated with distilled water and different concentrations of hemoglobin water solution .....	99

Figure 5.1: The relation among laser, fluid, and particle.....	108
Figure 5.2: Obtaining the strongest intensity of the particle.....	110
Figure 5.3: Laser tracking of the particle in the X-Y coordinate plane.....	112
Figure 5.4: Laser scanning microscopy design for small particle tracking.....	121
Figure 5.5: X-coordinate of the positions of the laser point and the particle.....	126
Figure 5.6: Y-coordinate of the positions of the laser point and the particle.....	127
Figure 5.7: Z-coordinate of the positions of the laser point and the particle.....	128
Figure 5.8: Position error of the control system in the XY plane.....	129
Figure 5.9: The position error of the control system in the Z direction.....	130
Figure 5.10: Velocity of the laser for tracking the particle in the XY plane.....	131
Figure 5.11: Velocity of the stage for tracking the particle in the Z direction.....	132

## LIST OF ABBREVIATIONS

ACP	: Acid Phosphatase
ACTH	: AdrenoCorticoTropic Hormone
AFM	: Atomic Force Microscopy
ALP	: Alkaline Phosphatase
ANOVA	: ANalysis of Variance
AST	: Aspartate Aminotransferase
ATP	: Adenosine Triphosphate
CBS	: <i>Cystathionine b-Synthase</i>
CCD	: Charge-Coupled semiconductor Device
CK	: Creatine Kinase
CNTs	: Carbon Nanotubes
CNx MWNTs	: Nitrogen-doped Multi-Walled Carbon Nanotubes
CSE	: <i>Cystathionine gamma-Lyase</i>
CO	: Carbon Monoxide
COPD	: Chronic Obstructive Pulmonary Disease
df	: degrees of freedom
DNA	: DeoxyriboNucleic Acid
EELS	: Electrical Energy Loss Spectrum
EDAC	: <i>N-ethyl-N'-(3-dimethylaminopropyl) carbodiimide hydrochloride</i>



EDS	: Energy Dispersive X-ray Spectrometers
GC/MS	: Gas Chromatography/Mass Spectroscopy
GH	: Growth Hormone
GVF	: Generalized Valence Force
H <sub>2</sub> S	: Hydrogen Sulfide
HSA	: Human Serum Albumin
K <sub>ATP</sub> channels	: ATP-sensitive potassium channels
LD	: Lactate Dehydrogenase
MPECVD	: Microwave Plasma Enhanced Chemical Vapor Deposition
MWCNTs	: Multi-Walled Carbon Nanotubes
NHS	: <i>N-hydroxysuccinimide</i>
NO	: Nitric Oxide
PBS	: Phosphate Buffered Saline
PMT	: Photomultiplier
ppm	: part per million
PTH	: ParaThyroid Hormone
sccm	: Standard Cubic Centimeters per Minute
SWNTs	: Single-Walled Nanotubes
TEM	: Transmission Electron Microscopy
TSH	: Thyroid Stimulating Hormone

# CHAPTER 1

## INTRODUCTION

### 1.1 Background and Motivation

At standard temperature and pressure hydrogen sulfide is a colourless and flammable gas. The environmental sources of H<sub>2</sub>S are from nature, anthropogeny, and industry. Traditionally, it has been regarded as a poisonous gas at high concentrations. Therefore, most previous studies on H<sub>2</sub>S were devoted to its toxic effects. However, recently there has been increasing evidence showing that endogenously generated H<sub>2</sub>S in specific mammalian tissues has some physiological effects such as those of neuromodulator and vasorelaxant in a membrane receptor-independent manner, and it has thereby been named the third gasotransmitter after nitric oxide (NO) and carbon monoxide (CO) [Wang, 2004]. While the three gasotransmitters share many features in their production and function, they perform their tasks in unique ways.

H<sub>2</sub>S can be measured both in the circulatory blood and in isolated tissues and cells. For example, rat blood contains about 50 μM H<sub>2</sub>S, while human blood contains about 10-100 μM H<sub>2</sub>S [Wang, 2004]. Higher concentrations (60-150 μM) occur in the rat brain homogenates [Wang, 2004]. These findings increase interest in the roles of H<sub>2</sub>S

in mammalian bodies, especially the physiological and pathological roles of endogenous H<sub>2</sub>S. In order to understand the functions of endogenous H<sub>2</sub>S, accurate measurement of low concentration H<sub>2</sub>S is a must. Furthermore, this measurement desirably should be in real time and non-invasive (or less-invasive).

Currently, there are several H<sub>2</sub>S measurement techniques such as spectrophotometry, chromatography, and ion-selective electrode. These techniques are derived from the industrial measurement of H<sub>2</sub>S pollution in the environment, and thus are not suitable for the measurement of endogenously generated H<sub>2</sub>S. These techniques are usually invasive and require a bulky quantity of tissues. Further, the process for applying these traditional techniques to tissue samples is very complex. Some of them require (1) removing tissues from the mammalian bodies and homogenizing, (2) reacting homogenized tissues with the *L-cysteine* to generate hydrogen sulfide, and (3) measuring the generated hydrogen sulfide [Wu et al., 2005]. For the ion-selective electrode measurement technique, relatively a large amount of blood samples are needed.

The purpose of the work described in this dissertation is to apply a new non-invasive or less invasive method for measuring low concentration H<sub>2</sub>S. In the following sections of this chapter, we will discuss H<sub>2</sub>S and its effects on the mammalian body, and the necessity for establishing a new measurement method.

### 1.1.1 Hydrogen Sulfide

Hydrogen sulfide is also known as dihydrogen monosulfide, dihydrogen sulfide, hydrosulfuric acid, sewer gas, stink damp, sulfureted hydrogen, and sulfur hydride. It is a colourless gas and has a strong odor of rotten eggs [Winder et al., 1933; Smith et al., 1979]. Hydrogen sulfide has a structure similar to that of water; however, since sulfur is not nearly as electronegative as oxygen, hydrogen sulfide is not nearly as polar as water. Because of this, comparatively weak intermolecular forces exist for H<sub>2</sub>S and the melting and boiling points are much lower than they are for water. Some relevant chemical and physical properties of hydrogen sulfide are shown in Table 1.1 [HSDB, 1998].

Table 1.1: Some Relevant Chemical and Physical Properties of H<sub>2</sub>S\*.

Property	Value (Unit)
CAS registry number**	7783-06-4
Molecular formula**	H <sub>2</sub> S
Molecular weight	34.08 g/ mol
Vapor pressure	15,600 mm Hg at 25 °C
Density	1.5392 g/L at 0 °C, 760 mm Hg
Boiling point	-60.33 °C
Water solubility	3980 mg/L at 20 °C
Log K <sub>ow</sub>	Not applicable
Dissociation constants	pKa1 = 7.04; pKa2 = 11.96
Conversion factor	1 ppm = 1.39 mg/m <sup>3</sup>

\* [NSDB, 1998]

\*\* no unit

Hydrogen sulfide is soluble in certain polar organic solvents, notably methanol, acetone, propylene carbonate, sulfolane, tributyl phosphate, various glycols, and glycol ethers [HSDB, 1998], and it is also soluble in glycerol, gasoline, kerosene, carbon disulfide, and crude oil. Although hydrogen sulfide is reported elsewhere to be fairly water soluble, Milby et al. [1999] indicated that H<sub>2</sub>S is only moderately water soluble. Inorganic aqueous solutions of H<sub>2</sub>S are not stable; absorbed oxygen causes the formation

of elemental sulfur and the solutions rapidly become turbid [HSDB, 1998]. However, organic solutions of H<sub>2</sub>S may reasonably be stable according to Zhao et al. [2003].

Once dissolved in water, H<sub>2</sub>S is involved in a series of chemical reactions, and they are (1) the dissociation of the molecular H<sub>2</sub>S to the HS<sup>-</sup> ion, (2) the dissociation of the HS<sup>-</sup> ion to the S<sup>2-</sup> ion, and (3) the self ionization of water. These reactions are described with equations below [Carroll, 1989].



The effect of pH on the solubility of H<sub>2</sub>S solution is shown in Figure 1.1. At low pH (acidic solutions), the predominant form of the solution is the molecular H<sub>2</sub>S. At a pH of slightly less than 7, there are equal amounts of H<sub>2</sub>S and HS<sup>-</sup> in the solution. At pH > 7, the concentration of the HS<sup>-</sup> increases rapidly and at pH = 8, HS<sup>-</sup> is about ten times that of the molecular H<sub>2</sub>S. The HS<sup>-</sup> ion is therefore the dominant species in hydrogen sulfide solution for pH > 7 [Carroll et al., 1989; 1998]. It is noted that at 25 °C and 1 atm (101.325 kPa), H<sub>2</sub>S solution has a pH of about 4 [Carroll et al., 1989; 1998]. It is noted that in constructing Figure 1.1, H<sub>2</sub>S was measured by GC [Carroll et al., 1989b], while the amount of water was obtained by measuring the total mass of the sample further subtracted by the amount of H<sub>2</sub>S. The pH of H<sub>2</sub>S solution can be found based on the following Equations from 1.4 to 1.8 [Nebergall et al., 1968]:

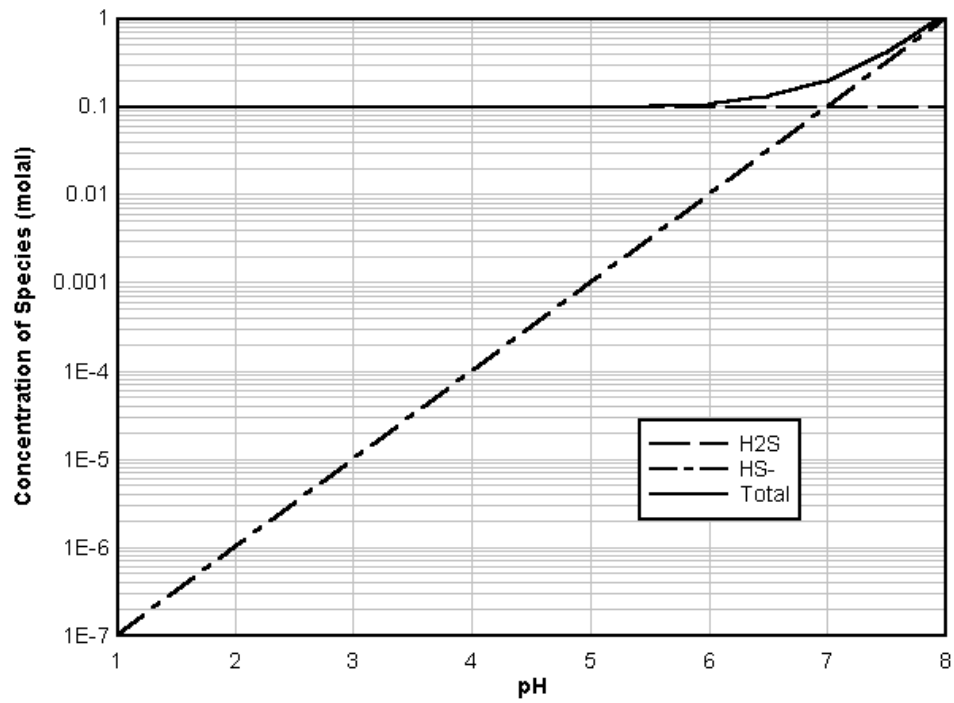


Figure 1.1: The approximate solubility of hydrogen sulfide as a function of the pH [Carroll, 1998].

$$\frac{[HS^-][H^+]}{H_2S} = K_1 \quad (1.4)$$

$$\frac{[S^{2-}][H^+]}{[HS^-]} = K_2 \quad (1.5)$$

$$\frac{[OH^-][H^+]}{[H_2O]} = K_3 \quad (1.6)$$

where  $K_1$  to  $K_3$  are the equilibrium constants which can be found from Roberts et al. [1985], and  $[X]$  is the concentration of ions or molecules in the unit of mole per liter.

Since the solution should have no charge (i.e., neither negative nor positive), therefore we have the following equilibrium equation:

$$[\text{H}^+] = [\text{HS}^-] + [\text{S}^{2-}] + [\text{OH}^-] \quad (1.7)$$

From Equation (1.7), we can obtain the concentration of  $[\text{H}^+]$ , and therefore the pH can be determined with the following equation:

$$\text{pH} = -\log [\text{H}^+] \quad (1.8)$$

The primary industrial uses of hydrogen sulfide include the production of elemental sulfur and sulfuric acid, the manufacture of heavy water and other chemicals, and as an analytical reagent. An  $\text{H}_2\text{S}$  molecule that freely diffuses across membranes [Pearson et. al 1978; Bagarinao, 1992] exerts its toxicity by forming sulfides with the active groups of different metalloenzymes and blood pigments (e.g., the Fe component of cytochrome oxidase can be tied up as a sulfide, thereby interrupting cellular respiration) [Miron et al., 1993]. Some researchers believed that hydrogen sulfide is absorbed rapidly through the lungs [Milby et al., 1999a; Guidotti, 1996; Glass 1990; Mehlman, 1994]. Exposure to  $\text{H}_2\text{S}$  has been recognized as a partial cause in the increase in cardiovascular-related deaths [Kosmider et al., 1967].

The toxicity of hydrogen sulfide is related to its concentration. The inhalation of high concentrations of  $\text{H}_2\text{S}$  (greater than 2000 ppm or 2780  $\text{mg}/\text{m}^3$ ) has profound effects



on the respiratory system, leading to unconsciousness with attendant neurological sequelae [Oseid et al., 1974a, b; Knezovich et al., 1994], and can even be fatal within seconds or minutes in both humans and animals [Lorans, 1996]. Even a low concentration of H<sub>2</sub>S may change a material from material A to material B when H<sub>2</sub>S interacts with A, for example Ag could become AgS when Ag interacts with H<sub>2</sub>S – a kind of “S-pollution” [Canela et al., 1998; Wieckowska, 1995].

### **1.1.2 Endogenously Generated Hydrogen Sulfide and Metabolism**

H<sub>2</sub>S is also a biological gas endogenously generated from *L-cysteine* in a reaction catalyzed by *cystathionine beta-synthase* (CBS) and/or *cystathionine gamma-lyase* (CSE) [Wang, 2002]. Various mammalian cells and tissues can produce and utilize H<sub>2</sub>S [Pace, 1997]. For instance, the physiological concentration of H<sub>2</sub>S in mammalian brain has been reported to be 50–160 μM [Abe et al., 1996]. Recent studies also showed that vascular tissues can generate measurable amounts of H<sub>2</sub>S [Zhao et al., 2001; Hosoki et al., 1997]. For example, the H<sub>2</sub>S concentration of the rat serum is about 46 μM [Zhao et al., 2001].

In some tissues both CBS and CSE are needed for generation of H<sub>2</sub>S, whereas in others one enzyme suffices [Wang, 2002]. For example, Chen et al. [1999] determined the activity and protein levels of CBS in a number of cardiovascular cells and tissues by direct enzyme assay and Western blot analysis, as well as in various human atrium and ventricle tissues [Chen et al., 1999; Bao et al., 1998]. They found that CBS was lacking

in these parts. Therefore, CBS does not play an important role in generating H<sub>2</sub>S in cardiovascular tissues. On the other hand CSE and endogenous production of H<sub>2</sub>S were both found in some parts of rat cardiovascular tissues [Hosoki et al., 1997, Zhao et al., 2001]. Thus, CSE is the enzyme for H<sub>2</sub>S in the cardiovascular system.

The expression of CBS [Meier et al., 2001] and CSE [Wang, 2002; Zhao et al., 2001; 2003; Levonen et al., 2000; Lu et al., 1992; Yap et al., 2000; Van der Molen et al., 1997] has been identified in many human and other mammalian cells, including those from liver, kidney, brain, skin fibroblasts, and blood lymphocytes. Table 1.2 gives the reported mammalian tissues where H<sub>2</sub>S was endogenously generated [Ubuka, 2002]. Table 1.3 presents some reported data for rats' tissue H<sub>2</sub>S concentrations [Hannestad et al., 1989]. From Table 1.2 we can see H<sub>2</sub>S occurs in nerve and cardiovascular systems. Active studies have been reported on the role of H<sub>2</sub>S in these two systems.

Table 1.2: Source Tissues for H<sub>2</sub>S Production in Mammals\* .

Species	Tissues
Rat	Brain, brainstem, cerebellum, hippocampus, striatum, cortex, hindbrain, lung, liver, serum, kidney, heart, spleen, blood, plasma, red blood cell, skeletal muscle, vascular smooth muscle
Man (Male, Female)	Brainstem, red blood cell, serum
Mouse	Brain, liver, kidney, serum
Bovine	Brain (gray matter), serum
Guinea pig	Serum
Rabbit	Serum

\*: [Ubuka, 2002]

Table 1.3: The H<sub>2</sub>S Content in Rats' Tissues\* .

Tissue	Concentration (n)
	nmol/g
Plasma	0.4 (3)
Red blood bell	0.2 (3)
Liver	10.2 (3)
Kidney	26.8 (3)
Brain	36.7 (3)
Heart	35.6 (3)
Skeletal muscle	6.2 (3)
Spleen	4.2 (3)

\*: [Hannestad et al. 1989]

n: number of animals

Another less important endogenous source of H<sub>2</sub>S is the nonenzymatic reduction of elemental sulfur to H<sub>2</sub>S, a process with the incremental reduction of equivalents obtained from the oxidation of glucose [Searcy et al., 1998]. All essential components of this non-enzymatic pathway are present *in-vivo*, including the supply of reducible sulfur. Blood circulation of humans [Westely et al., 1991] or mice [Buzaleh et al., 1990] can provide millimolar concentration of sulfur.

A summary of the endogenous H<sub>2</sub>S formation can be seen in the following two figures [Wang, 2002]. Figure 1.2 indicates that H<sub>2</sub>S *in-vivo* is metabolized by oxidation in mitochondria or by methylation in cytosol. Figure 1.3 shows the nonenzymatic reduction of elemental sulfur to H<sub>2</sub>S using reducing equivalents obtained from the oxidation of glucose:

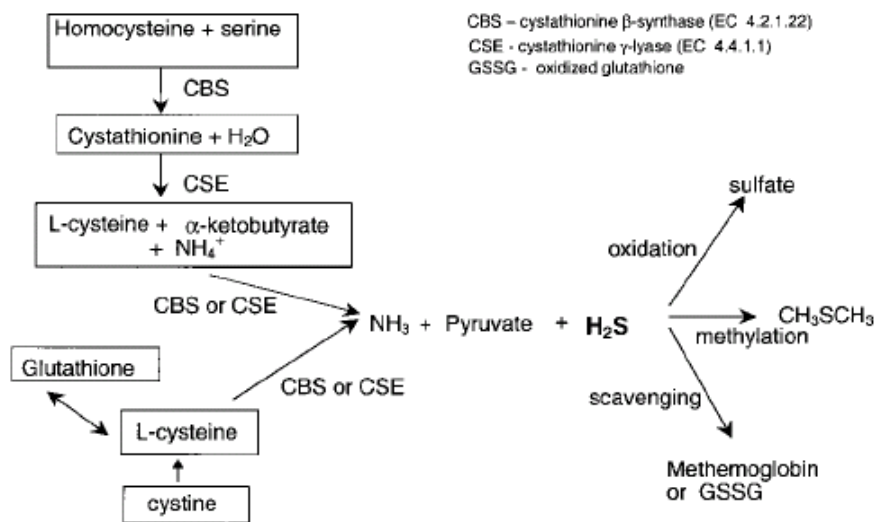


Figure 1.2: Endogenous enzymatic production and metabolism of H<sub>2</sub>S [Wang, 2002].

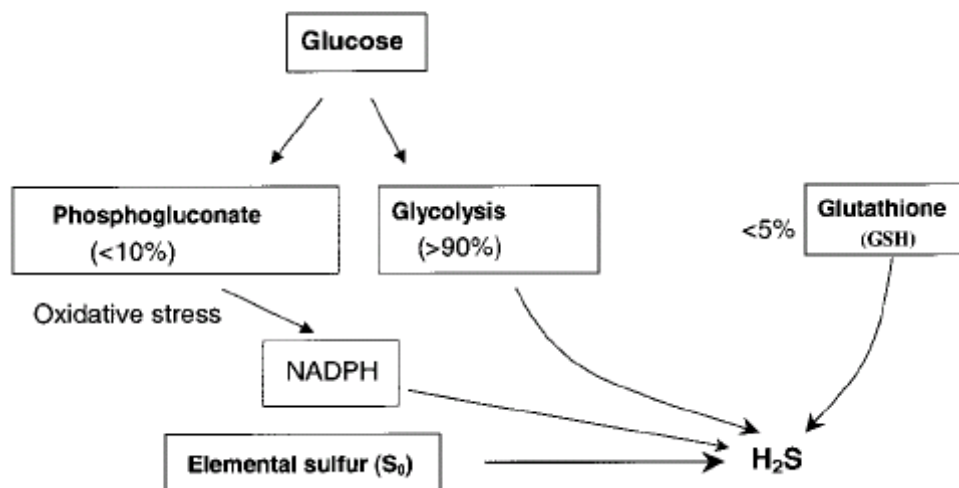


Figure 1.3: Endogenous nonenzymatic production of H<sub>2</sub>S [Wang, 2002].

In animals and humans, H<sub>2</sub>S distributes to the blood, brain, lung, heart, liver, spleen, and kidney [Imamura et al., 1996]. Although hydrogen sulfide is metabolized by three pathways, namely oxidation, methylation, and reactions with metalloproteins, oxidation is the primary metabolic pathway for H<sub>2</sub>S, with thiosulfate and sulfate as metabolites [Beauchamp et al., 1984; Kage et al., 1992]. Metabolism in laboratory animals and in humans appears to be similar. The major oxidation product of H<sub>2</sub>S metabolism is sulfate [Beauchamp et al., 1984], although thiosulfate may also be isolated from tissues exposed to hydrogen sulfide [Kage et al., 1992].

*In-vivo* H<sub>2</sub>S can be removed by methemoglobin [Beauchamp et al., 1984] or by metallo- or disulfide-containing molecules such as oxidized glutathione [Smith et al.,

1966] during metabolizing by oxidation in mitochondria or by methylation in cytosol. Recently, scientists noticed that hemoglobin may be the common “sink” for CO in forming scarlet carboxyhemoglobin [Wang, 1998], for NO in forming nitrosyl hemoglobin, and for H<sub>2</sub>S in forming green sulfhemoglobin [Arp et al., 1983].

H<sub>2</sub>S is excreted mainly by the kidney as free or conjugated sulfate [Beauchamp et al., 1984]. Urine is the primary route of elimination following H<sub>2</sub>S exposure. Gunina [1959] reported that the majority of the hydrogen sulfide (70 – 99%) in dogs and rats was eliminated in the urine 24 hours after exposure to H<sub>2</sub>S by inhalation routes. Kage et al. [1992] detected thiosulfate but not sulfide in the urine of rabbits exposed to 100 – 200 ppm (139 – 278 mg/m<sup>3</sup>) H<sub>2</sub>S by inhalation up to 24 hours after exposure, with the highest levels detected 2 hours after exposure. Thiosulfate was also found in the urine of humans exposed to 8, 18, or 30 ppm (11, 25, or 42 mg/m<sup>3</sup>) H<sub>2</sub>S for 30 – 45 minutes [Kangas et al., 1987].

### **1.1.3 Physiological Effects of Hydrogen Sulfide**

The toxicity of H<sub>2</sub>S has been known for about 300 years. A complete toxicological profile of H<sub>2</sub>S can be found in Beauchamp et al. [1984] and Reiffenstein et al. [1992]. By analogy to other endogenous gaseous molecules such as nitric oxide (NO) and carbon monoxide (CO) [Wang et al., 1997], H<sub>2</sub>S was hypothesized to fulfill a physiological role in regulating cardiovascular functions that is distinctive from its

toxicological effect. Hydrogen sulfide gas naturally produced by the body is not simply a toxic gas, but a vascular dilator.

The H<sub>2</sub>S concentrations in different brain regions were measured by Warenycia et al. [1989]. The presence of detectable sulfide in all untreated animals indicates that there is an endogenous level of sulfide in the brain. Further research found that in the human, the level of H<sub>2</sub>S was decreased by ~55% in the brains of Alzheimer's disease patients but no change in the *L-cysteine* level or CBS activity in brain [Eto et al., 2002]. The chronic exposure to H<sub>2</sub>S impaired foetal neuronal development and monoamine neurochemistry in rats [Roth et al., 1995]. Thus, H<sub>2</sub>S may have functional involvement in neurodegenerative diseases [Moore et al., 2003].

In the cardiovascular system, H<sub>2</sub>S appears to be synthesised mainly by a different enzyme, namely *cystathionine-γ-lyase*, and in rodents, plasma concentrations of up to 80 μM have been recorded. The addition of H<sub>2</sub>S to aortic rings or smooth muscle causes vasorelaxation by a mechanism that may involve the opening of K<sub>ATP</sub> channels, suggesting a physiological role for H<sub>2</sub>S in the vasculature [Zhao et al., 2001].

Zhao et al. [2001] detected the transcriptional expression of the H<sub>2</sub>S generating enzyme CSE in all rat arteries tested, but not in brain and lungs [Smith et al., 1979; Abe et al., 1996]. They found that CSE has the capability to cleave *L-cysteine* to produce H<sub>2</sub>S, ammonium, and *pyruvate*. They also found that NO significantly increases CSE activity in vascular tissues. NO appears to be a physiological modulator of the

endogenous production of H<sub>2</sub>S by indirectly stimulating CSE, as well as by directly increasing the CSE expression. The interaction between two gases, NO and H<sub>2</sub>S, may function as a molecular switch for regulating vascular tone to relax contracted blood vessels and to reduce blood pressure. The vasorelaxation induced by H<sub>2</sub>S has a major direct effect on smooth muscles. Wang [2002] summarized the relationship between NO and H<sub>2</sub>S as indicated in Figure 1.4.

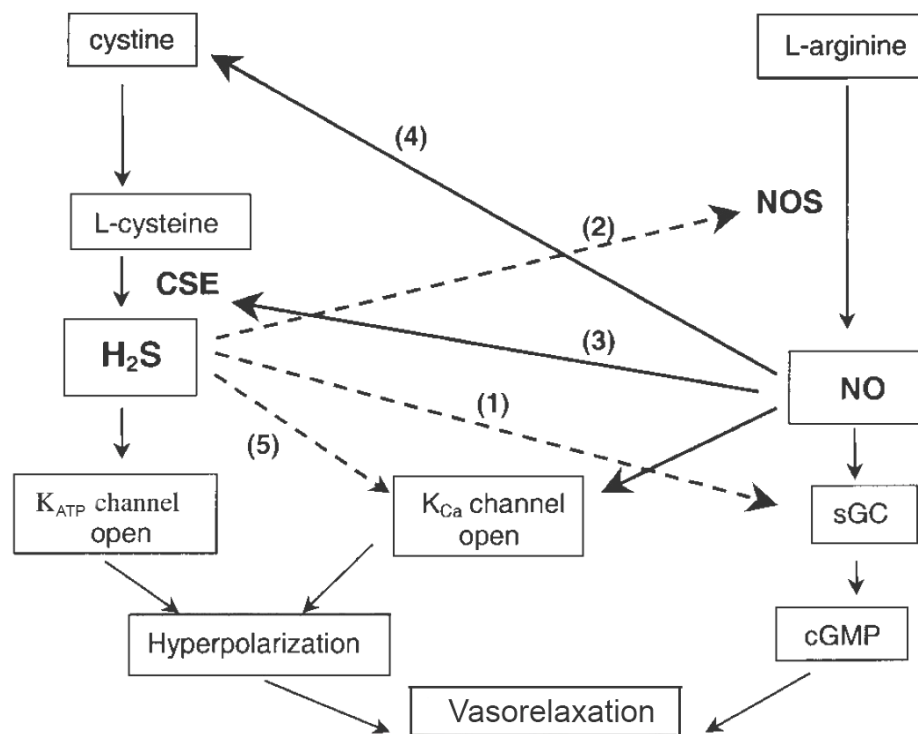


Figure 1.4: Hypothesized scheme of the interactions of H<sub>2</sub>S and NO in vascular tissues. The solid lines indicate the stimulatory inputs and the dashed lines, inhibitory inputs. (1) H<sub>2</sub>S may decrease the sensitivity of the cGMP pathway to NO. (2) H<sub>2</sub>S may reduce the expression level of NO synthase (NOS). (3) NO may increase the expression of CSE. (4) NO may increase the cellular uptake of cystine. (5) H<sub>2</sub>S may modify K<sub>Ca</sub> channels to decrease their sensitivity to NO [Wang, 2002].



In 2005, Patacchini et al. [2005] found that in the detrusor muscle of the rat urinary bladder, H<sub>2</sub>S produced contractile responses. These results provide evidence that in the detrusor muscle, the dominant effect of physiologically relevant concentrations of H<sub>2</sub>S involves stimulation of capsaicin-sensitive primary afferent neurons with consequent release of *tachykinins*, which in turn produces contractile responses of the detrusor muscle. This indicates that H<sub>2</sub>S predominantly activates the primary afferent nerve terminals directly rather than indirectly via axonal conduction, which involves fast tetrodotoxin-sensitive sodium channels.

#### **1.1.4 Significance of Measurement of Low Concentration Hydrogen Sulfide**

Endogenous levels of H<sub>2</sub>S are 50~160 μM in rat brain [Abe et al., 1996], ~46 μM in Sprague-Dawley rat plasma [Zhao et al., 2001], and 10~100 μM in human blood [Richardson et al., 2000]. Whether H<sub>2</sub>S plays a physiological, pathophysiological, or even a toxicological role depends on its *in-vivo* level. However, the concentration difference between toxicological and physiological effects of H<sub>2</sub>S is very small. The toxic level of H<sub>2</sub>S reported by Warencya et al. [1989] is less than twofold greater than its endogenous level in rat brain tissues. Mitchell et al. [1993] found that at the time of death of mice exposed to 60 micrograms g<sup>-1</sup> sodium hydrosulfide, the sulfide concentration only elevated from the endogenous level by 57%, 18%, and 64% in brain, liver, and kidney, respectively. Chen et al. [2005] studied the sera of humans from ages 50 to 80 years. They found that there is no significant H<sub>2</sub>S concentration difference among the age groups (35.7 ± 1.2 μM for age 50-60, 34.0 ± 0.9 μM for age 60-70, and

36.4 ± 1.1 μM for age 70-80, respectively). However, serum levels of H<sub>2</sub>S were 49.4% higher in patients with stable COPD (Chronic Obstructive Pulmonary Disease) than those in age-matched healthy control subjects. They suggested that endogenous H<sub>2</sub>S is involved in the pathogenesis of airway obstruction in COPD, and its alteration in level may be connected with disease activity and severity. From their research, the H<sub>2</sub>S concentration difference between health and COPD is less than 20 μM. It is thus reasoned that the dose-response relationship of H<sub>2</sub>S at the physiological concentration range must be very steep before the physiological effect of H<sub>2</sub>S sharply transforms into a highly toxic effect [Zhao et al., 2001]. As such, the measurement of H<sub>2</sub>S in mammals with small-quantity resolution becomes an important subject.

## **1.2 Existing Hydrogen Sulfide Measurement Methods**

Unfortunately, only a limited number of analytical techniques have been used for measuring hydrogen sulfide in the breath (expired air), biological tissues, and fluids including blood and saliva. Current methods for measurement of hydrogen sulfide include chromatography, spectrophotometry, and sulfide ion-specific electrode.

### **1.2.1 Chromatography**

Chromatography (including gas chromatography, liquid chromatography, ion exchange chromatography, and affinity chromatography) is a measurement technique used for analyzing and/or separating mixtures of chemical substances. The basic

working principles of these chromatography methods are as follows [Wheeler, 1998]: A sample of the mixture to be analyzed (the analyte) is applied to a stationary fixed material (the adsorbent), and then a second material (the eluent) is passed through or over the stationary phase. The compounds contained in the analyte are then partitioned between the stationary adsorbent and the moving eluent. As different materials adhere to the adsorbent with different forces, some adhere to the adsorbent more strongly and therefore move through the adsorbent more slowly when the eluent flows over them, while other components of the analyte are less strongly adsorbed on the stationary phase and move along more quickly with the moving eluent. Therefore, as the eluent flows through the column, the components of the analyte will move down the column at different speeds and therefore separate from one another.

The resolution of chromatography is defined as [Miller et al., 2005]:

$$R = \frac{1}{4} N^{1/2} \left( \frac{\alpha - 1}{\alpha} \right) \left( \frac{1 + k}{k} \right) \quad (1.9)$$

where  $N = 5.55 t_R^2 / w^2$ ;  $t_R$  is the retention time, which is the time between the samples being injected and the time the analyte peak reaches a detector at the end of the column. Each analyte in a sample will have a different retention time;  $w$  is the half width of the peak (Figure 1.5).

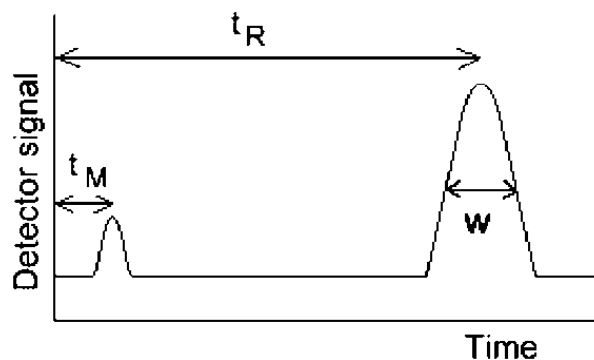


Figure 1.5: Distribution of analytes between phases.

Retention factor  $k = (t_R - t_M) / t_M$  and  $t_M$  (Figure 1.5) is the time required for the mobile phase to pass through the column of the chromatography. Further, selectivity factor,  $\alpha = k_B/k_A$  describes the separation of two species (A and B) on the column. Note that here species A elutes faster than species B. The selectivity factor is always greater than 1.

The concentration difference that can be detected is defined as the interval between two adjacent peaks when the amplifier attenuation is set such that the smaller peak is at least 50% of full scale. The limit is achieved when  $R = 1.5$ . For example, the measurement of  $H_2S$  in air by ion chromatography has the working range of 20 – 500  $\mu M$  for a 20 L air sample [Cassinelli, 1994].

### 1.2.2 Spectrophotometry

Spectrophotometry is widely used to measure trace amounts of  $H_2S$ . It is also known as the methylene-blue method in analytical chemistry, since the dye methylene

blue will be formed when the H<sub>2</sub>S solution reacts with ferric chloride (FeCl<sub>3</sub>) and *N,N*-dimethyl-*p*-phenylenediamine. Absorbance of the dye in solution is then measured by the spectrophotometer. When monochromatic light (light of a specific wavelength) passes through a solution there is usually a quantitative relationship (Beer's law) between the solute concentration and the intensity of the transmitted light, that is:

$$I = I_0 \times 10^{-kcl} \quad (1.10)$$

where  $I_0$  is the intensity of transmitted light using the pure solvent,  $I$  is the intensity of the transmitted light when the coloured compound is added,  $c$  is the concentration of the coloured compound,  $l$  is the distance that the light passes through the solution and  $k$  is a constant.

If  $l$  is a constant, as is the case with a spectrophotometer measurement, Beer's law can be written as:

$$I / I_0 = 10^{-hc} = T \quad (1.11)$$

where  $T$  is the transmittance of the solution and  $h$  is a constant.

We can also write this equation as:

$$-\log T = hc = K = \text{optical density} \quad (1.12)$$

$$\Delta c = \Delta K / h. \quad (1.13)$$

The minimum concentration of H<sub>2</sub>S that can be measured is related to the optical density changes that can be detected by the instrument. Photoacoustic spectroscopy of H<sub>2</sub>S converted to methylene blue has greater sensitivity than standard spectrophotometric methods (NIOSH, 1979). By maximizing the instrument response to the 750 nm peak, it is possible to achieve a detection limit of  $3 \times 10^{-4}$  μM when samples are collected at 2.0 L min<sup>-1</sup> for a 1 h period.

### 1.2.3 Sulfide Ion-Specific Electrode

First, a typical sulfide calibration curve is obtained. This means that electrode potentials of standard solutions (the concentrations of the standard solutions were known before the measurement) are measured and plotted on the linear axis against their concentrations on the log axis. The linear axis (y-axis) denotes the milli-volt values and the log axis (x-axis) represents the concentration values of the solutions. Then, the electrode potential of the sample solution is recorded. From this linear calibration curve, an unknown sample concentration with its milli-volt values can be obtained. The calibration procedure for H<sub>2</sub>S is very complicated because sulfide ion-specific electrodes are sensitive only for the fully dissociated form of sulfide. However, the equilibrium between H<sub>2</sub>S, HS<sup>-</sup> and S<sup>2-</sup> is pH dependent such that the calibration needs to be carried out in a well-buffered system of known pH, and with a complete lack of oxygen

[Gemerden et al., 1989]. The accuracy of standard solutions, usually measured by the methylene-blue method [Trupper et al., 1964], depends on the measurement method. Typically, the ion-specific electrode has a linear response range of between  $10^{-1}$  M and  $10^{-5}$  M and a detection limit on the order of  $10^{-5} - 10^{-6}$  M. However, the observed detection limit is often affected by the presence of other interfering ions or impurities [Brzozka, 2006]. Recently, Dennis et al., reported measurement of very low sulfide concentration ( $0.5 \mu\text{M}$ ); however, their method requires steady state concentrations with a modified sulfide ion-specific electrode [Dennis et al., 2004].

The advantages and disadvantages of each method are summarized in Table 1.3. All these methods generally require bulky samples and are invasive and off-line, and thus they are not qualified for *in-vivo* and non-invasive measurement.

Table 1.4: Comparison of the Current Methods for H<sub>2</sub>S Measurement.

Measurement methods	Advantages	Disadvantages
Spectrophotometry	<ul style="list-style-type: none"> <li>Widely used</li> <li>Less expensive</li> </ul>	<ul style="list-style-type: none"> <li>Long experimental time (1.5 days)</li> <li>In vitro measurement</li> <li>Detect limit: <math>3 \times 10^{-4}</math> <math>\mu\text{M}</math> when sample are collected at <math>2.0 \text{ L min}^{-1}</math> for 1 hour</li> </ul>
Chromatography	<ul style="list-style-type: none"> <li>Accurate detection</li> <li>Separates H<sub>2</sub>S from mixtures of chemical substances</li> </ul>	<ul style="list-style-type: none"> <li>Expensive for the first setup</li> <li>In vitro measurement</li> <li>Detect limit: 20-500 <math>\mu\text{M}</math> for 20L air sample</li> </ul>
Sulfide ion-specific electrode	<ul style="list-style-type: none"> <li>Easy to operate</li> <li>Low cost for initial setup</li> </ul>	<ul style="list-style-type: none"> <li>Needs to be calibrated before every measurement</li> <li>Detect limit: 0.5 <math>\mu\text{M}</math> with steady state concentrations</li> </ul>

#### 1.2.4 A New Method for Hydrogen Sulfide Measurement

The existing methods for measurement of H<sub>2</sub>S in mammal tissues require a bulky amount of tissues and require a complex procedure for the sample preparation, and as well they are extremely invasive. Because these methods could not be updated to real-time measurement, they have limitations in clinical applications and in the study of H<sub>2</sub>S effect in the living cell.



In recent studies, micro-cantilevers with specific functional coatings have been used to determine concentrations of molecules in both gas and liquid phases, and exhibit the sensitivity to detect concentrations in the trace range [Hansen et al., 2001]. To use the cantilevers in concentration measurement, the cantilevers should either be made of adsorbent material or coated by a thin layer of adsorbent. When the cantilevers are in the solution, the adsorption occurs. This adsorption can cause bending of the cantilever due to the surface stress change. The bend is then transformed into a change of another form (such as electrical or optical) that can be easily monitored by simple instrumentation (Figure 1.6).

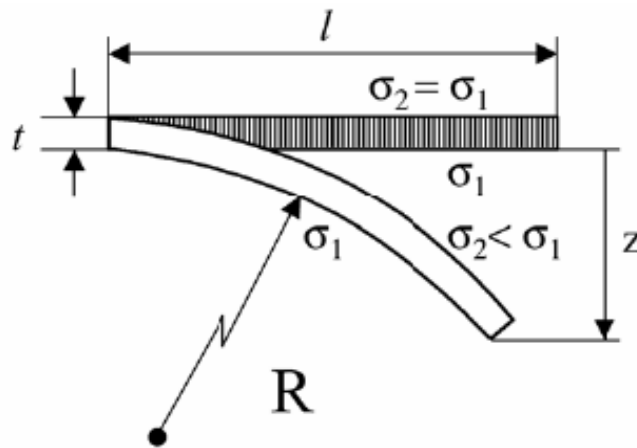


Figure 1.6: Circular bending of a cantilever induced by a differential stress due to unequal changes of interfacial energies on each of the cantilever sides [Lavrik et al., 2001].

In Figure 1.6, the equilibrium state of the cantilever is disturbed, causing bending when surface stresses  $\sigma_1$  and  $\sigma_2$  on each side of the cantilever change unequally. The bend can be characterized by the radius of cantilever curvature,  $R$ , or tip deflection  $z = l^2 / 2R$ . The effect of surface stress change on the cantilever bending is quantified by Stoney's equation [Stoney, 1909]:

$$R^{-1} = 6 (1-\nu) \Delta\sigma / Et^2 \quad (1.14)$$

and

$$z_{\max} = 3l^2(1-\nu) \Delta\sigma / Et^2 \quad (1.15)$$

where  $\nu$  and  $E$  are, respectively, the Poisson's ratio and Young's modulus for the cantilever,  $t$  is thickness of the micro-cantilever,  $l$  is cantilever effective length, and  $\Delta\sigma = \sigma_2 - \sigma_1$  is a differential surface stress. Although Stoney's Equations (1.14) and (1.15) do not account for a multi-layer structure of cantilevers that are typically used in sensor applications, they give a fair approximation as long as the over-layers are thin in comparison to the substrate material [Lavrik et al., 2001].

In practice, the bending of the cantilever can be detected by AFM which is a very high-resolution type of scanning probe microscope and is one of the foremost tools for imaging, measuring, and manipulating matter at the nanoscale.

Although the research of Lavrik et al [2001] opened a bright future for nano quantity, low concentration  $H_2S$  measurement, there remain many questions unsolved. For example, what kinds of coating materials can be used in the case of small quantity and low concentration  $H_2S$  measurement? In searching for the suitable materials, the factor of stability must be considered because the measurement may be used under different clinic conditions.

In this dissertation, we will present a new method in H<sub>2</sub>S measurement. This new method is based on carbon nanotube, inspired by (1) the existing knowledge that activated carbon can absorb H<sub>2</sub>S very well, (2) carbon nanotube can be comparable with activated carbon in terms of one important property – surface to weight ratio, and (3) carbon nanotube has excellent properties which are highly desirable for sensors.

We first studied the binding of carbon nanotube with H<sub>2</sub>S in distilled water. We then studied the binding of carbon nanotube with H<sub>2</sub>S in sera where there are some proteins present. The proteins may also bind with carbon nanotube, which may compromise selectivity of carbon nanotube with respect to H<sub>2</sub>S. We also studied a critical issue when the proposed method may be used for living cells – that is tracking of carbon nanotube in a fluid.

In particular, the remainder of the dissertation is organized in the following way. Chapter 2 presents related knowledge including activated carbon, carbon nanotube, confocal laser scanning and Raman microscopes which were primarily used to confirm the binding of carbon nanotube with H<sub>2</sub>S in context of this dissertation study, adhesion theory which is indeed a foundation to study the binding behaviour, and Brownian motion and the control system for developing a clinic oriented method. Chapter 3 discusses H<sub>2</sub>S measurement in water solutions by carbon nanotube. Chapter 4 discusses H<sub>2</sub>S measurement in sera. Chapter 5 discusses the control system that can track a single nano particle in Brownian motion. Chapter 6 is a conclusion of the work, along with a discussion of future work.

## **CHAPTER 2**

### **BACKGROUND KNOWLEDGE**

#### **2.1 Introduction**

One key reason for using carbon nanotube for the purposes of this study is that carbon nanotube is comparable with activated carbon in terms of surface to weight ratio which is in turn related to the adsorption of  $H_2S$ . In this chapter, this idea will be closely examined; specifically, Section 2.2 will discuss activated carbon and Section 2.3 will discuss carbon nanotube. Some background knowledge regarding blood and serum (Section 2.4), confocal laser scanning microscopy (Section 2.5), and Raman microscopy (Section 2.6) will also be presented in this chapter. Further, the mechanism underlying the adsorption of one element by another is always related to adhesion theory, so a discussion on adhesion will be given in Section 2.7. Section 2.8 will discuss the Brownian motion which is relevant to tracking of carbon nanotube by the laser beam of the confocal laser scanning microscopy when this method may be used for living cells. Finally in Section 2.9, the feedback control knowledge that is needed for a software system to control the laser beam to track carbon nanotube in a fluid will be discussed. The contents of Section 2.5 and 2.6 have been published [Wu et al., 2007].

## 2.2 Activated Carbon

An activated carbon is a solid, porous, black carbonaceous material. It is distinguished from an elemental carbon by the absence of both impurities and an oxidized surface [Mattson et al., 1971]. It can be prepared from a large number of sources such as coconut, wood, peat, coal, tar, sawdust, and cellulose residues [Lambiotte, 1942].

Any carbon source can be converted into an activated carbon via a number of methods. Usually, there are two general processes: carbonization and activation. During carbonization, most of the non-carbon elements are removed in a gaseous form by the pyrolytic decomposition of their source material. The porous structure is mainly developed during activation by means of an activation agent that reacts with the carbon. Such agents may include synthetic acids, bases, and other substances in a stream of gases such as steam ( $H_2O$ ), nitrogen ( $N_2$ ), or carbon dioxide ( $CO_2$ ) [Rodríguez-Reinoso et al., 2006].

The most important property of activated carbon, the property that determines its usage, is the pore structure (Figure 2.1). There are two types of pore structures: (1) slit pores, which have cracks around the surface of carbon, and (2) hole pores, which have small openings on the surface that extend, in cylinder form, toward the centre of the carbon. The total number of pores and their shapes and sizes determine not only the

adsorption capacity but also dynamic adsorption rate of activated carbon. Pores in activated carbon can be classified in term of their size as follows [Rodriguez-Reinoso et al., 1989]:

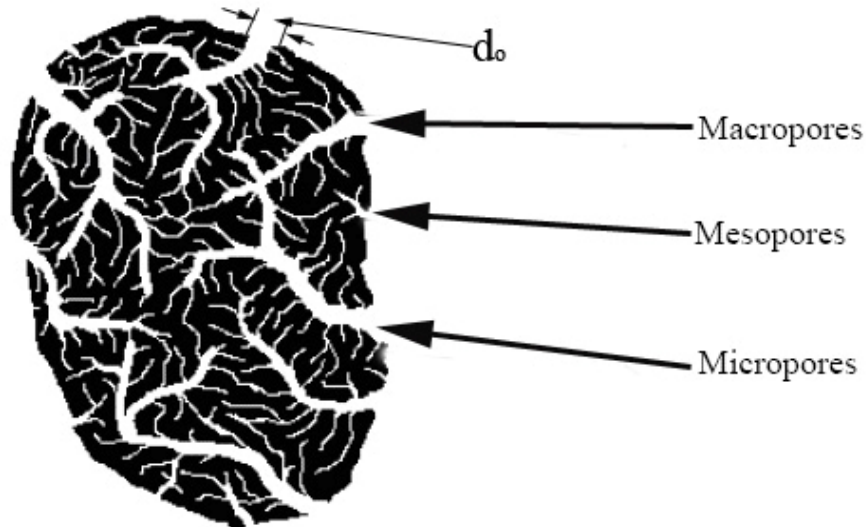


Figure 2.1: Schematic representation of the different types of pores in an activated carbon particle [Wu, 2004].

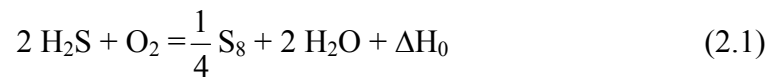
- macropores:  $d_0 > 50$  nm
- mesopores:  $2 \leq d_0 \leq 50$  nm
- micropores:  $d_0 < 2$  nm
- ultramicropores:  $d_0 < 0.7$  nm
- supermicropores:  $0.7 < d_0 < 2$  nm

where  $d_0$  is the pore width for the slit type pore, or the pore diameter for the hole type pore.

Because of its pore structure, activated carbon has an extraordinarily large ratio of surface area over weight, which makes it suitable for a wide range of applications. Activated carbon can be used as a decolourizing agent, a taste and odour removing agent, and as a purification agent in food processing. A major use of activated carbon is in water purification, including removal of  $H_2S$  in water. Water treatment accounts for approximately half of the total use of activated carbon in the United States [Baker et al., 1992]. There are also a number of applications related to purification processes in the clothing, textile, automobile, cosmetics, and pharmaceutical industries. The hundreds of other uses include its utilization as an adsorbent in gas mask filters and as a pollution control material in a range of filters [Ashford, 1994].

Activated carbon impregnated by NaOH or KOH becomes a carbonaceous adsorbent that has chemicals finely distributed on its internal surface. The impregnation optimizes some existing properties of activated carbon by giving a synergism between the chemicals and the carbon [Tsai et al., 2001]. This facilitates the otherwise impossible cost-effective removal of certain impurities from gas streams. Impregnated activated carbons are available and have been used for many years in the fields of gas purification, civil and military gas protection and catalysis. The removal of  $H_2S$  by activated carbon generally involves some catalytic activity as well as adsorption [Masuda et al., 1999]. The role of carbon was found to be more than merely the provision of a porous medium [Kato et al., 1995; Primavera et al., 1998].

A dry blend of H<sub>2</sub>S and oxygen do not react with each other at ambient temperatures, but only at temperatures above 200°C. However, Primavera et al. [1998] have shown that H<sub>2</sub>S can be either transformed into sulfur dioxide or oxidized to elemental sulfur, depending on reaction conditions. Generally, in the presence of activated carbon, at ambient temperatures, the oxidation of H<sub>2</sub>S to S is promoted. The activated carbon with this property can be used as catalyst for H<sub>2</sub>S removal [Furimsky, 1997; Primavera et al., 1998]:



$$(\Delta\text{H}_0 = - 444 \text{ kJ})$$

The sulfur produced is on the internal surface of activated carbon, while the water is desorbed from the catalyst surface.

Activated carbon can be regenerated. This can be done by transporting the activated carbon to a thermal regeneration facility, where the carbon is heated up to 800 – 1000 °C in a hydrogen atmosphere to boil off the adsorbed load together with about 10% carbon matrix. The disadvantage of this method is its relatively high cost; however, regeneration of activated carbon allows it to be re-used a number of times.




### 2.3 Carbon Nanotube

The ground state electron configuration of the carbon atom is  $2s^2 2p^2$ . Carbon can form four covalent bonds. In the  $sp^3$  hybrid model, all of the bonds are equivalent and have a tetrahedral arrangement of sigma bonds around the carbon; this is the bonding arrangement of diamond or methane. In the  $sp^2$  bonding arrangement, there are three sigma bonds and one pi bond. The bonding in graphite is described by  $sp^2$  hybrid bonding which explains the sheet structure of graphite. In addition, the pi bonding in the sheets provide sufficient electron density for weak interaction between the sheets.

Basically, a single-wall carbon nanotube is analogous to a sheet of graphite rolled into a cylinder and closed at either end with caps containing pentagonal rings, and a multi-wall carbon nanotube is one comprising several sheets of graphite. This growth pattern makes the carbon nanotubes very stable and it is difficult to separate a single carbon nanotube from their bundle. Due to this special structure, if a perfect nanotube is obtained it would be light, flexible, thermally stable, and chemically inert. Depending on the twist direction of the graphite sheet, nanotubes can be metallic or semi-conduct. Table 2.1 lists some properties of carbon nanotubes.

Table 2.1: Properties of Carbon Nanotube.

<b>Equilibrium Structure</b>	Average Diameter of SWNT's		1.2 -1.4 nm	Spires et al., 1996
	Distance from opposite Carbon Atoms (Line 1)		2.83 Å	Spires et al., 1996
	Analogous Carbon Atom Separation (Line 2)		2.456 Å	Spires et al., 1996
	Parallel Carbon Bond Separation (Line 3)		2.45 Å	Spires et al., 1996
	Carbon Bond Length (Line 4)		1.42 Å	Spires et al., 1996; Wildoer et al., 1998
	C - C Tight Bonding Overlap Energy		~ 2.5 eV	Wildoer et al., 1998; Odom et al., 1998
<b>Optical Properties</b>	Metallic		0 eV	Dekker et al., 1999
	Semi-conducting		~ 0.5 eV	Wildoer et al., 1998; Dekker et al., 1999
<b>Electrical Transport</b>	Conductance Quantization		$(12.9 \text{ k}\Omega)^{-1}$	Dekker et al., 1999; Frank et al., 1998
	Resistivity		$10^{-4} \Omega/\text{cm}$	Thess et al., 1996
	Maximum current density		$10^{13} \text{ A/m}^2$	Frank et al., 1998
<b>Thermal Transport</b>	Thermal conductivity		~ 2000 W/m/K	Hone et al., 1999; Berber et al., 2000

	Phonon mean free path		~ 100 nm	Hone et al., 1999
	Relaxation time		~ 10 <sup>-11</sup> s	Hone et al., 1999
<b>Elastic Behavior</b>	Young's modulus (SWNT)		~ 1 TPa	Dujardin et al., 1998; Schewe et al., 1996
	Maximum tensile strength		~ 100 GPa	Yu et al., 2000

It was reported that several types of defects such as vacancies, dislocations, and declinations could be generated during the growth of carbon nanotube [Persson, 1992]. These defects are known to be caused by unbound sites in carbon nanotubes and play an important role in controlling the mechanical and electronic properties of the surface. For example, the electronic density around defects is different from those in other parts, which can lead to different adsorptions at defects in comparison with the rest of the surface lattice. Furthermore, the defects usually lead to the restoration of broken bonds by means of adsorption, so the energy at the defect sites is much higher than that at the regular sites.

Their uniform pore size distribution, large ratio of surface area over weight, and excellent electronic properties make carbon nanotubes promising materials for H<sub>2</sub>S adsorption. At the sites of defects in carbon nanotubes, modification of the electronic density occurs around the defects so increased energy is needed to restore the broken bonds. This can lead to an increase in adsorption capacity of the carbon nanotubes.

In summary, activated carbon has a large ratio of surface area over weight because of its pore structure. The large ratio of surface area over weight of activated carbon increases the adsorption of H<sub>2</sub>S. Carbon nanotube has a large ratio of surface area over weight as well, and therefore carbon nanotube should be a promising material for H<sub>2</sub>S adsorption by the straightforward reasoning that activated carbon is an excellent absorbent of H<sub>2</sub>S. Carbon nanotube has additional properties, in addition to the property of absorption of H<sub>2</sub>S, which render it to be an excellent sensor for measurement of low concentration and nano quantity of H<sub>2</sub>S in fluids (water, serum, and others).

#### **2.4 Blood and Serum**

Blood consists of cellular materials (99% red blood cells, and 1% white blood cells and platelets), water, amino acids, proteins, carbohydrates, lipids, hormones, vitamins, electrolytes, dissolved gases, and cellular wastes [Shier et al., 2002]. In the red cells, hemoglobin (or haemoglobin) occupies 1/3 by volume.

Blood cells suspend in a liquid. As with any other suspension materials, the components of blood can be separated by centrifuging (spinning). Three layers are visible in centrifuged blood. The straw-colour liquid portion, called plasma, forms the top layer (~55%). Further, plasma comprises about 92% water, with plasma proteins being the most abundant solutes. The plasma protein groups are albumins, globulins, and fibrinogens. A thin cream-colored layer, called the Buffy coat, stays below the plasma.

The Buffy coat consists of white blood cells and platelets. Finally, red blood cells form the heavy bottom portion of the mixture (~45%) [Shier et al., 2002].

Serum or blood serum is a clear yellowish fluid obtained from whole blood by removing blood cells, platelets, and fibrogen; it is the blood plasma without the fibrogen [Levinson et al., 1942]. The components of serum are shown in Table 2.2.

Table 2.2: Serum Constituents\* .

Category	Constituents	Concentration
Proteins / Enzymes	Albumin, Dye binding	38– 50 g/L
	Bilirubin, total	0.1– 1.2 mg/dL
	ALT (ALanine Aminotransferase) at 37 °C	4– 36 U/Lb
	AST (Aspartate aminotransferase) at 37 °C	8– 33 U/L
	Amylase	30– 220 U/L
	CK ( <i>Creatine Kinase</i> ) at 37 °C	55– 170 U/L (Male)
		30– 135 U/L (Female)
	LD (Lactate Dehydrogenase) at 30 °C ( <i>Pyruvate</i> -> Lactate)	90– 310 U/L
	ALP (Alkaline Phosphatase) at 37 °C	20– 130 U/L
ACP (Acid Phosphatase) at 37 °C	2.2– 10.5 U/L	

Electrolytes	Calcium (Ca)	9.2– 11.0 mg/dL
	Sodium (Na), Plasma	3.1– 3.3 mg/mL
	Potassium (K), Plasma	148–195 ug/mL
	Chloride (Cl)	3.4– 3.7 mg/mL
	Magnesium (Mg)	1.6– 2.6 mg/dL
	Iron (Fe)	60– 150 ug/dL
	Phosphorus, Inorganic	2.3– 4.7 mg/dL
Lipids	Cholesterol	150– 250 mg/dL
	Triglyceride	10– 190 mg/dL
Hormones	<i>Prolactin</i>	1– 20 ug/L (Male)
		1– 25 ug/L (Female)
	Insulin (C256H381N65O76S6), <i>Radioimmunoassay</i> , Plasma	0.17– 1.0 ng/mL
	ACTH (AdrenoCorticoTropic Hormone), 0800h: unrestricted activity	<120 pg/mL
	Catecholamine, <i>Norepinephrine</i> , Radom	<1700 pg/mL
	<i>Cortisol</i> , 8– 10am, Plasma	5– 23 ug/dL
	<i>Gastrin</i>	25– 90 ng/L

	GH (Growth Hormone)	< 10 ug/L
	PTH (ParaThyroid Hormone), Intact molecule	10– 65 ng/L
	Renin, Normal sodium diet standing, 4h	0.7– 3.3 ug/L/h
	<i>Aldosterone</i> , upright	7– 30 ng/dL
	Glucagon	20– 100 ng/L
	TSH (Thyroid Stimulating Hormone)	0.32– 5.0 mU/L
Gases	Oxygen (O <sub>2</sub> ), Arterial, Whole blood	12.7– 13.3 kPa
	Carbon Dioxide (CO <sub>2</sub> ), Arterial, Whole blood	4.7– 5.3 kPa
	Hydrogen Sulfide (H <sub>2</sub> S)	1.6 ug/mL
	Nitrogen (N <sub>2</sub> )	<2 g/(5 Ld)
Others	Glucose, Fasting	70– 110 mg/dL

\*: Michael, 2000; Burtis, 1999; Henry, 1996].

## 2.5 Confocal Laser Scanning Microscopy

Unlike most other microscopes, a pinhole is used in a confocal laser scanning microscopy (Figure 2.2) such that a laser beam is focused by an objective into a small focal volume within a specimen. A mixture of emitted fluorescent light and reflected laser light from the illuminated volume is then collected by the objective. A beam

splitter separates the light mixture by allowing only the fluorescent light to pass through and reflecting the laser light. After passing a pinhole, the fluorescent light is detected by a photomultiplier (PMT) which transforms the light signal into the electrical signal which is then recorded.

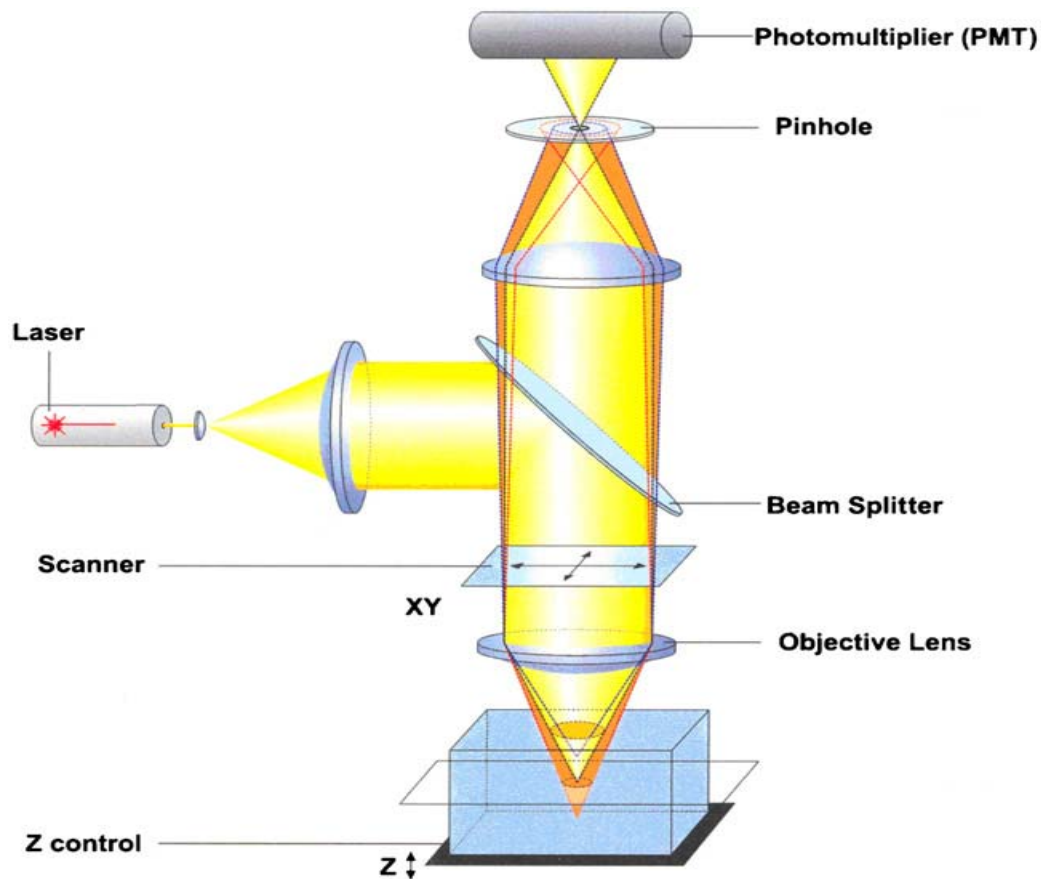


Figure 2.2: Working principle of confocal laser scanning microscopy (Zeiss LSM 510 Meta Manual).

In laser scanning microscopy, a specimen is illuminated by a point laser source. The scanning laser point source is a three-dimensional diffraction pattern determined by the optical system, including the numerical aperture of the system's objective and the wavelength of the laser light. With confocal laser scanning microscopy, the resolution



can be improved greatly, since only a small volume at a time of the element can be detected. The resolution limit in confocal laser scanning microscopy depends not only on the illumination but also on the generation of enough detectable photons from the sample. In addition, using a more advanced photo-detector, the noise caused by the detector can be further reduced; thereby the signal-to-noise ratio can be increased. Increasing excitation intensity can possibly enhance the signal-to-noise ratio, but high intensity of the laser beam in the visible region may bleach the sample [Wu et al., 2007].

## **2.6 Raman Microscopy**

Figure 2.3 is an illustration of the energy level diagram and the transitions involved in Raman spectroscopy. The Raman spectrum is the result of an inelastic scattering process that involves a change in polarizability of the scattered light of the molecule of interest. The electric field of a laser interacts with the electron density of the molecule and induces a dipole. The scattered light can be observed to be elastically and inelastically. The elastically scattered light is rejected and the inelastically scattered light is observed as the Stokes and Antistokes bands. The energy increase or decrease due to the elastic scattering is related to the so-called irrational energy spacing in the ground electronic state of the molecule. The wave number of the Stokes and anti-Stokes scattering is a direct measure of the irrational energy of the molecule. Thus, the Raman wave number shift is an indication of changes in irrational energy in the sample, which provides the chemical and structural information of materials [Loader, 1970; Long, 1971].

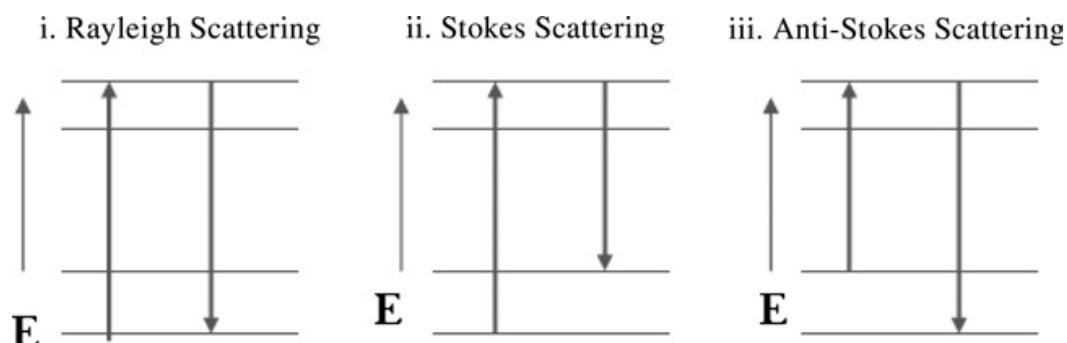


Figure 2.3: Simplified Raman energy level diagram [Skoog et al., 1998].

It is noted that the Stokes and Anti-stokes bands are typically weak and very close to the elastically scattered light (Rayleigh). Thus it is usually difficult to separate Raman bands that are close to the Rayleigh line. Recent developments in filter technology allow for the efficient removal of the Rayleigh band. In some materials, fluorescence occurs when the molecule returns to the electronic ground state from the excited state by emission of a photon. This fluorescence makes it more difficult to detect Raman signal. The use of UV light (244 nm) to excite the sample may help the separation of the Raman signal, as the luminescence in this case will not interfere with the Raman signal. Finally, Raman Microscopes can also be easily reconfigured to work in the luminescence mode to detect full spectra of weak signals.

Raman spectrometers typically use holographic diffraction gratings and multiple dispersion stages to achieve a high degree of laser rejection. The displacement resolution of the dispersion stage of the Raman microscopy used in our study is about 5  $\mu\text{m}$ , which is too large for nano-size carbon nanotubes and may cause random errors.

## **2.7 Adhesion**

Adhesion is defined as the state of two surfaces being held together for an extended period of time by interfacial forces that may consist of valance forces or mechanical interactions or both [Kinloch, 1987]. In the following sections, adhesion theory (Section 2.7.1) and the structure of adhesion materials (Section 2.7.2) will be discussed. Section 2.7.3 discusses adhesion on the surface between a biological object and an inorganic object.

### **2.7.1 Adhesion Theory**

The mechanism of adhesion, ranging from bio-adhesion (involving cell adhesion) to adhesion of heavy construction materials under temperatures from ranging sub-freezing to a few hundred degrees centigrade, has been investigated extensively. Several theories have been proposed in an attempt to provide an explanation for various adhesion phenomena. No single theory applies to all adhesion phenomena; a particular theory may apply only to a limited range. An appropriate theory must be selected for a particular adhesion problem based on the chemical/biochemical nature of that particular adhesive combination. For example, the mechanical anchoring of the adhesive in the pores and the uneven parts of a surface can be explained by the Mechanical Theory; the difference in electric negativities of adhering materials can be explained by the Electrostatic Theory; the adhesion caused by intermolecular forces can be explained by

the Adsorption Theory; the adhesion related to the chemical interactions can be explained by the Chemisorption Theory; the processes that play a role in the bonding of similar types of thermoplastic high-polymer materials can be determined with the Diffusion Theory. These theories can be used, solely or in combination with each other, to describe almost any kind of adhesion phenomenon [Nihlstrand, 1996]. In the following sections, from Section 2.7.1.1 to Section 2.7.1.4, each theory will be discussed, followed by a summary in Section 2.7.1.5.

### **2.7.1.1 Mechanical Theory**

The Mechanical Theory, also called the Mechanical Interlocking Theory, is the oldest explanation for adhesion [McBain et al., 1925]. The theory states that mechanical interlocking of the adhesives and the flow into the irregularity of the substrate surface, i.e., pores, holes, and crevices, is the source of adhesion [Craig et al., 2006]. The adhesive must not only wet the substrate but also have the right properties for penetration into pores and openings within a reasonable time. The viscosity of the adhesive and the contact time with the substrate are important parameters for mechanical adhesion [Kinloch, 1979; 1980; 1987]. Viscosity adhesion occurs by restricted movement due to the viscous nature of the substrates.

Roughness of the interface can increase the adhesion force. There are two methods to increase the roughness of the surfaces: one is mechanical abrasion and the other is chemical treatment. Mechanical abrasion will increase the joint strength

[Jennings, 1972], but such treatments do not generally result in a surface topography with cavities suitable for mechanical interlocking. However, mechanical abrasion can ensure that the substrates are free from machine oil, grease, scale, and so on, which helps remove weak boundary layers and thus enhances adhesion. Chemical treatment such as acid etching can produce a surface topography suitable for mechanical interlocking, provided that proper care is given to ensure that the resulting surface layer is not too weak or friable [Kim, 2000]. High roughness of the surface is conducive to an increase in the energy dissipated viscoelastically and plastically [Evans et al., 1979; Packham, 1981 and 1983; Hine et al., 1984; Bair et al., 1971; Wang et al., 1972].

#### **2.7.1.2 Electrostatic Theory**

The basis of the electrostatic theory of adhesion is the difference in electro negativities of adhesion materials. When the adhesive and substrate have different electron structures, adhesive force is attributed to the transfer of electrons across the interface creating positive and negative charges that attract one another and balance the Fermi levels [Kinloch, 1987]. This kind of transfer will result in an electrical layer at the interface between the adhesive and substrate. Deryaguin et al. [1955; 1957; 1969] suggested that the electrical force caused by contact of different electro negativity materials may contribute to the intrinsic adhesion that resists the separation of the adhesive and substrate. This theory can be viewed as treating the adhesives or substrate system as a capacitor that is charged due to contact of two different materials. Deryaguin's Theory as shown below can be used to represent the Electrostatic Theory:

$$A_c = \left(\frac{h_c \epsilon_d}{8\pi}\right) \left(\frac{dV_c}{dh_c}\right)^2 \quad (2.2)$$

where  $V_c$  is the discharge potential at the discharge gap,  $h_c$  and  $\epsilon_d$  are the dielectric constants, respectively, and  $A_c$  is the adhesive force.

This equation successfully explained some experiments [Deryaguin et al, 1957], but could not explain the peel strength of pressure sensitive tapes when tested in vacuum as opposed to atmospheric pressure [Weidner, 1963]. Also, when it comes to determining the values of the equation, it turns out that an additional equation is needed [Wake, 1982].

A common example often described by the Electrostatic Theory is the adhesion of a plastic film on a layer of paper or another film of plastic.

### **2.7.1.3 Diffusion Theory**

The Diffusion Theory states that adhesion occurs through inter-diffusion of the adhesive and substrate across the interface [Kim, 2000]. It is a result of the solubility of the adhesive to the substrate. Adhesion is considered as a three-dimensional volume process rather than as a two-dimensional surface process. This theory is perfectly acceptable in relation to systems of thermodynamically compatible polymers in the

viscous-flow or high-elastic state during the period of formation of the adhesion bond. Industrial techniques to enhance interfacial diffusion include solvent welding, heat welding, and ultrasonic welding [Tres, 2000]. In solvent welding, a solvent common to both adhesive and substrate is applied to allow diffusion of polymers across the interface. In heat welding, materials are melted to allow interfacial diffusion. In ultrasonic welding, ultrasonic wave is directed through a horn that focuses on the interface to melt a thin layer of materials across the interface. Among these techniques, ultrasonic welding is the most often used method.

#### **2.7.1.4 Adsorption Theory**

The Adsorption Theory is the most widely applied theory on interfacial adhesion [Toth, 2002]. This theory states that in sufficient intimate molecular contact, the materials will adhere because of the interatomic and intermolecular forces. The most common such force is Van der Waals force. Acid-base interactions and hydrogen bonds may also contribute to intrinsic adhesion force [Allara et al, 1986; Fowkes, 1987]. These forces are referred to as secondary forces. Adsorption that results from the universal Van der Waals interactions is called physical adsorption. In addition, a chemical bond called chemisorption may also be formed across the interface. The chemisorption includes ionic, covalent, or metallic interface bonds. These types of bonds are referred to as primary forces. Research has found that the mechanism of adhesion in many adhesive joints involves only secondary forces [Kinloch, 1979; Gledhill et al., 1980]. Defects and other geometric irregularities on the interface can also affect adsorption [Kinloch, 1980].

When two objects are closely in contact, Van der Waals interaction or acid-base interaction or both take place; therefore, an intimate contact can increase the adsorption between two objects.

Physical adsorption is very effective, particularly at a temperature close to the critical temperature of a given gas [Fraissard, 1997]. Chemisorption occurs usually at temperatures much higher than the critical temperature and is a specific process that can take place only on particular solid surfaces for a given gas. Under favourable conditions, both processes can occur simultaneously or alternately [Smith, 1980].

Physical adsorption includes the following stages [Fraissard, 1997]: (1) Molecules diffuse from the bulk phase towards the interface; (2) Molecules diffuse inside the pores; (3) Molecules diffuse on the surface of the pores; and (4) Adsorption/desorption processes at the surface of the pores. In the second stage, diffusion takes place only when the dimensions of the adsorbate molecules are slightly smaller than the pore diameter. Increasing temperatures sometimes can increase the ability of the adsorbate molecules to enter the pores in case where the molecules have insufficient kinetic energy. The diffusion at higher temperatures can reduce the equilibration time.

In biology, the Adsorption Theory is often used to explain protein adsorption, cell adhesion, and cell spreading. There are organic molecules that have been found to



serve as “glue” for biological cells, and these glue molecules are classified into categories such as *Cadherins*, *Selectins*, *Integrins*, and *Ig* superfamily [Scott, 1997].

### **2.7.1.5 Summary**

Adhesion can happen on the interfaces between two materials. There are several theories that can be used to explain the adhesion phenomenon. Sometimes one theory is enough; sometimes several theories need to be used together. In many cases, adsorption happens between two objects when they adhere, so adsorption theory is the more commonly applied theory. The forces of adhesion can be summarized as follows [Lee, 1991]:

- (1) Atoms are held in molecules by covalent and ionic bonds,
- (2) Intermolecular forces hold molecules together in a more condensed manner,
- (3) Intermolecular forces are primarily Coulomb (electrostatic) in nature, and
- (4) Most covalent bonds have a residual charge, or ionic characteristic (i.e., electronegativity).

The basic requirements for achieving good adhesive bonds are:

- (1) An intimate contact between the adhesive and the substrate,
- (2) Removal of weak boundary layers, and
- (3) Avoidance of stress concentration across the adhesive joint.

### **2.7.2 The Structure of Materials in Adhesion**

Many factors can affect adhesion. For example, surface treatment can improve adhesion. Here, we will discuss the structure of materials in adsorption.

In adsorption science, porosity is usually classified into three groups: micropores, mesopores, and macropores (also see previous discussion in Section 2.2). The micropores are defined as pores of a width not exceeding 2 nm, mesopores are pores of a width between 2 and 50 nm, and macropores represent pores of a width greater than 50 nm [Everett, 1973; 1976].

The size of the pores plays an important role in the adsorption processes [Fraissard, 1997]. The adsorbents with pore sizes of micropores are better in adsorption than those with the pore sizes of mesopores and macropores. This is because the size of micropores is comparable to those of adsorbate molecules such that all atoms or molecules of the adsorbent can interact with the adsorbate species. The adsorption in the micropore structure material is basically a pore-filling process in which their pore

volume is the main controlling factor [Dubinin, 1975a, 1975b]. Thus, the essential parameter characterizing micropores is their pore volume per unit weight or surface area per unit weight.

For mesopore structure materials whose walls are occupied by a great number of adsorbent atoms or molecules, the mono- and multilayer adsorption takes place on the surface of the walls according to the mechanism of capillary adsorbate condensation [Oscik, 1982]. The basic parameters characterizing mesopores are: specific surface area, pore volume, and pore-size or pore-volume distribution.

The adsorption on the surface of macropores does not differ from that on flat surfaces [Fraissard, 1997]. As the specific surface area of macroporous solids is very small, the adsorption on this surface is usually neglected. Capillary adsorbate condensation does not occur in macropores.

### **2.7.3 Adhesion between Biological and Inorganic Interface**

The adhesion between biological and inorganic objects, specifically, peptide adhesion to inorganic materials, has generally involved use of complex biological components. Peptides were found to selectively adhere to certain metallic [Brown, 1997] and semiconductor [Whaley, 2000] surfaces. The adhesion of amino acid to inorganic surfaces such as metal, insulators, and semiconductors decreases with an increase of pH in solutions [Willett et al, 2005]. Formation of an intermediary layer on inorganic

surfaces can lead to adhesion between biological and inorganic surfaces. Various methods [Wagner et al., 1997; Veiseh, et al., 2002; Gleason. et al., 2003; Alireza et al., 1999] have been used to produce an intermediary layer on inorganic materials, including self-assembled monolayers that contain cell binding agents that bind to biological materials [Yeo et al., 2003].

Recently, carbon nanotubes have been investigated in biological applications. Because of its nano size, carbon nanotubes have potential applications in drug delivery. In many instances, a cell membrane will break down proteins transported via endocytosis, a process that cells use to transport a variety of molecules into the cell, but the nanotube-bound proteins avoid this fate if they are delivered along with a small amount of antimalarial drug such as *chloroquine* [Kam et al., 2005]. Although the toxicity of carbon nanotube to mammals is still under research, cutting-edge research such as the use of carbon nanotubes in protein attachment has been of great interest in looking for nano-size protein carriers.

In order to create adhesion force between the bimolecular and nanotubes, bimolecular should be located close to the carbon nanotubes. This attachment can be through either of non-covalent interaction or covalent bonding. The best stability and selectivity, however, will be achieved through covalent bonding because this kind of adhesion can control the bimolecular location, improve stability and selectivity, and reduce leaching. The common steps for achieving covalent bonding between nitrogen-

doped multi-walled carbon nanotubes (CNx MWNTs) and biomolecules are as follows (Figure 2.4) [Jiang et al., 2004]:

- (1) CNx MWNTs are acid-oxidized to form carboxylic acid groups on the surface of the carbon nanotubes.
- (2) The carboxylic acid groups are activated by *N-ethyl-N'-(3-dimethylaminopropyl) carbodiimide hydrochloride* (EDAC), forming a highly reactive *O-acylisourea* active intermediate.
- (3) EDAC treated CNx MWNTs are stabilized by presenting *N-hydroxysuccinimide* (NHS), and a more stable active ester (succinimidyl intermediate) can be formed.
- (4) The active ester undergoes nucleophilic substitution reaction with the amine groups on proteins, resulting in the formation of an amide bond between the CNx MWNTs and proteins.

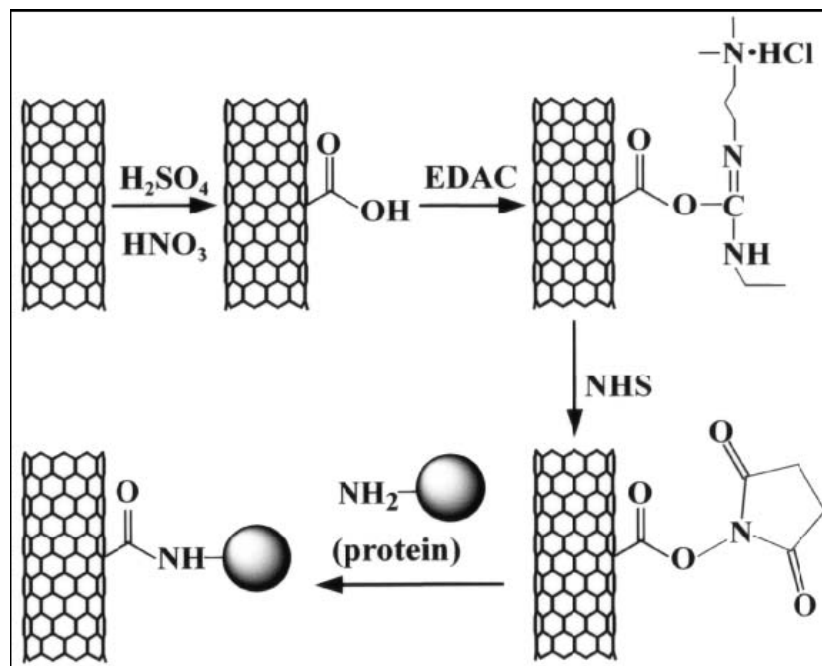


Figure 2.4: Schematic view of the attachment of proteins to carbon nanotubes [Jiang et al., 2004].

## 2.8 Brownian Motion

In 1827, Robert Brown observed pollen grains of some flowering plants through a microscopy. To his surprise, he noticed that tiny particles suspended within the fluid of pollen grains were moving in a haphazard fashion. Brown repeated his experiment with other fine particles, including the dust of igneous rocks, a highly inorganic material. He found that any fine particle that suspends in water executes a similar random motion. This phenomenon was named Brownian motion. It is now known that the Brownian motion of particles in a liquid is due to an instantaneous imbalance in the force exerted by the small liquid molecules on the particle.

Assume at  $t=0$  a particle had  $\mathbf{r}(0)=0$ . We can calculate its velocity at the time  $t$  [Karatzas et al., 1988; Don et al., 2002; Huang, 2005]:

$$\frac{d\mathbf{v}(t)}{dt} = -\lambda\mathbf{v}(t) + \mathbf{f}(t) \quad (2.3)$$

where  $\mathbf{v}(t)$  is the velocity,  $\lambda$  is the friction coefficient, and  $\mathbf{f}(t)$  is the random force acting on the particle. The friction force is proportional to the velocity with constant  $\lambda$ . Because force  $\mathbf{f}(t)$  is random in its nature, it should be expressed as a random variable. The probability distribution function (i.e.,  $P$ ) of the force  $\mathbf{f}(t)$  can be represented by the equation below [Karatzas et al., 1988; Don et al., 2002; Huang, 2005]:

$$P[\mathbf{f}(t)] \propto \exp\left(-\alpha \int_0^t dt \mathbf{f}(\tau)^2\right) \quad (2.4)$$

where  $\alpha$  is a constant related to friction and temperature,  $\alpha = \frac{1}{kT\lambda}$ , where  $k$  is a Boltzmann constant, and  $T$  is the temperature at equilibrium. Note that Equation 2.4 is actually a Gaussian distribution. Therefore, the mean force is zero.

From Equation 2.3:

$$\frac{d(\mathbf{v}(t)\exp(\lambda t))}{dt} = \mathbf{f}(t)\exp(\lambda t) \quad (2.5)$$

Integrate above Equation 2.5:

$$\mathbf{v}(t) \exp(\lambda t) - \mathbf{v}_o = \int_0^t \mathbf{f}(\tau) \exp(\lambda \tau) d\tau \quad (2.6)$$

From Equation 2.6, it is easy to get the solution for Equation 2.3:

$$\mathbf{v}(t) = \mathbf{v}_o \exp(-\lambda t) + \exp(-\lambda t) \int_0^t \mathbf{f}(\tau) \exp(\lambda \tau) d\tau \quad (2.7)$$

The solution for  $\mathbf{r}(t)$  is:

$$\mathbf{r}(t) = \int_0^t \mathbf{v}(\tau) d\tau \quad (2.8)$$

Integration of the first term in Equation 2.7 gives:

$$\int_0^t \mathbf{v}_o \exp(-\lambda \tau) d\tau = \frac{1}{\lambda} \mathbf{v}_o (1 - \exp(-\lambda t)) \quad (2.9)$$

Integration of the second term in Equation 2.7 gives:



$$\begin{aligned}
& \int_0^t [\exp(-\lambda\tau) \int_0^\tau \mathbf{f}(\rho) \exp(\lambda\rho) d\rho] d\tau = \\
& -\frac{1}{\lambda} \exp(\lambda\tau) \int_0^\tau \mathbf{f}(\rho) \exp(\lambda\rho) d\rho \Big|_0^t + \frac{1}{\lambda} \int_0^t \mathbf{f}(\tau) d\tau = \\
& \frac{1}{\lambda} \int_0^t (1 - \exp(\lambda(\tau - t))) \mathbf{f}(\tau) d\tau
\end{aligned} \tag{2.10}$$

Then:

$$\mathbf{r}(t) = \frac{1}{\lambda} \mathbf{v}_o (1 - \exp(-\lambda t)) + \frac{1}{\lambda} \int_0^t (1 - \exp(\lambda(\tau - t))) \mathbf{f}(\tau) d\tau \tag{2.11}$$

Notice that the average velocity and displacement of the particle are zero, but the instant velocity can be quite large. Therefore, the particle can actually move quite far.

## 2.9 Feedback Control System

The general configuration of a feedback control system is shown in Figure 2.5. In this figure, the plant is a target object or system to be controlled, while the controller is to instruct and regulate the plant such that its performance can reach its desired output. In Figure 2.5,  $x_p$  is the input to the plant;  $y_p$  is the output of the plant;  $x_c$  is the input to the controller;  $y_c$  is the output of the controller;  $y_p^d$  is the desired output of the plant; and  $d$  is the disturbance to the controller as well as to the plant. There are relations between  $y_p$  and  $x_p$  and between  $y_c$  and  $x_c$ , respectively, that are assumed to be known with respect to the controller. The controller is, in essence, a mathematical expression that takes  $x_c$ ,

$y_p^d$ , and  $d$  as independent variables, and  $y_c$  as the dependent variable. The simplest controller is expressed as follows:

$$y_c = k_p ||y_p - y_p^d|| \quad (2.12)$$

where  $k_p$  is a given constant; how to determine  $k_p$  is out of the scope of discussion here.

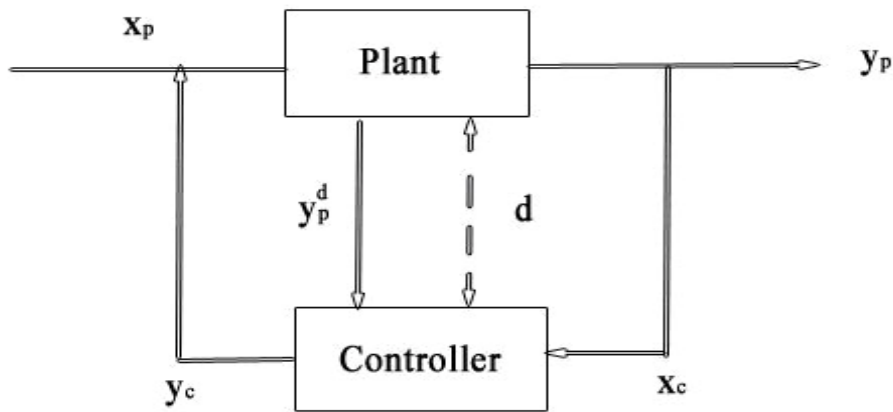


Figure 2.5: General configuration of a feedback control system.

As one can imagine the controller may not only concern  $y_p$ , but also concern how  $y_p$  is obtained, namely the relation between  $x_p$  and  $y_p$ . When the controller takes the  $x_p - y_p$  relation into consideration, the plant and controller are integrated in the sense that the expression of the controller will include two categories of parameters ( $k_p$  in Equation 2.12 and the  $x_p - y_p$  relation). This thus implies that the plant and the controller can be merged into one, which is then called a controlled system (or control system); see Figure 2.6.

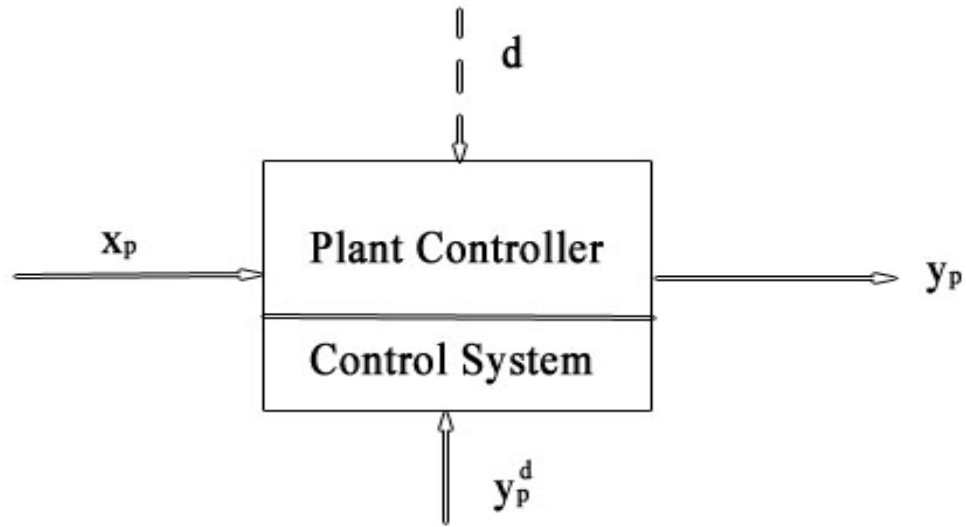


Figure 2.6: State-space control system.

The most convenient method for expressing the control system is called the state-space approach. In a state space system, the internal state of the system is represented by an equation known as the state equation. The system output is given in terms of a combination of the current system state, and current system input, by the output equation. These two equations form a system of equations known as the state-space equations. The state-space is the vector space that consists of all the possible internal states of the system. The state-space approach is valid for both linear and nonlinear systems.

In a state-space system representation, we use  $\mathbf{y}(t)$  as the output of the system,  $\mathbf{x}(t)$  as the state of the system, and  $\mathbf{u}(t)$  as the input of the system. We use the notation  $\mathbf{x}'(t)$  to denote the first order derivative of the state vector of the system, as dependant on

the current state of the system and the current input. The following are mathematic expressions of  $\mathbf{x}'(t)$  and  $\mathbf{y}(t)$ :

$$\mathbf{x}' = g[t_o, t, \mathbf{x}(t_o), \mathbf{u}(t)] \quad (2.13)$$

$$\mathbf{y}(t) = h[t, \mathbf{x}(t), \mathbf{u}(t)] \quad (2.14)$$

Equation 2.13 shows that the system state is dependent on the previous system state, the initial state of the system, initial time, present time, and system inputs. Equation 2.14 shows that the system output is dependent on the current system state, system input, and present time. If  $\mathbf{x}'(t)$  and  $\mathbf{y}(t)$  are linear combinations of the system state and input vectors, we say that the systems are linear systems, and we can rewrite them in a matrix form:

$$\mathbf{x}'(t) = \mathbf{A}(t)\mathbf{x}(t) + \mathbf{B}(t)\mathbf{u}(t) \quad (2.15)$$

$$\mathbf{y}(t) = \mathbf{C}(t)\mathbf{x}(t) + \mathbf{D}(t)\mathbf{u}(t) \quad (2.16)$$

If the systems are also time-invariant, we can re-write this as follows:

$$\mathbf{x}'(t) = \mathbf{A}\mathbf{x}(t) + \mathbf{B}\mathbf{u}(t) \quad (2.17)$$

$$\mathbf{y}(t) = \mathbf{C}\mathbf{x}(t) + \mathbf{D}\mathbf{u}(t) \quad (2.18)$$

Equation 2.18 shows that for a given system, the current output is dependent on the current input to the system and the current state of the system. Equation 2.17 shows the relationship between the current state of the system, input to the system, and future state of the system.

# **CHAPTER 3**

## **USING CARBON NANOTUBE TO ADSORB HYDROGEN SULFIDE IN WATER SOLUTION**

### **3.1 Introduction**

Activated carbon is well known as an excellent absorbent to H<sub>2</sub>S in oil, gas, and waste water. The most important property of activated carbon that is related to adsorption of H<sub>2</sub>S is the pore structure of activated carbon. Further, its pore structure causes activated carbon to have an extraordinarily large surface area per unit weight, which is a major factor responsible for activated carbon's unique role. By comparison to activated carbon, carbon nanotube also has a large surface area per unit weight, which leads to the concept of using carbon nanotube as an absorbent to H<sub>2</sub>S in water solution with a particular potential to adsorb low concentration and nano quantity H<sub>2</sub>S in the biological cell. This concept is further supported by some other excellent properties of carbon nanotube, including high strength, good thermal conductivity, and good electrical transport capability.

This chapter describes an experimental study to prove the concept of using carbon nanotube to adsorb H<sub>2</sub>S. For this purpose, the binding behaviour of carbon

nanotube with H<sub>2</sub>S was primarily examined using Raman and confocal laser scanning microscopes.

In particular, Section 3.2 discusses the materials and methods used in this experiment. Section 3.3 discusses results and discussion, including a discussion of the underlining mechanism of the adsorption between H<sub>2</sub>S and carbon nanotube. Section 3.4 comments on related work. Section 3.5 provides a conclusion. The content of this chapter has been published [Wu et al., 2006].

## **3.2 Materials and Methods**

In the following, Section 3.2.1 and Section 3.2.2 describe the preparation of the carbon nanotube and H<sub>2</sub>S, respectively. Section 3.2.3 describes the data acquisition methods and instruments. Section 3.2.4 describes the experimental procedure.

### **3.2.1 Carbon Nanotube Acquisition**

The carbon nanotubes in a powder form were provided by Engineering Physics and Physics Department at University of Saskatchewan. In particular, these powder form carbon nanotubes were prepared by using a Microwave Plasma Enhanced Chemical Vapour Deposition (MPECVD) reactor in a gas mixture of hydrogen and methane [Yang et al., 2002], The schematic of the reactor is shown in Figure 3.1. In this figure, the substrate stage consists of an inconel 600 plate and a stainless steel substrate holder plate

separated by a 5.3 cm long quartz tube. Carbon nanotubes were deposited on the inconel substrate located at the low part of the substrate stage. In this process, the temperature was approximately 550 °C for the Si substrate and 350 °C for the inconel substrate. The deposition conditions are summarized in Table 3.1.

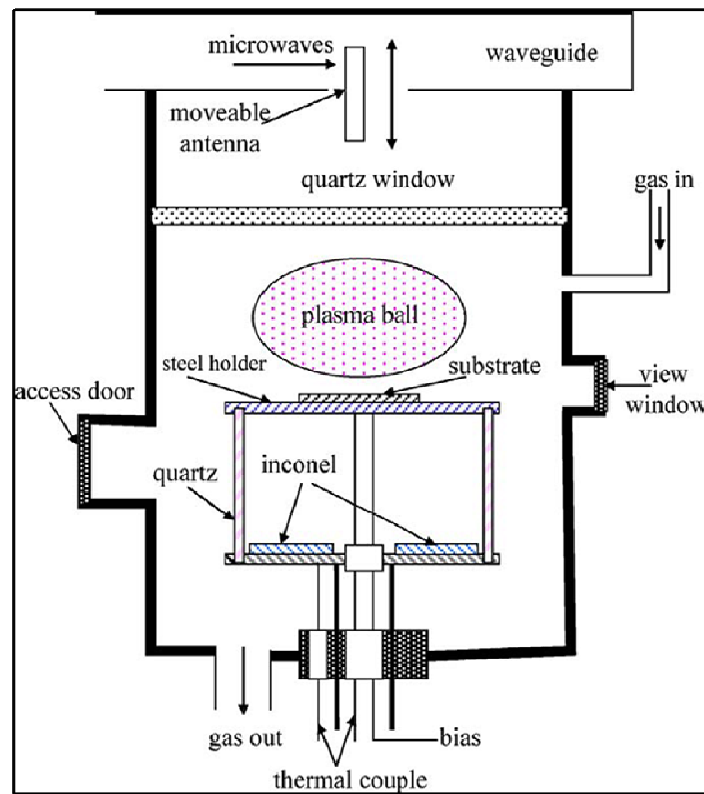


Figure 3.1: Chemical vapor deposition system [Yang et al., 2002].



Table 3.1: Carbon Nanotube Growth Conditions.

<b>Growth parameters</b>	<b>Typical value</b>
Microwave power (W) at 2.45 Hz	1000
Substrate temperature (°C)	350
Methane concentration (vol.%)	1
Bias voltage (V)	-100
Gas flow rate (sccm)	100
Deposition pressure (Torr)	30
Substrate	inconel
Gas mixture	H <sub>2</sub> + CH <sub>4</sub>

The powder form carbon nanotubes were observed by Philips CM-10 transmission electron microscopy (TEM) at 60 kV bright field mode; see Figure 3.2. The diameters of the carbon nanotubes shown in Figure 3.2 are about 25 nm, and their inner diameters are approximately 5 nm. From Figure 3.2, it can be seen that the carbon nanotubes are curved, long tubes with lengths up to submillimeter scale. The high resolution TEM observation further reveals the multi-wall structures of these nanotubes. It is noted that the TEM sample of carbon nanotube was prepared by putting carbon nanotubes in distilled water and sonicating them for 1 minute. A drop of sonicated solution was put on the TEM copper grids with formvar and dried before using TEM.

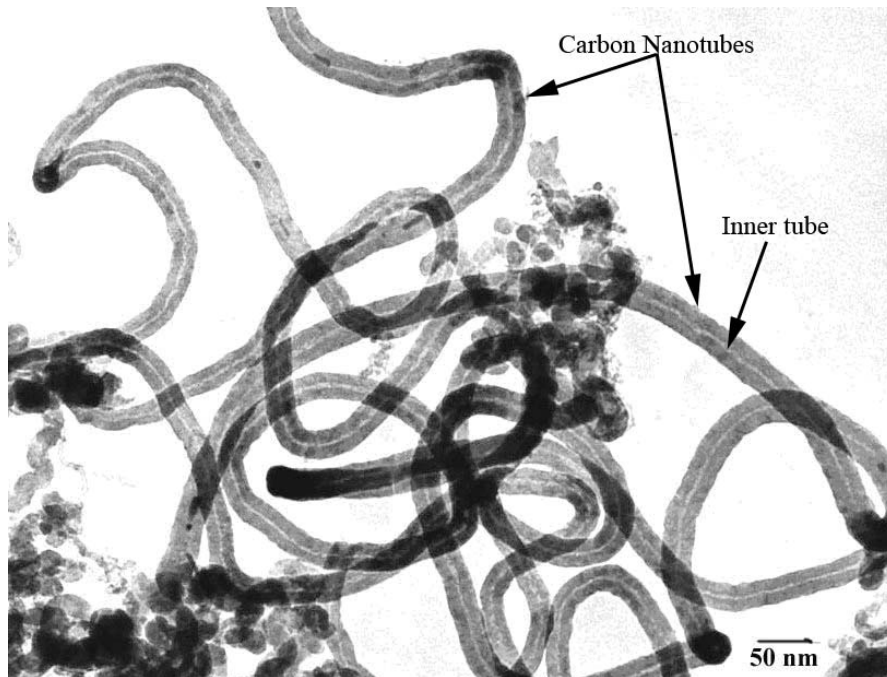


Figure 3.2: TEM image of carbon nanotubes.

Another supply of carbon nanotubes for this experiment was provided by the Saskatchewan Structure Sciences Center (SSSC) at the University of Saskatchewan. Unfortunately, the specification of this carbon nanotube was unknown at the time of this experiment, except for the information that these carbon nanotubes were in a powder sheet form.

In the following discussion, the carbon nanotube prepared with the MPECVD approach (i.e., the one shown in Figure 3.2) is called sample A; while the carbon nanotube supplied by SSSC is called sample B.

### 3.2.2 H<sub>2</sub>S Preparation

H<sub>2</sub>S gas-saturated solution (90 mM at 30°C) was made by bubbling pure H<sub>2</sub>S gas (Praxair, Mississauga, ON) into 40 mL of distilled water at 30 °C and 10 psi (pounds per square inch, 1 atm = 760 mmHg = 14.7 psi) for 30 minutes. The H<sub>2</sub>S gas-saturated solution was freshly prepared on the day of the measurement. NaOH solution (300 ml) was used to trap the extra H<sub>2</sub>S gas. The equipment was gas-tight sealed.

Direct measurement of H<sub>2</sub>S concentration was made by using a sulfide sensitive electrode (Model 9616, Orion Research, Beverly) on a Fisher Accumet AR50 pH meter (Fisher Scientific, Pittsburgh, PA) following the manufacturer's direction. Standards were prepared from Na<sub>2</sub>S stock solution, which was freshly prepared on the day of the measurement. The exact concentration of the stock solution was determined by titrating 10 ml of the standard with 0.1 M lead perchlorate. The linear range of the sulfide sensitive electrode was greater than 0.32 ppm (parts per million, 1 ppm = 31.12 μmol/litre S<sup>2-</sup>) or 10<sup>-5</sup> M (mole/litre) S<sup>2-</sup>.

Lower concentration (μM level) H<sub>2</sub>S solutions were diluted from 90 mM H<sub>2</sub>S solution into the samples as follows: 10 μM, 20 μM, 30 μM, 40 μM, 50 μM, and 100 μM.

### **3.2.3 Data Acquisition**

Laser Scanning Microscopy (ZEISS LSM 510 META) was used to measure the fluorescence of the powder form carbon nanotubes to confirm whether carbon nanotube binds with H<sub>2</sub>S. The selected excitation wavelength was 514 nm. The emission wavelengths were in a range from 539 nm to 753 nm. A water immersed 25× objective was used in the experiment. In order to get the intensity versus time curve, the time series function available with the confocal laser scanning microscopy was employed.

Raman Microscopy (Renishaw system 2000) was also used to measure the luminescence of the samples for the same purpose of confirming whether carbon nanotube binds with H<sub>2</sub>S. In the Raman measurement, the selected excitation wavelength was 514 nm and emissions wavelengths were in a range from 518 nm to 800 nm.

### **3.2.4 Procedure**

For sample A, 1.6 mg powder form carbon nanotubes were immersed in 100 μL distilled water; 10 μM, 20 μM, 30 μM, 40 μM, 50 μM, and 100 μM H<sub>2</sub>S solutions, respectively, for 2 minutes, and the resulting carbon nanotubes were dried at room temperature for 30 minutes. It is noted that for each of these concentrations, a different powder form carbon nanotube was used. In this experiment, for each sample, thirty

different spots were measured, and each spot was measured thirty times in one minute with the time series function available with the confocal laser scanning microscopy.

For sample B, carbon nanotubes in sheet form were cut into small pieces for Raman microscopy measurement. Different pieces of carbon nanotube sized from 2 to 3 mm were immersed into 100  $\mu\text{L}$  distilled water, 50  $\mu\text{M}$  and 100  $\mu\text{M}$   $\text{H}_2\text{S}$  water solutions, respectively, for 2 minutes, and the resulting carbon nanotubes were dried at room temperature for 30 minutes.

It is noted that sample A was measured by laser scanning microscopy and sample B was measured by Raman microscopy. While, there is no restriction for measuring sample A by Raman microscopy and sample B by laser scanning microscopy, it should be mentioned that Raman microscopy may not be able to measure the 10  $\mu\text{M}$  differences because its resolution is lower than that of the confocal laser scanning microscopy for the particular measurement task here.

### **3.3 Results and Discussion**

In this section, results from the Raman microscopy (Section 3.3.1) and the confocal laser scanning microscopy (Section 3.3.2) will be presented. The statistic analysis of the data from the laser scanning microscopy will be presented in Section 3.3.3. The mechanism of the adsorption between  $\text{H}_2\text{S}$  and carbon nanotubes is discussed in Section 3.3.4.

### 3.3.1 Results from Raman Microscopy

The result of sample B with Raman microscopy is shown in Figure 3.3. The fluorescence increased with the increase of the immersed  $\text{H}_2\text{S}$  concentration. In this figure, y axis represents the photons received by the Raman and the x axis is the wavelengths from 518 nm to 800 nm.

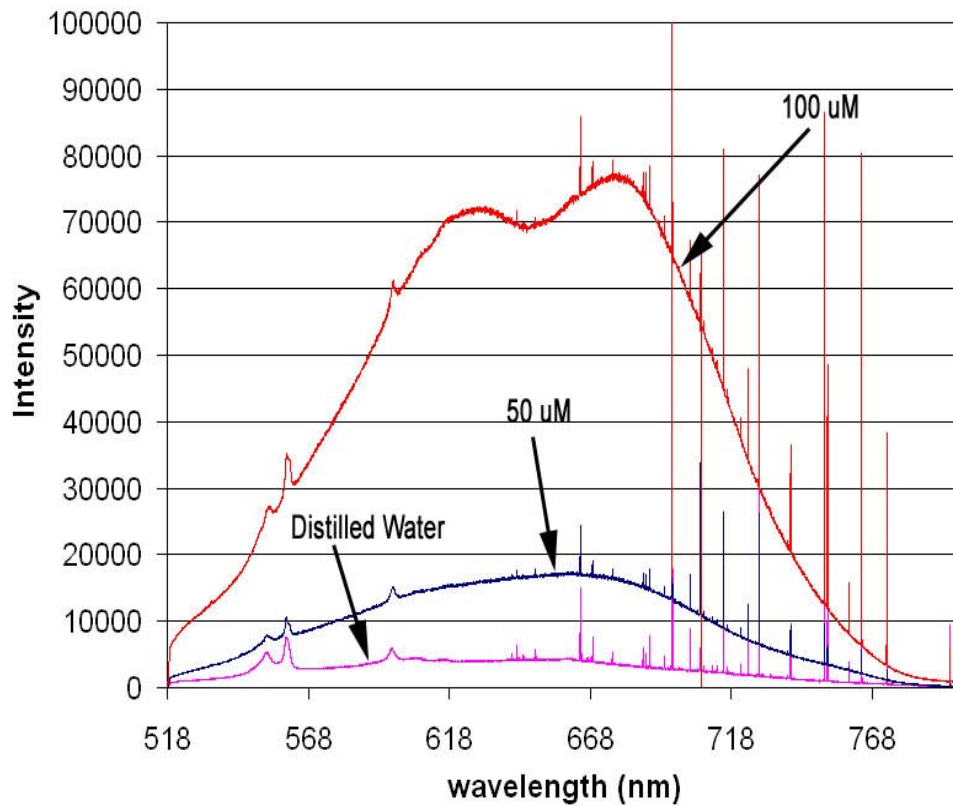


Figure 3.3: Raman luminescence of carbon nanotube treated with different concentrations of  $\text{H}_2\text{S}$  in water.

### 3.3.2 Results from Laser Scanning Microscopy

The result of sample A with confocal laser scanning microscopy is shown in Figure 3.4. In this figure, the emitted fluorescence intensities from the carbon nanotubes after being immersed in H<sub>2</sub>S water solutions increase with the increase of concentration of H<sub>2</sub>S in the water solution.

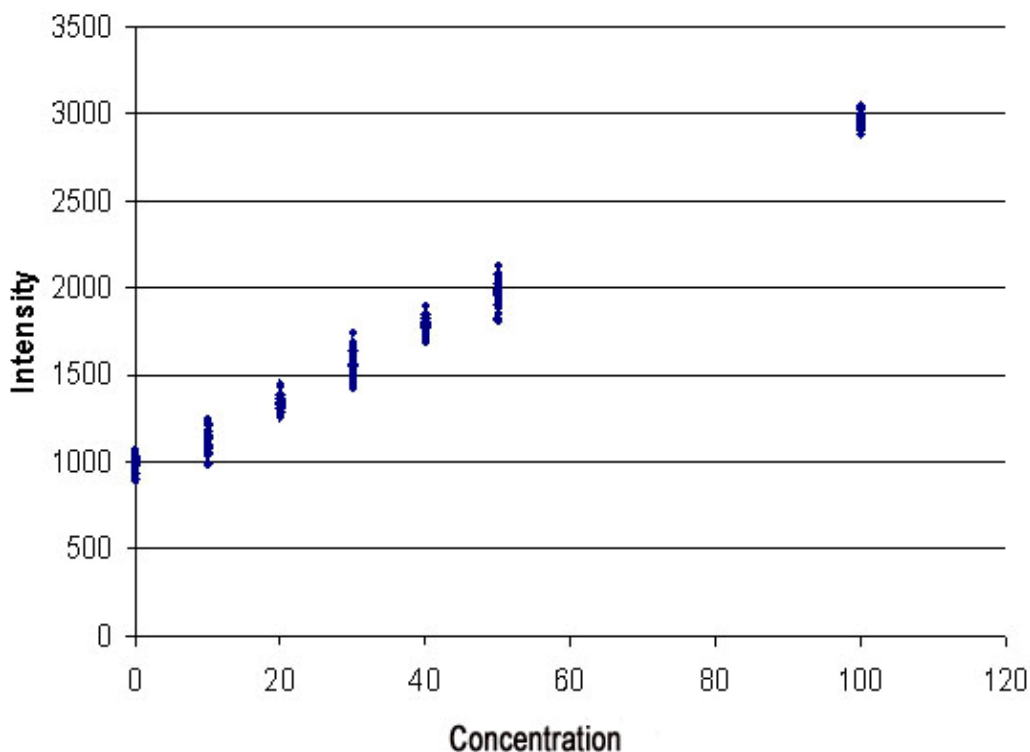


Figure 3.4: Confocal laser scanning microscopy fluorescence of the carbon nanotubes treated with distilled water and with different concentrations of H<sub>2</sub>S in water, respectively. The 30 different spots were measured for each sample. Each spot was measured 30 times. In this figure, there are 30 points which correspond to each concentration (0 μM, 10 μM, 20 μM, 30 μM, 40 μM, 50 μM, and 100 μM, respectively). Each point was the average of 30 times' measurement.

### 3.3.3 Binding of Carbon Nanotube and H<sub>2</sub>S in H<sub>2</sub>S Water Solutions

From the results shown in Figure 3.3 and Figure 3.4 as well as the procedure of the experiment, it can be understood that the intensity of both the Raman luminescence and laser scanning fluorescence is sensitive to the concentration of H<sub>2</sub>S – in particular the intensity increases with respect to the increase of the concentration of H<sub>2</sub>S (or the amount of H<sub>2</sub>S due to the same amount of distilled water used for all these samples with different H<sub>2</sub>S concentrations). It is further noted that carbon nanotubes can also induce the luminescence in Raman and fluorescence in confocal laser scanning microscopy. Therefore, the intensity as shown in Figure 3.3 and Figure 3.4 is a mixture of intensities of carbon nanotube and H<sub>2</sub>S. However, during the experiment, the same type of carbon nanotube was used, which can reasonably imply that the increase of the intensity was contributed by the increase of the amount of H<sub>2</sub>S.

In the whole experiment, there was also an assumption that the carbon nanotubes will never reach a saturated state. This assumption was made validity by making sure that when the amount of H<sub>2</sub>S increased the intensity increased. Furthermore, this assumption can always be ensured by having a sufficient amount of carbon nanotubes to interact with H<sub>2</sub>S.



### 3.3.4 Statistic Analysis of the Results from Laser Scanning Microscopy

The regression and the residual analysis were further performed on different H<sub>2</sub>S concentration samples. The regression analysis was aimed at establishing a relationship between the concentration of H<sub>2</sub>S and the fluorescence intensity. After regression analysis, the one factor ANOVA (ANalysis Of VAriance between groups) (Table 3.2), line fit plot (Figure 3.5), Residual plot (Figure 3.6), and Normal probability plot (Figure 3.7) were produced.

In Table 3.2, “df” indicates the degrees of freedom; “SS” indicates the sum of the squares of the error; “MS” indicates the values of the mean squares, calculated by SS/df; “F” indicates the F-value computed by the ratio of the MS between groups (Regression) to the MS within groups (Residual); and “Significance F” indicates the value at which the null hypothesis may be rejected, and the smaller value of F indicates the greater significance.

Table 3.2: ANOVA for Linear Relationship between H<sub>2</sub>S Water Solution Concentrations and Fluorescence Intensities.

	<b>df</b>	<b>SS</b>	<b>MS</b>	<b>F</b>	<b>Significance F</b>
Regression	1	79864557.09	79864557.09	20210.70658	3.804 x 10 <sup>-209</sup>
Residual	208	821932.0689	3951.596485		
Total	209	80686489.15			

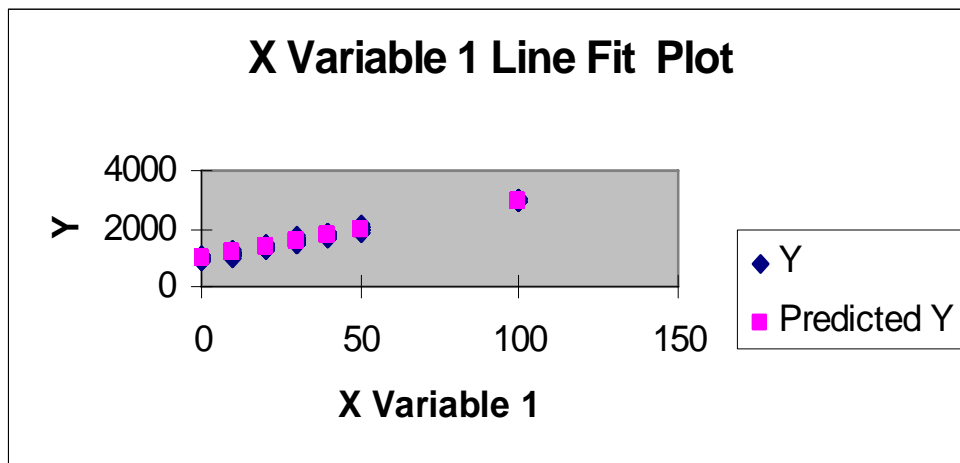


Figure 3.5: Line fit plot in H<sub>2</sub>S water solution. X-axis shows the H<sub>2</sub>S concentrations. Y-axis gives the fluorescence intensity. The small blue diamonds show the measurement for each H<sub>2</sub>S concentration. The small pink squares represent the predicted results for each H<sub>2</sub>S concentration.

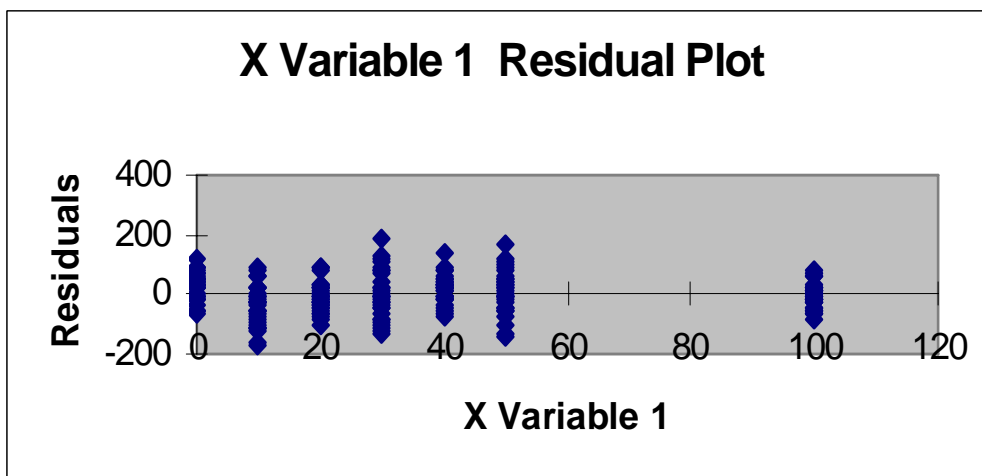


Figure 3.6: Residual plot in H<sub>2</sub>S water solution. X-axis represents the H<sub>2</sub>S concentrations. Y-axis shows the residuals. The small blue diamonds illustrate the residual value between the fluorescence intensity measured and the mean intensity for each H<sub>2</sub>S concentration.

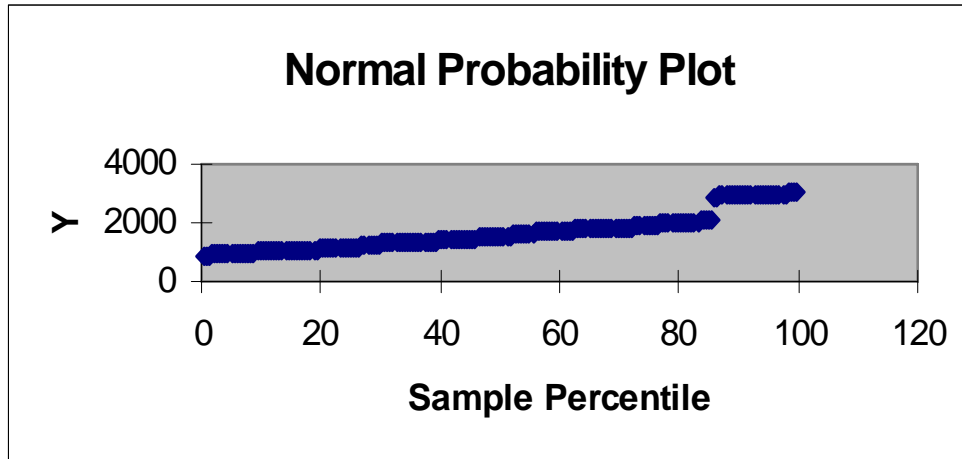


Figure 3.7: Normal probability plot in H<sub>2</sub>S water solution. It shows the distribution of the samples. This is a normal distribution as the links among small blue diamonds are almost linear.

From the line fit plot (Figure 3.5), it can be found that the relationship between fluorescence intensity and H<sub>2</sub>S concentration is linear and satisfies Equation 3.1 as follows:

$$y = 953.52 + 20.13x \quad (3.1)$$

where y refers to the fluorescence intensity and x refers to the H<sub>2</sub>S concentration.

The normal probability plot (Figure 3.7) extends the linear relationship between different H<sub>2</sub>S concentrations and their corresponding intensities. The F value in Table 3.2 indicates that there is a significant intensity difference between different H<sub>2</sub>S concentrations.

### 3.3.5 Mechanism of the Adsorption of H<sub>2</sub>S with Carbon Nanotube

The following is a proposed mechanism that accounts for the adsorption of H<sub>2</sub>S with carbon nanotube, which is adapted from the mechanism which accounts for the adsorption of H<sub>2</sub>S with activated carbon, proposed by Hedden et al. [1976].

In the course of binding H<sub>2</sub>S with carbon nanotube, a series of chemical reactions happen as follows:



The following is a description of physical activities that occur associated with the chemical reactions.

When carbon nanotubes are in the H<sub>2</sub>S solution, a thin water film is formed. Oxygen is dissolved on the film, and oxygen molecules are adsorbed on the carbon nanotubes and become reactive points. Under Van der Waals force, H<sub>2</sub>S can move toward carbon nanotubes, which looks like a physical adsorption.

The H<sub>2</sub>S that reaches the carbon nanotube is also dissolved on the film, and the H<sub>2</sub>S molecule is partly dissociated into proton and hydrosulfide ion (see Equation 3.2). The hydrosulfide ion (HS<sup>-</sup>) then reacts with the oxygen at the reactive points to form hydroxyl ions and sulfur (see Equation 3.3). The sulfur is further attached to the carbon nanotube. The protons (H<sup>+</sup>) neutralize the hydroxyl ions and produce water (see Equation 3.4). The series of physical activities followed by the series of chemical activities represented by Equations 3.2 to 3.4 look like a chemical adsorption.

In short, the binding of H<sub>2</sub>S with carbon nanotube involves a mix of activities that are accounted for both the mechanical adhesion theory and the adsorption theory (see the discussions in Section 2.7).

To verify the above mechanism, GC/MS spectroscopy was used to examine a possible adsorption of H<sub>2</sub>S directly with carbon nanotubes [Wu et al., 2006]; this was done by increasing the temperature of the reaction chamber of GC/MS up to 600°C. There was no H<sub>2</sub>S peak found during the examination, which suggests that the H<sub>2</sub>S molecules do not bind with carbon nanotube directly.

Another support for the proposed mechanism is the examination of the treated carbon nanotubes with TEM (JEOL 2000 FX) and EDS (Genesis version 3.5 from EDAX Inc.). Figure 3.8a shows the TEM image of the treated carbon nanotubes. From this figure, it can be concluded that small particles are attached to the surfaces of the

carbon nanotubes evenly. It is noted that these small particles cannot be seen on the untreated carbon nanotubes (Figure 3.2). The qualitative measurement of TEM and EDS has no evidence of sulfide on untreated carbon nanotubes; however, TEM with EDS has shown that the attached particles on treated carbon nanotubes were sulfur (Figure 3.8b). In Figure 3.8, The Cu-peak came from copper grids, O-peak was from air-absorption, Fe-peak was possibly from multi-scattering in TEM the column, C-peak was from the carbon nanotubes, and Cr-peak was from the sample holder. It is further noted that in performing the measurement of TEM with EDS in this case, we tried several points on both untreated and treated carbon nanotubes and found that the results were the same.

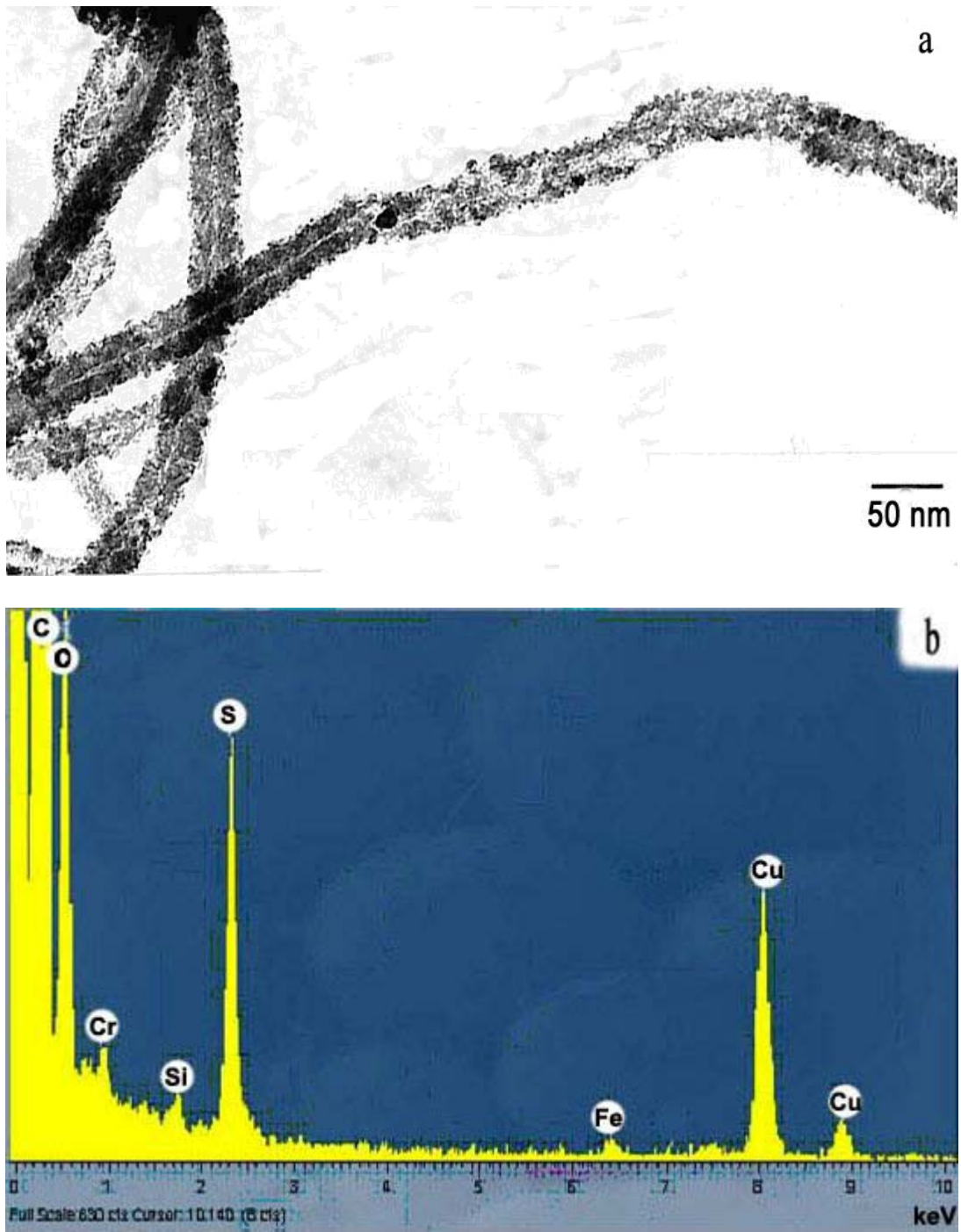


Figure 3.8: TEM image of carbon nanotubes after adsorption of  $\text{H}_2\text{S}$  (a) and the EDS result (b). EDS analyses on carbon nanotubes surface indicate strong S-peak.

### 3.4 Related Work

The use of carbon nanotube to adsorb H<sub>2</sub>S was first reported in this dissertation or in the paper we published on IEEE Transaction on Nanobioscience [Wu et al., 2006]. The mechanism regarding the binding between carbon nanotube and H<sub>2</sub>S has never been reported by others, though there are many studies on the binding between activated carbon and H<sub>2</sub>S [Feng, 2005; Klein et al., 1984; Pilarczyk et al., 1987; Hedden et al., 1976]. The mechanism for the binding between activated carbon and H<sub>2</sub>S is the same as that for the binding between carbon nanotube; such a finding has not been reported by others – especially based on the GC/MS and TEM/EDS instruments.

In a most recent study on the binding behaviour between activated carbon and H<sub>2</sub>S, reported by Feng [2005], the connection of the structure of activated carbon with the binding mechanism has been examined. The study concluded that (1) adsorption of H<sub>2</sub>S onto activated carbon surfaces has two processes: reversible (physical adsorption) and irreversible (chemical adsorption) ones; (2) reversible adsorption is mainly affected by the pore structure; (3) irreversible adsorption is mainly affected by the surface area of activated carbon and the presence of activated carbon which acts like a catalyst to promote the reaction between H<sub>2</sub>S and oxygen.

It should be noted that the study presented in this dissertation has not involved the structural feature of carbon nanotube to the level of details as researched by Feng



[2005] on activated carbon. It is meaningful to study the binding behaviour between carbon nanotube and H<sub>2</sub>S to such a detailed level in order to develop a more effective carbon nanotube system to absorb low concentration and nano-quantity H<sub>2</sub>S.

### 3.5 Conclusions

- (1) The carbon nanotube method can achieve nano-quantity and low concentration H<sub>2</sub>S measurement with conventional energy beams such as those in the confocal laser scanning microscopy and Raman microscopes. Currently, the 10 μM concentration of H<sub>2</sub>S has been measured in water solutions.
- (2) The underlining mechanism behind this method does not limit the possibility of measuring further lower concentrations than 10 μM. By using more accurate instruments, it is likely that much lower concentrations could be measured.
- (3) The carbon nanotube method needs only a trace amount of fluids so it has promise for clinical use and for further development into an *in-vivo*, non-invasive, and real-time continuous H<sub>2</sub>S measurement method.
- (4) The adsorption between H<sub>2</sub>S and carbon nanotube has two steps. The first step is physical adsorption, which is caused by Van der Waals force, and the second step is chemical adsorption. After the second step, sulfur is formed and attached onto the carbon nanotube.

(5) The proposed mechanism that extends what was proposed by Hedden et al. [1976] for the adsorption of  $H_2S$  with activated carbon appears to be valid. Nevertheless, it would be a good future project to measure such a thin film being formed on the carbon nanotube when it interacts with  $H_2S$  in water.

# CHAPTER 4

## MEASUREMENT OF HYDROGEN SULFIDE IN SERUM USING CARBON NANOTUBES

### 4.1 Introduction

The results from Chapter 3 show that carbon nanotube can adsorb H<sub>2</sub>S in an aqueous condition. Raman microscopy and confocal laser scanning microscopy can be used to measure the adsorption between H<sub>2</sub>S and carbon nanotube. The concentration resolution in water that can be measured by confocal laser scanning microscopy is down to 10 μM. In this chapter, carbon nanotubes are used to measure the H<sub>2</sub>S concentrations in sera.

It is known that there are many different proteins in sera, and existing studies in literature have shown that functionalized single-wall carbon nanotubes could be protein carriers. Two important issues of the study described in this chapter were, thus, (i) whether the proteins could be adsorbed by the multi-wall non-functionalized carbon nanotubes (i.e., those used in adsorbing H<sub>2</sub>S in water discussed in Chapter 3) and (ii) whether the H<sub>2</sub>S adsorption could be measured by carbon nanotubes with again the help of confocal laser scanning microscopy and Raman microscopy. Since the binding of

carbon nanotube with H<sub>2</sub>S in distilled water has been confirmed with the Raman and confocal laser scanning microscopes, the underlying purpose of addressing these two issues is to see whether proteins in sera could also bind with the non-functionalized carbon nanotubes used for distilled water.

To address these two issues, proteins in sera were measured before and after carbon nanotube interacts with H<sub>2</sub>S in sera. Raman and confocal laser scanning microscopes were then used in the study described in this chapter to examine the adsorption behaviour between H<sub>2</sub>S and carbon nanotubes. Details of materials and methods for the experiment are presented in Section 4.2. The measurement results will be presented in Section 4.3. Section 4.4 discusses the underlying mechanism. Section 4.5 discusses related work. Section 4.6 is a conclusion. The content of this chapter has been published [Wu et al., 2007].

## **4.2 Materials and Methods**

Section 4.2.1 describes the preparation of carbon nanotubes and the H<sub>2</sub>S measurement. Section 4.2.2 describes the measurement of proteins in sera. Section 4.2.3 describes the confocal laser scanning microscopy measurement. Section 4.2.4 describes the Raman microscopy measurement. Section 4.2.5 describes the Raman microscopy measurement of hemoglobin samples.

#### **4.2.1 Preparation of Carbon Nanotubes**

In the experiments described in this chapter, multi-wall carbon nanotube samples were used, and they were acquired from the Department of Engineering Physics and Physics of the University of Saskatchewan – the same situation as discussed in Chapter 3. These carbon nanotubes were further purified at 450 °C in vacuum until there was no further weight loss with the carbon nanotubes. A typical Transmission Electron Microscopy (TEM) image of these carbon nanotubes is shown in Figure 3.2. The TEM image shows that the outer diameter of the nanotube is about 25 nm and the inner diameter is about 5 nm.

#### **4.2.2 Measurement of Proteins in the Serum**

The serum sample was separated into two equal parts (each part 300 µL): one was used as a control sample and the other was used as a treated sample. The 1.6 mg carbon nanotubes were immersed into the treated sample, and were left overnight until all the carbon nanotubes were at the bottom of the vial. The serum in treated sample was then taken out from the top of the treated sample for protein measurement.

The proteins measured in the serum were: total protein, albumin, alpha1-globulin, alpha2-globulin, beta globulin, and gamma globulin. The total protein and albumin protein were measured colourimetrically by spectrophotometry on the

synchrotron LX20 (Beckman, Palo Alto, CA). Immunoglobulin, including alpha1-globulin, alpha2-globulin, beta globulin, and gamma globulin, were quantified by electrophoresis analyses using the Array™ Protein System (Beckman Instruments Inc. Brea, CA). In the spectrophotometry and electrophoresis analyses, the minimum quantities that could be detected for the total protein, albumin, alpha1-globulin, alpha2-globulin, beta globulin, and gamma globulin were 30, 10, 0.1, 0.1, 0.1, and 0.4 g/L, respectively. The coefficients of variance (the degree to which a set of data points varies) for the total protein, albumin, alpha1-globulin, alpha2-globulin, beta globulin, and gamma globulin were 5%, 3%, 5%, 4%, 5%, and 5%, respectively, which are acceptable from the point of view of measurement technology in engineering practice.

#### **4.2.3 Confocal Laser Scanning Microscopy Measurement**

Three different H<sub>2</sub>S concentration serum samples (each sample 100 µL) were prepared, called Serum sample 1, Serum sample 2, and Serum sample 3, respectively, in the following discussion. These sera were taken from 10 –12 week old male Sprague-Dawley rats (The rats were housed in an animal care facility at the College of Medicine, University of Saskatchewan, and the animal experiment protocols were approved by the Committee on the Animal Care and Supply of the University of Saskatchewan). The H<sub>2</sub>S concentrations of these three samples, measured by a sulfide sensitive electrode (Model 9616, Orion Research, Beverly) on a Fisher Accumet AR50 pH meter (Fisher Scientific, Pittsburgh, PA), were 25 µM, 44 µM, and 71 µM, respectively. Standards were prepared from Na<sub>2</sub>S stock solution, which was freshly prepared on the day of the measurement.

The control sample for this experiment was distilled water. In this experiment, for each sample, thirty different spots were measured, and each spot was measured thirty times for one minute by the time series function available with confocal laser scanning microscopy.

Laser Scanning Microscopy (Zeiss LSM 510 META) was used to measure the fluorescence intensity of the carbon nanotubes. The excitation wavelength selected in this experiment was 514 nm and emission was collected from 539 nm to 700 nm.

#### **4.2.4 Raman Microscopy Measurement**

The 50  $\mu\text{L}$  bovine hemoglobin (methemoglobin, Sigma H2500) was first mixed with 300  $\mu\text{L}$  fetal bovine serum (F1050, Sigma) to scavenge  $\text{H}_2\text{S}$ ; such a serum sample was considered “without”  $\text{H}_2\text{S}$ . Then, we equally divided this serum sample into three samples and added  $\text{H}_2\text{S}$  with different concentrations into these three samples. The concentrations of the three samples after adding  $\text{H}_2\text{S}$  were 20  $\mu\text{M}$ , 50  $\mu\text{M}$ , and 100  $\mu\text{M}$ , respectively.

The Raman microscopy (Renishaw system 2000) was used to measure the luminescence of the immersed carbon nanotubes. In the experiment, the excitation wavelength was 514 nm, and the wavelength of luminescence was selected in the range from 520 nm to 600 nm.

On a general note, the confocal laser scanning microscopy and Raman microscopy were used for the purpose to confirm the binding between carbon nanotube and H<sub>2</sub>S in sera. It is further noted that in either confocal laser scanning microscopy or Raman microscopy measurement, carbon nanotubes of 1.6 mg were immersed into each of the serum and control samples, respectively. After 2 minutes, carbon nanotubes were taken out from the samples and dried on glass slides for measurement

#### **4.2.5 Raman Microscopy Measurement of Hemoglobin Samples**

There were three bovine hemoglobin (methemoglobin, Sigma H2500) water solution samples with different concentrations, 3.7 mM, 1.8 mM, and 1.2 mM, respectively. A 100  $\mu$ L quantity of each sample was used in the experiment. Carbon nanotubes of 1.6 mg were then immersed in each of the three samples for 5 minutes. The same amount of the carbon nanotubes was also immersed in 100  $\mu$ L distilled water for 5 minutes and they were used for control. The carbon nanotubes treated in the four samples (three haemoglobin samples and one distilled water sample) were then taken out and placed on the same glass slide for Raman microscopy measurement.

Raman microscopy (Renishaw system 2000) was used in the experiment for examining both the frequency response and luminescence response of treated carbon nanotubes. In both situations, the excitation wavelength for Raman microscopy was 514 nm. The range of the wave numbers for collecting the frequency response was from



1000  $\text{cm}^{-1}$  to 4000  $\text{cm}^{-1}$ , and the range of the wavelengths for collecting the luminescence response was from 520 nm to 600 nm.

## **4.3 Results**

### **4.3.1 Serum Measurement**

The sulfide ion sensitive electrode showed that  $\text{H}_2\text{S}$  was present in the serum with the concentration of about 36  $\mu\text{M}$ . Table 4.1 shows the result of protein measurement using the Spectrophotometry and electrophoresis instruments. The first column in Table 4.1 lists the proteins in interest, the second and third columns show the amounts of portents before and after the treatment of carbon nanotubes, respectively. The results of Table 4.1 indicate that the amounts of the proteins in the two samples (control versus treated) had no difference, which further suggests that the proteins be not adsorbed by the carbon nanotubes. This conclusion needs to be taken in caution due to the measurement limitation of the instruments used (i.e., spectrophotometry and electrophoresis

Table 4.1: Protein Quantities Before and After the Serum was Treated by Carbon Nanotubes (These results are from 3 measurements and hence averaged).

<b>Proteins</b>	<b>Before CNT treatment (g/L)</b>	<b>After CNT treatment (g/L)</b>
Total protein	48	49
Albumin	16	17
Alpha1-globulin	3	3
Alpha2-globulin	8	8
Beta globulin	9	8
Gamma globulin	11	12

The fluorescence spectrum by confocal laser scanning microscopy is shown in Figure 4.1. From this figure, it can be seen that the intensity of the fluorescence for the carbon nanotubes which were treated with the serum (containing H<sub>2</sub>S) was higher than that for the carbon nanotube which was treated in distilled water. According to the conclusion obtained from the measurement of using spectrophotometry and electrophoresis analyses, the increasing intensity of the fluorescence of the treated carbon nanotubes in the serum must be caused by the H<sub>2</sub>S.

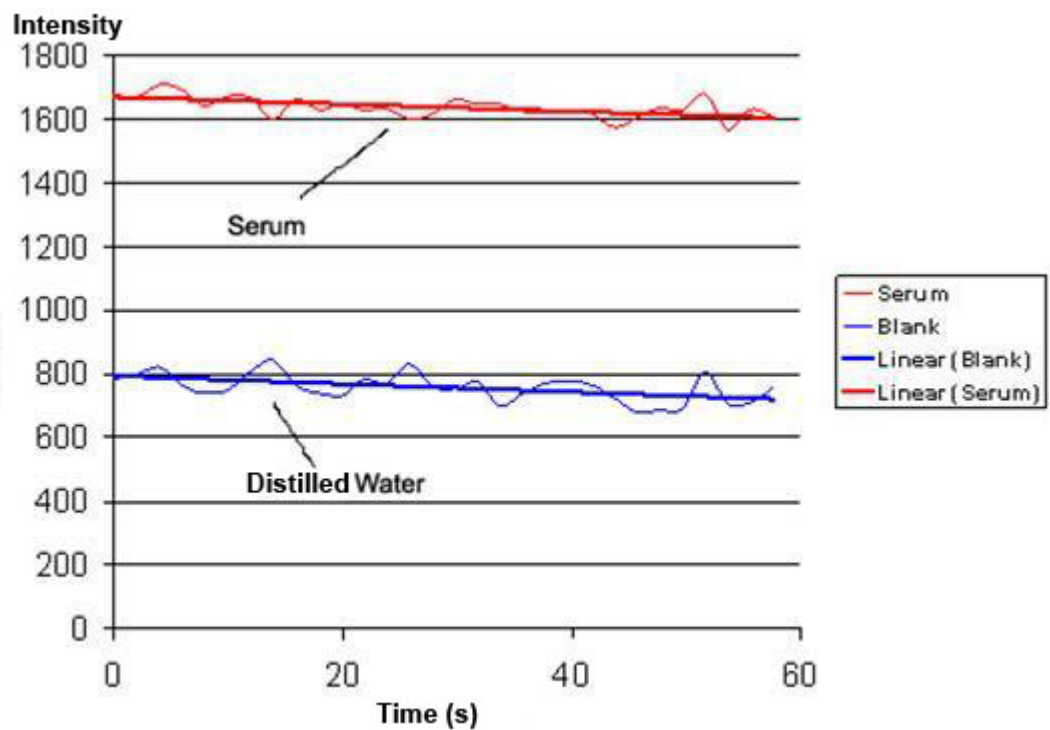


Figure 4.1: Laser scanning microscopy fluorescence response of carbon nanotubes treated with the serum and distilled water, respectively.

### 4.3.2 Confocal Laser Scanning Microscopy Measurement

The intensity of the fluorescence of treated carbon nanotubes measured by the confocal laser scanning microscopy is shown in Figure 4.2. In this figure, Serum sample 1, Serum sample 2, and Serum sample 3 contained 25  $\mu\text{M}$ , 44  $\mu\text{M}$ , and 71  $\mu\text{M}$   $\text{H}_2\text{S}$ , respectively. The variation bar for each sample point in Figure 4.2 was calculated based on the measurement of the thirty spots on each sample. For each spot, measurements were taken thirty times and were plotted on the figure. From this figure, it can be seen that as the  $\text{H}_2\text{S}$  concentration increased, the intensity of fluorescence increased as well.

This result provides one more evidences for the positive test to our hypothesis that H<sub>2</sub>S can bind with carbon nanotube in sera where some proteins are presented.

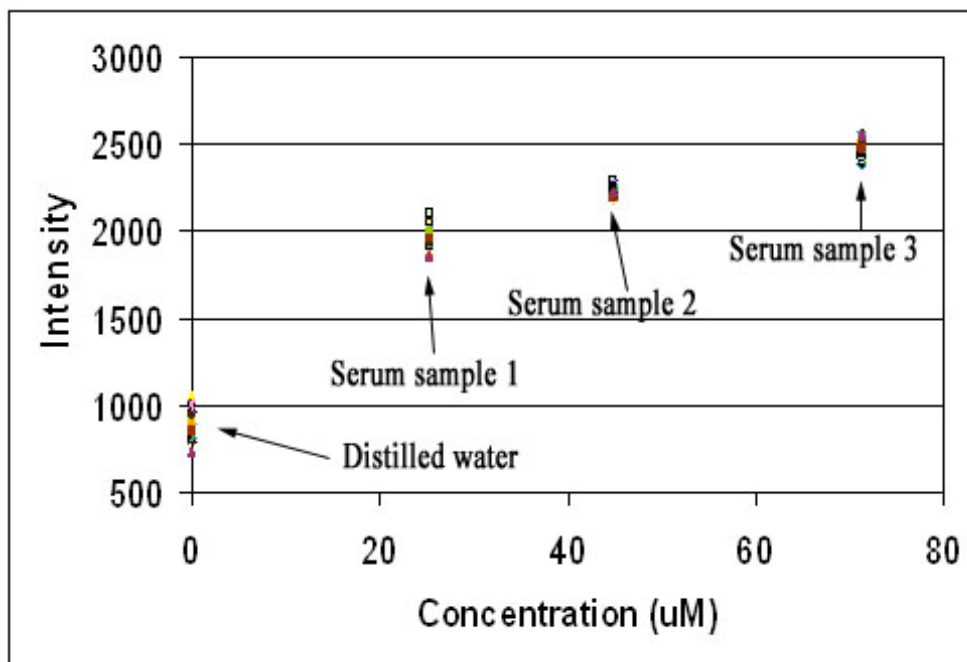


Figure 4.2: Laser scanning microscopy fluorescence intensities of the carbon nanotubes treated with the serum (with H<sub>2</sub>S concentrations of 25 µM, 44 µM, and 71 µM, respectively) and distilled water, respectively. 30 different spots were measured for each sample. Each spot was measured 30 times. In the figure, there are 30 points that correspond to each concentration (0 µM, 25 µM, 44 µM, and 71 µM, respectively). Each point was the average of 30 times' measurement.

It is noted that the intensity of fluorescence treated with distilled water was not zero, which means that carbon nanotubes can have some effect on fluorescence in confocal laser scanning microscopy. However, in all the measurements, the same type of carbon nanotube was used; as a result, this confounding effect was eliminated.

The regression and the residual analysis were further performed for three different H<sub>2</sub>S concentration serum samples. The distilled water sample was not analyzed in statistics. The regression analysis was aimed to establish a relationship between the concentrations of H<sub>2</sub>S and the fluorescence intensities. After regression analysis, the ANOVA (ANalysis Of VAriance between groups) (Table 4.2), line fit plot (Figure 4.3), Residual plot (Figure 4.4), and Normal probability plot (Figure 4.5) were produced.

Table 4.2: ANOVA for Linear Relationship between H<sub>2</sub>S Concentrations in Sera and Fluorescence Intensities.

	<b>df</b>	<b>SS</b>	<b>MS</b>	<b>F</b>	<b>Significance F</b>
Regression	1	3951934.551	3951934.551	1200.265704	4.57587 x 10 <sup>-53</sup>
Residual	88	289744.3786	3292.549757		
Total	89	4241678.93			

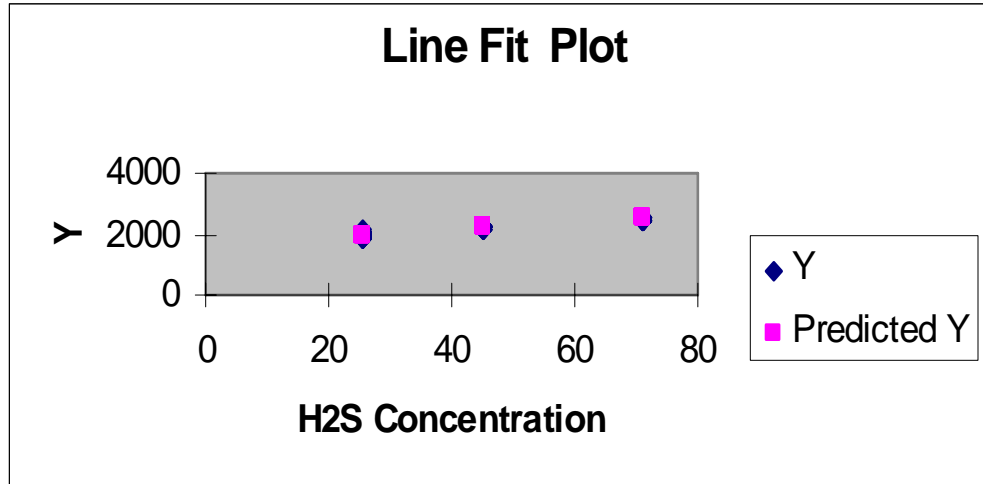


Figure 4.3: Line fit plot of H<sub>2</sub>S in sera. X-axis shows the H<sub>2</sub>S concentrations. Y-axis gives the fluorescence intensities. The small blue diamonds show the measurement for each H<sub>2</sub>S concentration. The small pink squares represent the predicted results for each H<sub>2</sub>S concentration.

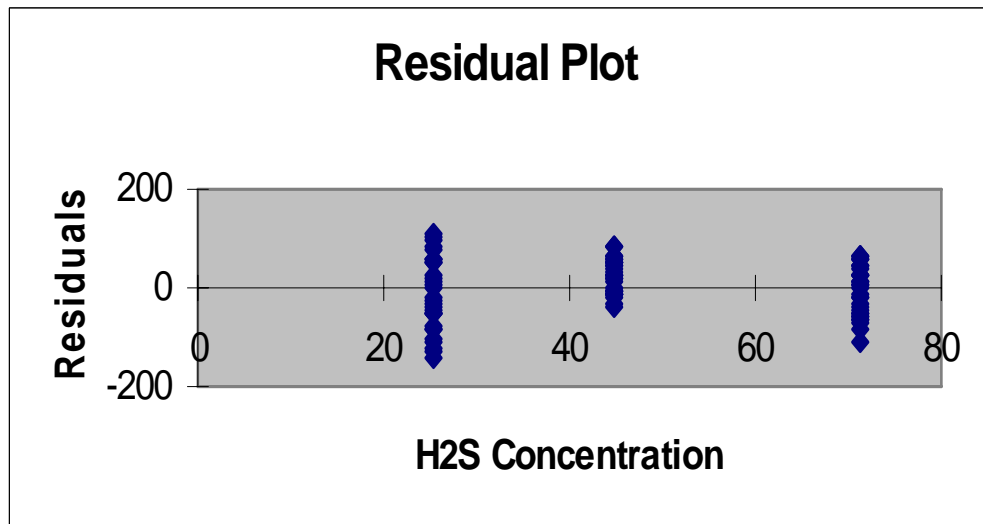


Figure 4.4: Residual plot of H<sub>2</sub>S in sera. X-axis represents the H<sub>2</sub>S concentrations. Y-axis shows the residuals. The small blue diamonds illustrate the residual value between the fluorescence intensity measured and the mean intensity for each H<sub>2</sub>S concentration.

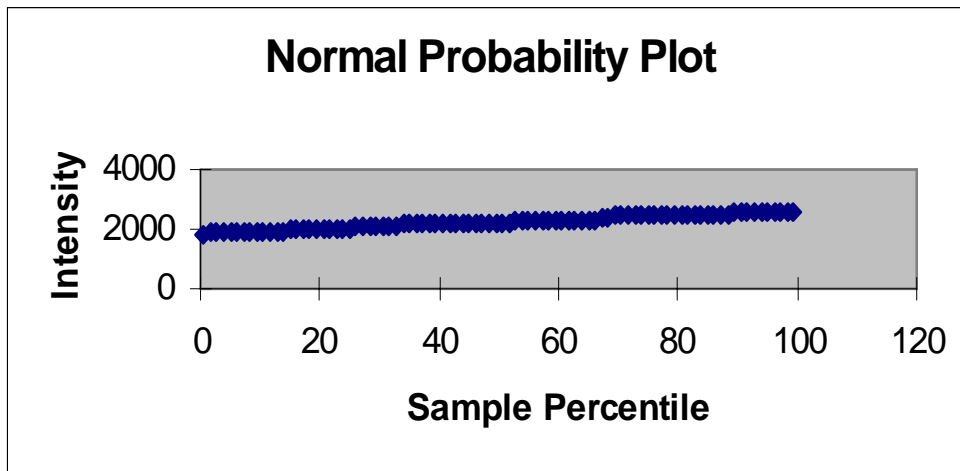


Figure 4.5: Normal probability plot of H<sub>2</sub>S in sera. It shows the distribution of the samples. This is a normal distribution as the links among small blue diamonds are almost linear.

From the line fit plot (Figure 4.3), it can be found that the relationship between fluorescence intensity and H<sub>2</sub>S concentration is linear, and it satisfies Equation 4.1 as follows:

$$y = 1707 + 11.14x \quad (4.1)$$

where  $y$  refers to fluorescence intensity, and  $x$  refers to H<sub>2</sub>S concentration.

The normal probability plot (Figure 4.5) extends the linear relationship between different H<sub>2</sub>S concentrations and corresponding intensities. The F value in Table 4.2 indicates the significant difference in intensity between different H<sub>2</sub>S concentrations:

### 4.3.3 Raman Microscopy Measurement

The different intensities of luminescence as measured by Raman microscopy are shown in Figure 4.6. From this figure, it can be seen that as the concentrations of H<sub>2</sub>S increase, the intensities of luminescence also increase. This result is consistent with the result obtained by confocal laser scanning microscopy.

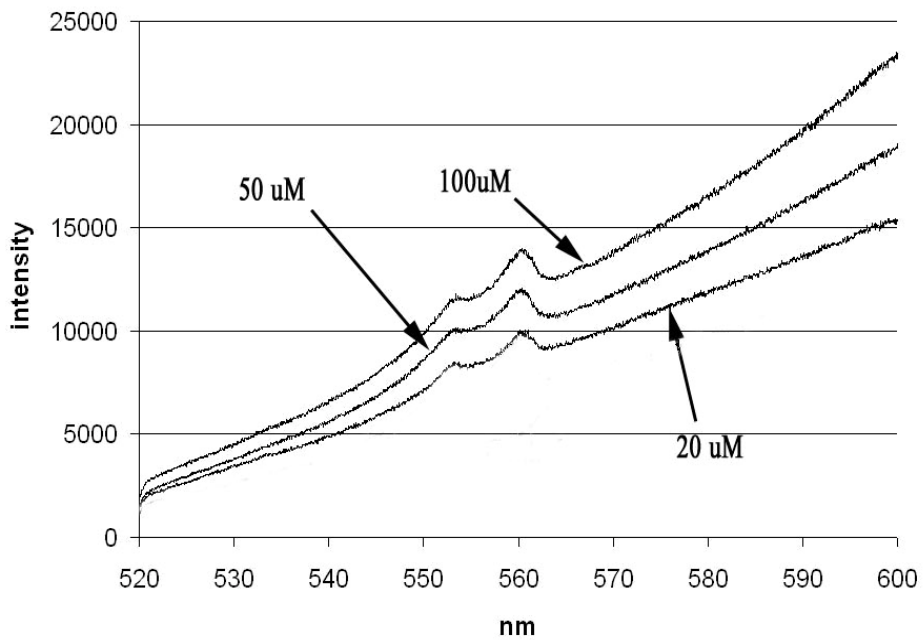


Figure 4.6: Raman luminescence response of carbon nanotubes treated with difference concentrations of H<sub>2</sub>S in sera.



#### **4.3.4 Raman Microscopy Measurement of Hemoglobin**

The results of Raman luminescence response of carbon nanotubes in distilled water and in different concentrations of hemoglobin samples are shown in Figure 4.7. This figure shows that the Raman luminescence of carbon nanotubes treated with different concentrations of hemoglobin are the same, and that these luminescence responses are also the same as those for the carbon nanotubes treated with distilled water. However, in the Raman spectrum response, by comparison to the peaks of carbon nanotube treated with distilled water, the peaks of carbon nanotubes treated with hemoglobin have a  $20\text{ cm}^{-1}$  wave number shift at about  $1500\text{ cm}^{-1}$  towards the direction of the lower wave number as shown in Figure 4.8 and Figure 4.9 which enlarges a part of Figure 4.8. However, the peak positions do not change for the samples of carbon nanotubes treated with different concentrations of hemoglobin.

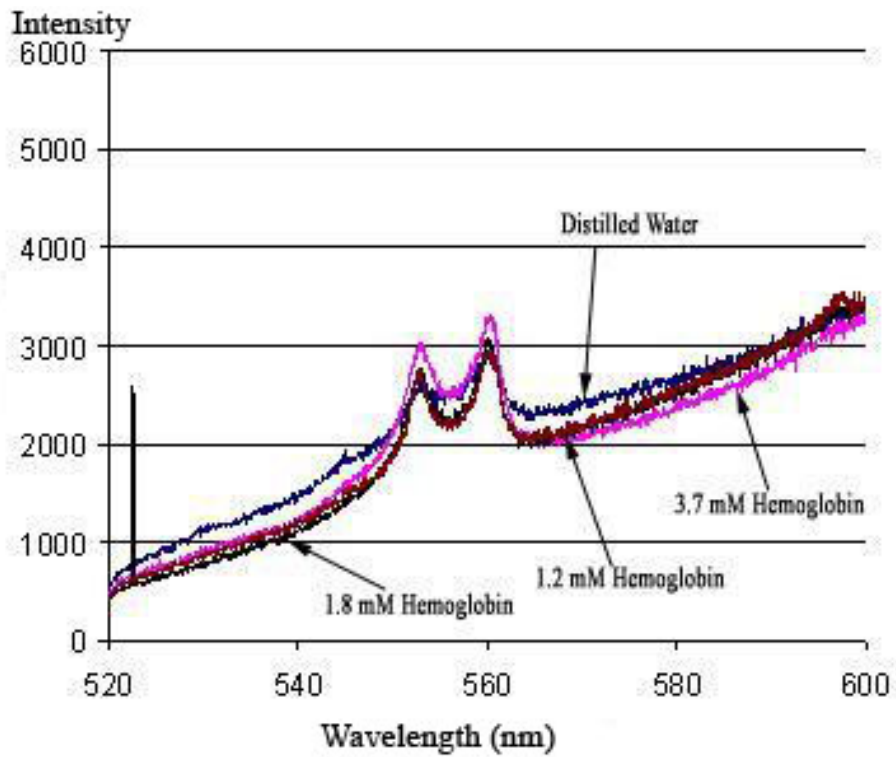


Figure 4.7: Raman luminescence responses of carbon nanotubes treated with distilled water and different concentrations of hemoglobin water solution (3.7 mM, 1.8 mM, and 1.2 mM, respectively).

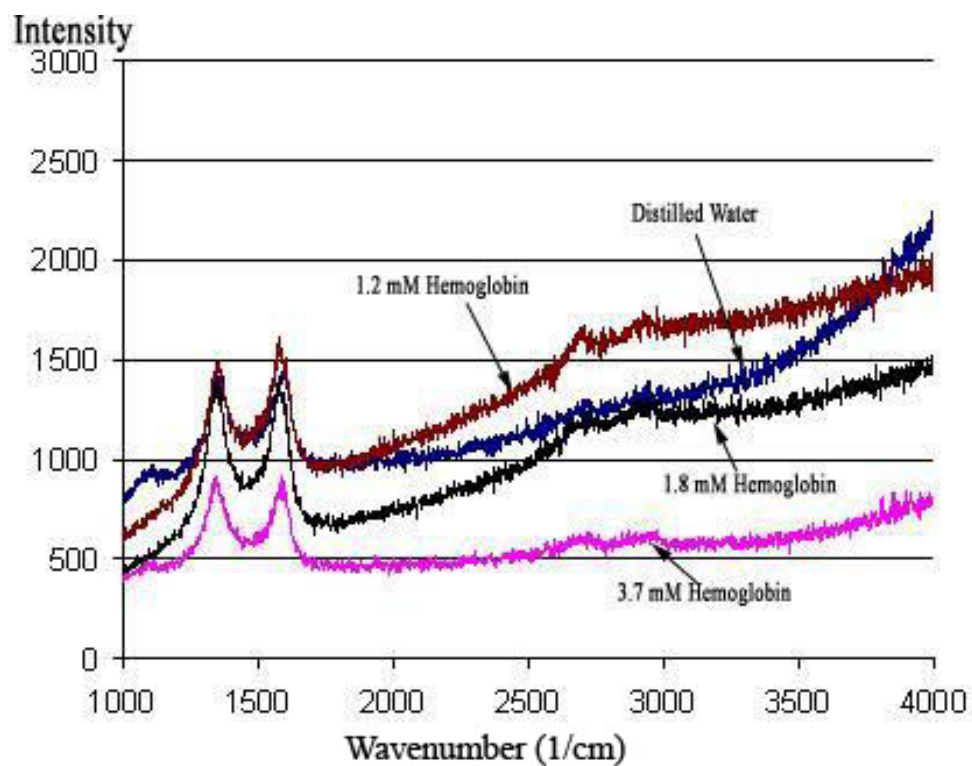


Figure 4.8: Raman spectrum responses of carbon nanotubes treated with distilled water and different concentrations of hemoglobin water solution (3.7 mM, 1.8 mM, and 1.2 mM, respectively).

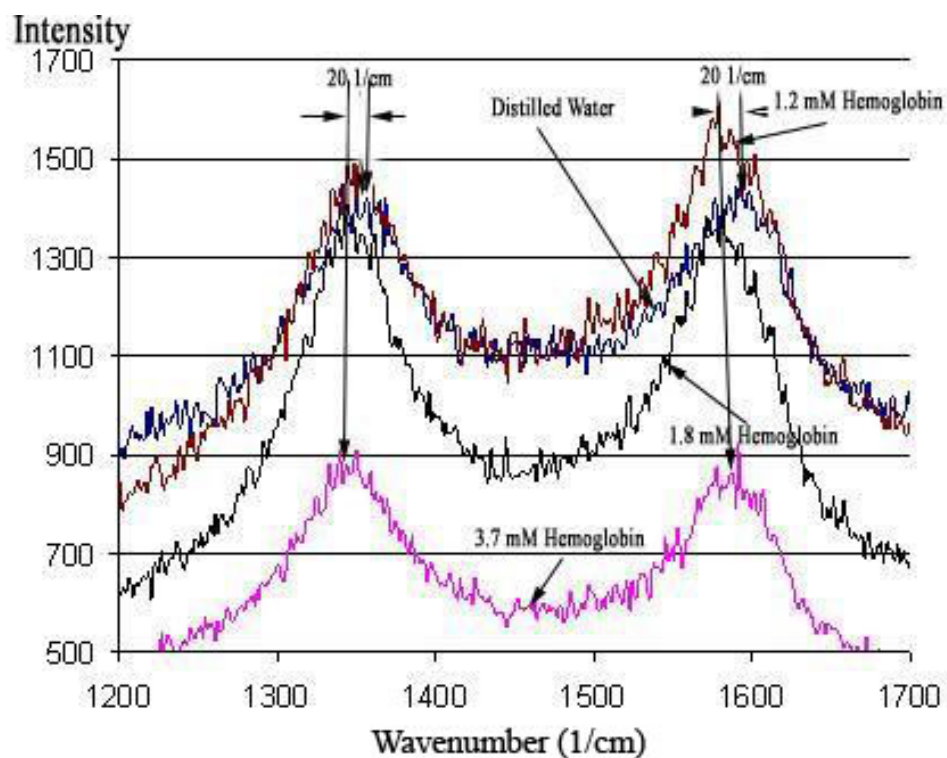


Figure 4.9: Enlarged Raman spectrum response of carbon nanotubes treated with distilled water and different concentrations of hemoglobin water solution (3.7 mM, 1.8 mM, and 1.2 mM, respectively) in the wave number range from  $1200\text{ cm}^{-1}$  to  $1700\text{ cm}^{-1}$ .

## 4.4 Discussion

### 4.4.1 The Binding of Carbon Nanotube and $\text{H}_2\text{S}$ in Sera

According to the adhesion theory presented in Section 2.7 of Chapter 2, the potential mechanism for those proteins to bind with non-functionalized carbon nanotube is the adsorption theory based on Van der Waals force. For this mechanism to work, these proteins must have an opportunity to “meet” with carbon nanotubes. However, such a meeting may not be always possible.

According to Rudee and Price [1985], when amorphous carbon interacts with the human serum, there was a continuous film (serum albumin film) created instantly in less than 1.3 seconds. The albumin film has the following dimensional properties: geometrical size: 8 nm×3.8 nm [He et al., 1992] and monomolecular radius of gyration in pH 5-7 solution: 3.2-3.4 nm [Olivieri et al., 1995]. We assume that (1) the properties of amorphous carbon which are responsible for the formation of the serum albumin film are also present in carbon nanotube (e.g., they both have the same water resistance ability which is a major facilitator for the formation of any kind of film) and (2) the properties of the human serum used in the experiment of Rudee and Price [1985] are also possessed by the serum used in our experiment. Therefore, we believe that there is a serum albumin film on the surface of the carbon nanotube in our experiment.

We further estimate that the diameter of H<sub>2</sub>S is about 1 nm, the diameter of the proteins listed in Table 4.1 are about 15-20 nm, and the diameter of the pores of the albumin film are about 4 nm. It is then clear that no proteins in the serum could penetrate the serum albumin film. Yet, H<sub>2</sub>S can penetrate the serum albumin, and as such, the process of the binding with carbon nanotube will follow the mechanism as described in Section 3.3.5. Furthermore, these proteins in sera are relatively heavier than H<sub>2</sub>S molecule; especially the average weight of these proteins is on the order of magnitude of kD, while the weight of H<sub>2</sub>S is 34 D. The light molecule has a more chance than the heavy molecule to adhere to a base element. Therefore, even though there may be some of the protein molecules in sera that may penetrate the serum

albumin film, their chance to be adsorbed by carbon nanotubes is less than H<sub>2</sub>S molecule.

#### **4.4.2 The Binding of Hemoglobin and Carbon Nanotubes in Water Solution**

Raman wave number shift for the carbon nanotube treated with different concentrations of hemoglobin (methemoglobin in our case) water solution with respect to the carbon nanotube treated with distilled water indicates that there is a change in the vibration property for these two situations. This further means that Raman spectrum response is sensitive to hemoglobin when it binds with carbon nanotube, and thus we can conclude that hemoglobin does bind with carbon nanotube. Further, this shift towards a lower wave number means that the compound containing the carbon nanotube and hemoglobin has lower frequency than the carbon nanotube.

It is noted that for the Raman luminescence of carbon nanotubes treated with the hemoglobin samples, the excitation wavelength is 514 nm and the range for collecting luminescence is from 520 nm to 600 nm, which are the same as those for Raman luminescence of carbon nanotube treated with H<sub>2</sub>S. The fact that the Raman luminescence of carbon nanotubes treated with hemoglobin does not change with respect to that with distilled water is good news to the selectivity of carbon nanotube to H<sub>2</sub>S with the Raman luminescence response as a tool to measure H<sub>2</sub>S on carbon nanotube.

## 4.5 Related Work

The study on the binding between H<sub>2</sub>S and carbon nanotube in sera was first described in this dissertation or our paper [Wu et al., 2007]. The experimental observation of this binding in sera using Raman and confocal laser scanning microscopes was first made in this dissertation or our paper [Wu et al., 2007]. Though there have been many studies on the binding of H<sub>2</sub>S and activated carbon, they were not in the serum. Naturally, the mechanism underlying the binding between H<sub>2</sub>S and carbon nanotube in sera was first proposed in this dissertation. In the literature, there is a study on the binding behaviour between the human serum and amorphous carbon [Rudee and Price, 1985]; the study has not explicitly considered H<sub>2</sub>S or the study was not directed to the understating of the binding between H<sub>2</sub>S and carbon nanotube. However, this study was learned and adapted to lead to the proposed mechanism which governs the process of the binding of H<sub>2</sub>S and carbon nanotube in sera – in particular the phenomenon that the proteins in sera will not bind with carbon nanotube.

Further, the studies, such as Klein et al., [1984 and Pilarczyk et al., [1987], on the chemical reason between H<sub>2</sub>S and oxygen in the presence of activated carbon were learned to lead to the mechanism for the binding between H<sub>2</sub>S and carbon nanotube – in particular the process after H<sub>2</sub>S penetrates the serum albumin film and arrives at the surface of carbon nanotube which contains oxygen molecules.

It appears imperative to understand whether proteins bind with non-functionalized carbon nanotube for this dissertation study. Recently, interests in biological applications of carbon nanotubes are growing. It is reported that various proteins (small peptides [Pantarotto et al., 2004], the protein streptavidin [Kam et al., 2005], and nucleic acids [Lu et al., 2004; Bianco et al., 2005]) can be adsorbed spontaneously on the side walls of acid-oxidized single-walled carbon nanotubes (SWNTs). Kam et al. [2005] further indicated that single-walled carbon nanotubes are generic intracellular transporters for various types of proteins with weight less than 80 kD, and they can be covalently or non-covalently bound to the nanotube sidewalls in a standard phosphate buffer saline (PBS). However, Salvador-Morales et al. [2006] reported that protein binding to functionalized carbon nanotubes is highly selective. They experimented with many different proteins in plasma and found that very few of them can bind to the carbon nanotubes. Fibrinogen was the proteins that bind to carbon nanotubes in the greatest quantity [Salvador-Morales et al., 2006]. On a general note, all these studies on the binding between proteins and carbon nanotube seem to be rooted in the so-called functionalized carbon nanotube; the functionalization of carbon nanotube means to have a chemical treatment on the surface of carbon nanotube.

#### **4.6 Conclusion**

(1) The low concentration and nano quantity  $H_2S$  in serum can be measured using carbon nanotubes with the fluorescence response by LSM 510 META laser scanning microscopy and the luminescence response by Raman microscopy. In confocal laser



scanning microscopy, statistic analysis shows a linear relationship between fluorescence intensity and H<sub>2</sub>S concentration.

- (2) The measurement resolution for H<sub>2</sub>S concentration in sera is about 20 μM; however, this is not a low limit that can be measured. In our previous experiment described in Chapter 3, we measured 10 μM H<sub>2</sub>S in water solution by confocal laser scanning microscopy. Because proteins in serum will not affect the measurement, according to the present study, it should be very likely that we can reach the resolution of 10 μM H<sub>2</sub>S in sera. On the other hand, the resolution of the H<sub>2</sub>S concentration measurement is certainly not limited by the carbon nanotubes, but rather by the way the confocal laser scanning microscopy or Raman microscopy is employed to examine the change in fluorescence or luminescence. Using a highly sensitive method for response data acquisition, it is highly feasible to achieve the measurement of H<sub>2</sub>S in the serum in high resolution.
- (3) Hemoglobin can bind with multi-wall carbon nanotubes, but this binding will not affect the luminescence of the carbon nanotubes under specific excitation and emission wavelengths. This further suggests that the selectivity of a bio-sensor be also related to the means used for acquiring response information of a particular substance (H<sub>2</sub>S in our case).

## CHAPTER 5

### TRACKING OF A SINGLE NANO-PARTICLE

#### 5.1 Introduction

From Chapter 3, it can be seen that low concentration and nano quantity of H<sub>2</sub>S in water solution can be detected using carbon nanotubes with the fluorescence spectrum by ZEISS LSM 510 Meta laser scanning microscopy [Wu et al., 2006]. Chapter 4 further shows that by using the same method, H<sub>2</sub>S in serum can be detected [Wu et al., 2007]. These results have made it possible to develop a clinical approach using confocal laser scanning microscopy, though our initial purpose of using laser scanning microscopy was to use it to confirm the binding of H<sub>2</sub>S to carbon nanotube. Although this new approach requires the use of laser scanning microscopy which is relatively expensive, compared with those existing approaches as reviewed in Chapter 1, the new approach requires only a very small amount of blood tissue (i.e., several  $\mu$ L). In addition, the new approach could be used for a real-time continuous measurement of H<sub>2</sub>S in live cells, which is a useful research vehicle for understanding some *in-vivo* cellular behavior in a real time manner.

One of the essential issues to be addressed with this new approach is that laser scanning microscopy should be able to track a small (nano) particle (less than a laser point which is, typically, 5  $\mu\text{m}$  in diameter) in a live cell which is a kind of fluid environment. Laser scanning microscopy will need a period of time to have its beam on the particle to acquire information about the intensity of the fluorescence signal of the particle. The particle will undergo Brownian motion (see Section 2.8) and may thus move out of the laser point. For example, using a typical 5  $\mu\text{m}$  diameter confocal laser point, there is a 90% chance that the nano particle, originally at the centre of the laser point, will move out of the laser point in 0.3 seconds (in a fluid with the diffusion coefficient of 5  $\mu\text{m}^2/\text{s}$ ). In order to track the movement of the nano particle in fluids, there is a need to develop a control system to keep the nano particle always within the laser point scope.

In this chapter, a novel control system for tracking a nano-particle in fluid under confocal laser scanning microscopy is presented. In particular, Section 5.2 presents a conceptual design of the controller. Section 5.3 is a logical design of the controller. Section 5.4 describes the controller, which can be realized on an existing confocal laser scanning microscopy. Section 5.5 presents a simulation study for validation of the control system. Section 5.6 presents related work. Section 5.7 is a conclusion.

## 5.2 Conceptual Design of the Controller

Figure 5.1 gives the general configuration of the particle, laser scanning microscopy, and fluid. The laser point can be considered to be a cylindrical volume with its trajectory in the X-Y plane being a circle (Figure 5.1). The particle can move in three dimensions (the two-dimensional motion is within the X-Y plane and the third dimension motion is along the beam direction of the laser or Z-direction) in the fluid and can emit the fluorescence signal only when it is within the laser cylindrical volume and is excited by the beam of the laser. Further, the intensity of the fluorescence signal of the particle will be stronger if the particle is at the centre of this volume. Ideally, we should maintain the particle at the centre of this cylindrical volume of laser point during the sampling period, which is therefore the purpose of the control system. In the following discussion, we may regard this cylinder as a sphere with its diameter being the radius of the cycle in the X-Y plane.

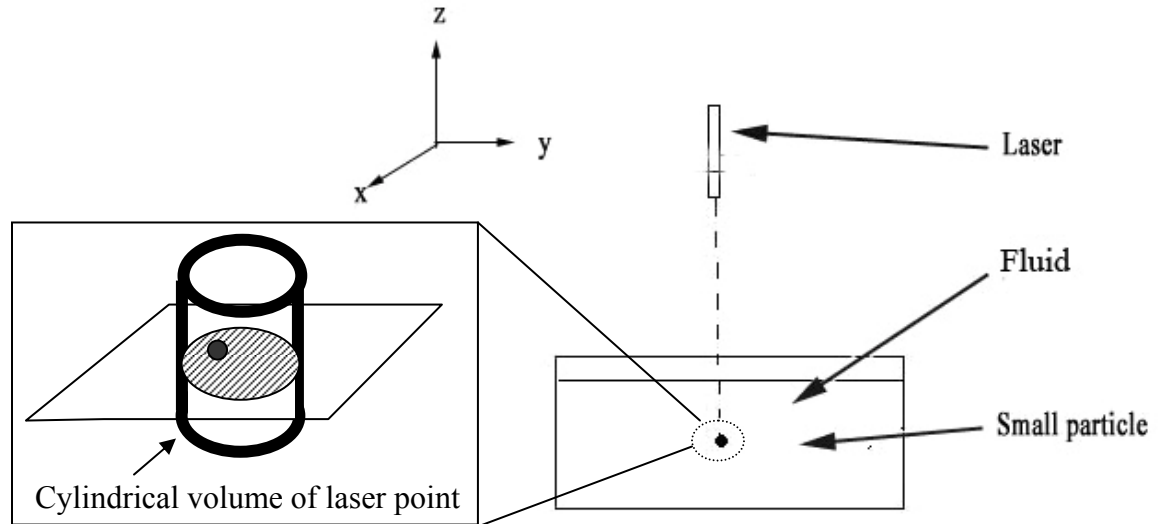


Figure 5.1: The relation among laser, fluid, and particle.

According to the discussion in Section 2.8 of Chapter 2, the control system comprises the following major components: (1) controller, (2) sensor, (3) actuator, and (4) target object to be tracked. Specifically, the controller is, in our cases, such that its input is the position of the particle and its output is the updated position of the laser. The sensor is to obtain the position of the particle at time  $t$ . The actuator is a motorized system that either moves the laser or the stage upon which the targeted object stays or the both to achieve the goal of the control system – i.e., the nano particle staying within the cylindrical volume of the laser point.

Conventional approaches to the control system are largely based on an external video camera to obtain the position of the targeted object (the nano particle in our case),

and then a discrepancy between the current position of the laser and the sensed position of the targeted object is used to derive the updated position of the laser based on a particular control law or algorithm – for example proportional-integral-derivative control law (see Section 2.8 of Chapter 2). Different from the conventional approaches, we proposed an approach to integrate the sensor and controller in such a way that while the position of the particle is being sensed the updated position of the laser is determined as well. This approach is outlined as follows.

First, the intensity of the fluorescence signal from the particle is acquired. This intensity depends on the distance between the particle and the centre of the laser point. More specifically, in Figure 5.2,  $d$  is the radius of the circle due to Brownian motion (see Section 2.8); point  $O$  is the original position of both particle and laser, and  $O'$  is the updated position for the laser or for the position of the particle with the strongest intensity of fluorescence signal.

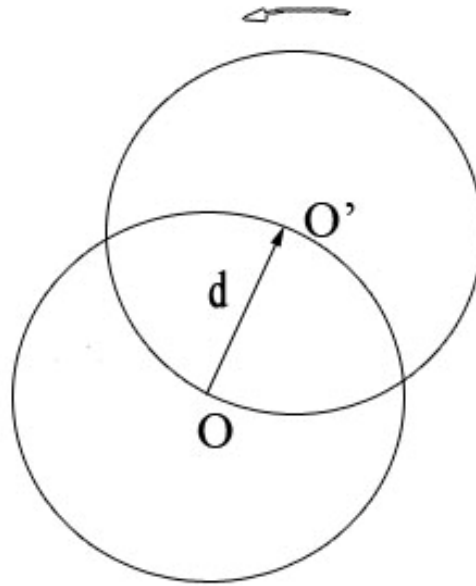


Figure 5.2: Obtaining the strongest intensity of the particle (O is the current centre of the laser point; d is the particle movement due to Brownian motion which can be calculated by knowing the signal intensity; O' is the next centre of the laser point).

Second, this intensity is converted or translated to the position of the particle, which can be achieved by adjusting the laser point in the X-Y plane (e.g., moving O' around O along the circle as shown in Figure 5.2) and then adjusting the laser point up and down in the Z-axis direction to obtain the strongest intensity. It is noted that with the pinhole in confocal laser scanning microscopy, there will be one position in the Z-axis direction that will most excite the sample or that will, in other words, give the strongest intensity.

Finally, the period of time for adjusting the laser to the position of the particle is called adjusting period. The laser working period refers to the sum of the sampling period and the adjusting period. During the adjusting period, it is assumed that the particle does not move out of the laser sphere. This assumption is made true by properly controlling the adjusting period. It is also assumed that the movement of the particle is slower than the movement of the laser or the stage.

### 5.3 Logical Design of the Controller

The objective of the logical design of the control system is to develop mathematical equations that represent the conceptual design. The most important task of this control system is to determine the position of the particle based on the intensity of that particle's fluorescence signal. Let the diameter of the laser point be  $w$ . The relationship between this intensity and the position of the particle can be expressed as [Berglund, 2007; Cang et al., 2006]:

$$I'(t) = I_0 e^{-\left(\frac{2}{w^2}\right) \mathbf{d}^2(t) \left(1 + \left(\frac{z(t)}{z_B}\right)^2\right)} + I_B \quad (5.1)$$

where,  $I_0$  is the photon count rate when the particle is in the centre of the laser sphere,  $I_B$  is the background photon count rate and can be removed through calibration in the experiment,  $z_B$  is the Rayleigh range ( $z_B = \pi w^2 / \lambda$ , where  $\lambda$  is excitation wavelength),  $\mathbf{d}$  is the distance between the position of the particle in the X-Y plane and the centre of the laser point (see also Figure 5.2), and  $z$  is the distance between the position of the particle



and the centre of the laser point along the Z-axis direction. Further, in Equation 5.1, the term  $d^2 = x_p^2 + y_p^2$  where  $x_p$  and  $y_p$  are the coordinates of point O' in the coordinate system that takes O as the origin and is in parallel with the coordinate system O-XY (see also Figure 5.2).

At time  $t=0$ , the particle and the laser point are coincident at O (see Figure 5.3). At time  $t$ , the particle moves to O'. Our goal now is to determine the coordinates of O' based on the information of the intensity of the fluorescence signal of the particle. According to Figure 5.3, we have:

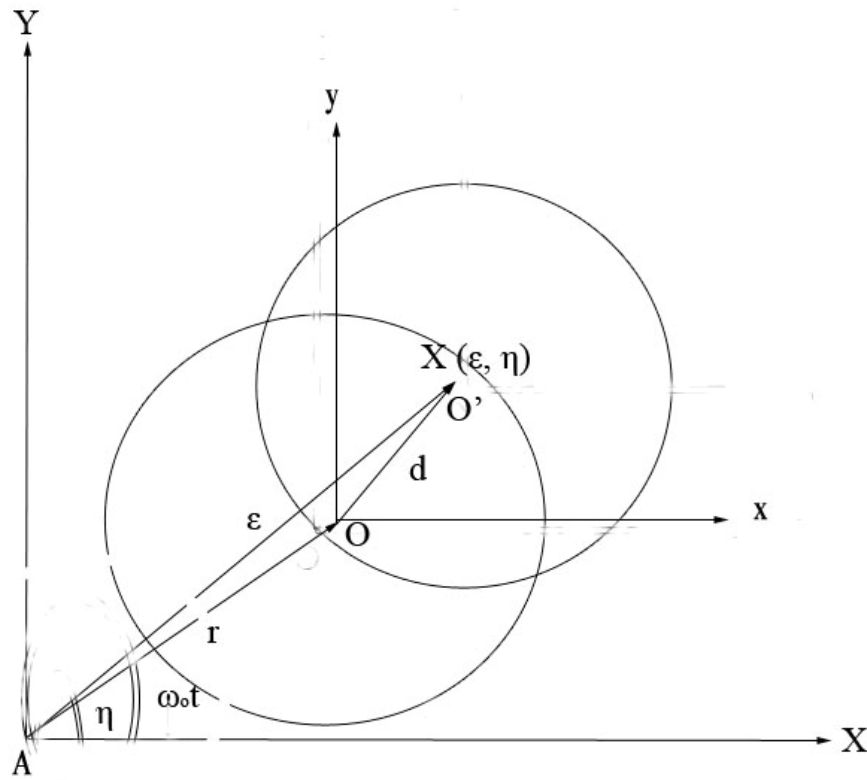


Figure 5.3: Laser tracking of the particle in the X-Y coordinate plane.

$$\mathbf{d} = \boldsymbol{\varepsilon} - \mathbf{r} \quad (5.2)$$

or

$$\mathbf{x}_p = \boldsymbol{\varepsilon} \cos(\eta) - \mathbf{r} \cos(\boldsymbol{\omega}_0 t) \quad (5.3)$$

$$\mathbf{y}_p = \boldsymbol{\varepsilon} \sin(\eta) - \mathbf{r} \sin(\boldsymbol{\omega}_0 t) \quad (5.4)$$

Then:

$$\begin{aligned} \mathbf{d}^2 &= \mathbf{x}_p^2 + \mathbf{y}_p^2 = (\boldsymbol{\varepsilon} \cos(\eta) - \mathbf{r} \cos(\boldsymbol{\omega}_0 t))^2 + (\boldsymbol{\varepsilon} \sin(\eta) - \mathbf{r} \sin(\boldsymbol{\omega}_0 t))^2 \\ &= \boldsymbol{\varepsilon}^2 (\cos^2(\eta) + \sin^2(\eta)) + \mathbf{r}^2 (\cos^2(\boldsymbol{\omega}_0 t) + \sin^2(\boldsymbol{\omega}_0 t)) \\ &\quad - 2\mathbf{r}\boldsymbol{\varepsilon} (\cos(\eta)\cos(\boldsymbol{\omega}_0 t) + \sin(\eta)\sin(\boldsymbol{\omega}_0 t)) \\ &= (\boldsymbol{\varepsilon}^2 + \mathbf{r}^2) - 2\mathbf{r}\boldsymbol{\varepsilon} \cos(\eta - \boldsymbol{\omega}_0 t) \end{aligned} \quad (5.5)$$

Substituting Equation 5.5 to Equation 5.1 (noticing that  $I_B$  is removed) leads to:

$$\begin{aligned} I(t) &= I_0 e^{-\left(\frac{2}{w^2}\right) \left[ (\boldsymbol{\varepsilon}^2 + \mathbf{r}^2) - 2\mathbf{r}\boldsymbol{\varepsilon} \cos(\eta - \boldsymbol{\omega}_0 t) \right]} \\ &= I_0 e^{-\left(\frac{2}{w^2}\right) (\boldsymbol{\varepsilon}^2 + \mathbf{r}^2)} e^{\left(\frac{4\mathbf{r}\boldsymbol{\varepsilon}}{w^2}\right) \cos(\eta - \boldsymbol{\omega}_0 t)} \end{aligned} \quad (5.6)$$

This intensity follows a Gaussian distribution. Now considering the particle position by  $\mathbf{x}_p(\boldsymbol{\varepsilon}, \eta)$  and  $\mathbf{y}_p(\boldsymbol{\varepsilon}, \eta)$  (refer to coordinate with centre O), we apply the maximum likelihood estimator [Poor, 1994; Berglund, 2007] (APPENDIX A) to obtain:

$$\begin{aligned}\hat{\mathbf{x}}_p &= \frac{\int_0^{\frac{2\pi}{w^2}} I(\tau) \cos(\omega_0 \tau) d\tau}{\int_0^{\frac{2\pi}{w^2}} I(\tau) d\tau} \\ &= 2\pi I_0 e^{-\left(\frac{2}{w^2}\right)(\boldsymbol{\varepsilon}^2 + r^2)} I_1\left(\frac{4r\boldsymbol{\varepsilon}}{w^2}\right) \cos(\eta)\end{aligned}\quad (5.7)$$

$$\begin{aligned}\hat{\mathbf{y}}_p &= \frac{\int_0^{\frac{2\pi}{w^2}} I(\tau) \sin(\omega_0 \tau) d\tau}{\int_0^{\frac{2\pi}{w^2}} I(\tau) d\tau} \\ &= 2\pi I_0 e^{-\left(\frac{2}{w^2}\right)(\boldsymbol{\varepsilon}^2 + r^2)} I_1\left(\frac{4r\boldsymbol{\varepsilon}}{w^2}\right) \sin(\eta)\end{aligned}\quad (5.8)$$

where  $I_1$  is a first order modified Bessel function. We also apply the maximum likelihood estimator for  $z$  to obtain:

$$\hat{\mathbf{z}}_p = \frac{\int_0^t I(\tau) e^{2\left(\frac{d(\tau)z(\tau)}{wz_B}\right)^2} d\tau}{\int_0^t I(\tau) d\tau} \quad (5.9)$$

In the following, we need to find the position of the particle, in particular  $\boldsymbol{\varepsilon}$ ,  $\boldsymbol{\eta}$ , and  $\mathbf{z}$ . We consider the dynamic steady-state equation that describes  $\boldsymbol{\varepsilon}$ ,  $\boldsymbol{\eta}$ , and  $\mathbf{z}$  as follows [Khali, 1996]:

$$\dot{\boldsymbol{\varepsilon}} = -\alpha(\boldsymbol{\varepsilon}(t) - \boldsymbol{\varepsilon}_0) \quad (5.10)$$

$$\dot{\boldsymbol{\eta}} = \frac{\omega}{1 + \beta(\boldsymbol{\varepsilon}(t) - \boldsymbol{\varepsilon}_0)^2} \quad (5.11)$$

$$\dot{\mathbf{z}} = -\alpha_z(\mathbf{z}(t) - \mathbf{z}_0) \quad (5.12)$$

where  $\alpha$ ,  $\alpha_z$ ,  $\beta$ ,  $\boldsymbol{\varepsilon}_0$ , and  $\omega$  are given constants.

Equation 5.10 can also be expressed as:

$$\frac{d(\boldsymbol{\varepsilon}(t)e^{\alpha t})}{dt} = \alpha \boldsymbol{\varepsilon}_0 e^{\alpha t} \quad (5.13)$$

or

$$\boldsymbol{\varepsilon}(t)e^{\alpha t} - \boldsymbol{\varepsilon}(0) = \boldsymbol{\varepsilon}_0 e^{\alpha t} - \boldsymbol{\varepsilon}_0 \quad (5.14)$$

$$\boldsymbol{\varepsilon}(t) = (\boldsymbol{\varepsilon}(0) - \boldsymbol{\varepsilon}_0)e^{-\alpha t} + \boldsymbol{\varepsilon}_0 \quad (5.15)$$

It is noted that Equations 5.10 to 5.12 allow us to obtain the position of the particle. Suppose that  $\Delta t$  is the working period. We assume that  $\Delta t$  is the same for each working period. The time domain can then be expressed as  $t_k = k\Delta t$  ( $k=1, 2, \dots, n$ ;  $n$  is the number of the working periods), or the time series of the movement of the laser can be expressed by  $\{k\}$ . It is further noted that the tracking for time  $k$  will be based on the working period  $k-1$ . By applying Equation 5.15 to each time interval from  $k$  to  $k+1$ , we obtain:

$$\boldsymbol{\varepsilon}(k+1) = (\boldsymbol{\varepsilon}(k) - \boldsymbol{\varepsilon}_0)e^{-\alpha \Delta t} + \boldsymbol{\varepsilon}_0 \quad (5.16)$$

By integration of Equation 5.11, we can obtain:

$$\eta(t) - \eta(0) = \int_0^t \frac{\omega}{1 + \beta(\boldsymbol{\varepsilon}(\tau) - \boldsymbol{\varepsilon}_0)^2} d\tau$$

$$\begin{aligned}
&= \left( \frac{\omega}{2\alpha} \right) \ln(e^{2\alpha t} (1 + \beta(\boldsymbol{\varepsilon}(t) - \boldsymbol{\varepsilon}_0)^2)) \Big|_0^t \\
&= \left( \frac{\omega}{2\alpha} \right) \ln(e^{2\alpha t} (1 + \beta(\boldsymbol{\varepsilon}(t) - \boldsymbol{\varepsilon}_0)^2)) \\
&\quad - \left( \frac{\omega}{2\alpha} \right) \ln(1 + \beta(\boldsymbol{\varepsilon}(0) - \boldsymbol{\varepsilon}_0)^2)
\end{aligned} \tag{5.17}$$

From Equation 5.15, we have:

$$\boldsymbol{\varepsilon}(t) - \boldsymbol{\varepsilon}_0 = (\boldsymbol{\varepsilon}(0) - \boldsymbol{\varepsilon}_0) e^{-\alpha t} \tag{5.18}$$

Substituting Equation 5.18 to 5.17, we have:

$$\begin{aligned}
\eta(t) - \eta(0) &= \left( \frac{\omega}{2\alpha} \right) \ln(e^{2\alpha t} + \beta(\boldsymbol{\varepsilon}(0) - \boldsymbol{\varepsilon}_0)^2) \\
&\quad - \left( \frac{\omega}{2\alpha} \right) \ln(1 + \beta(\boldsymbol{\varepsilon}(0) - \boldsymbol{\varepsilon}_0)^2) \\
&= \left( \frac{\omega}{2\alpha} \right) \ln \frac{(e^{2\alpha t} + \beta(\boldsymbol{\varepsilon}(0) - \boldsymbol{\varepsilon}_0)^2)}{(1 + \beta(\boldsymbol{\varepsilon}(0) - \boldsymbol{\varepsilon}_0)^2)}
\end{aligned} \tag{5.19}$$

By applying Equation 5.19 to each time interval from  $k$  to  $k+1$ , we obtain:

$$\eta(k+1) = \eta(k) + \left( \frac{\omega}{2\alpha} \right) \ln \frac{(e^{2\alpha \Delta t} + \beta(\boldsymbol{\varepsilon}(k) - \boldsymbol{\varepsilon}_0)^2)}{(1 + \beta(\boldsymbol{\varepsilon}(k) - \boldsymbol{\varepsilon}_0)^2)} \tag{5.20}$$

Using the same procedure as  $\epsilon$  as for  $Z$ , we have:

$$\mathbf{z}(k+1) = (\mathbf{z}(k) - \mathbf{z}_0)e^{-\alpha_z \Delta t} + \mathbf{z}_0 \quad (5.21)$$

At time  $t$ , the position of the centre of the focus point is then:

$$\mathbf{X}(k+1) = \begin{pmatrix} \mathbf{x}(k) \\ \mathbf{y}(k) \\ \mathbf{z}(k) \end{pmatrix} + \mathbf{X}_k \quad (5.22)$$

Where:

$$\mathbf{x}(k) = \epsilon \cos(\eta) \quad (5.23)$$

$$\mathbf{y}(k) = \epsilon \sin(\eta) \quad (5.24)$$

$$\mathbf{X}_k = \begin{bmatrix} \mathcal{X}_p(k) \\ \mathcal{Y}_p(k) \\ \mathcal{Z}_p(k) \end{bmatrix} \quad (5.25)$$

Now, let us determine the maximum working period denoted by  $t_{\max}$ . The meaning of  $t_{\max}$  is such that when the particle moves for a period of time longer than  $t_{\max}$  from the centre of the laser point sphere, the particle will be out of the sphere. The  $t_{\max}$  is thus related to the radius  $(\frac{w}{2})$  of the laser point sphere. It is known from the previous

discussion (Chapter 2) that the Brownian motion of a particle in a fluid follows a Rayleigh distribution. Therefore, the probability (P) that the particle will move out of the laser point sphere can be expressed by:

$$P = \int_0^{\frac{w}{2}} \frac{q}{Dwt_{\max}} e^{-\frac{q^2}{2Dt_{\max}}} dq = 1 - e^{-\frac{w^2}{2Dt_{\max}}} \quad (5.26)$$

where D is the diffusion coefficient of the fluid and q is a distance variable for the movement of the particle.

From Equation 5.26, we can calculate the maximum working period:

$$t_{\max} = \frac{\left(\frac{w^2}{2}\right)}{2D \ln\left(\frac{1}{1-P}\right)} \quad (5.27)$$

#### 5.4 Laser Scanning Microscopy Implementation

In this section, we discuss a proposed implementation of the control system based on confocal laser scanning microscopy, where we considered that the laser can be moved in a motorized manner in the X-Y plane and the stage can be moved in a motorized manner in the Z-direction. Though it was uncertain that the commercial confocal laser scanning microscopy would actually provide such a capability, we



believed that this is feasible. In a certain sense, the proposed implementation scheme may provide useful information to the manufactures of laser scanning microscopy.

Figure 5.4 shows a design or modified design of an inverted confocal laser scanning microscopy. In this design, the 514 nm light is from argon lasers (Light Source). The filter is used to select a proper wavelength, specifically, 518 nm. Objective 1 is to focus the laser beam on the sample. The intensity of the laser beam should be adjusted for the best performance. The sample is placed on a piezoelectric translation stage. A 60x water immersion objective is placed beneath the sample. A part of the emission light, collected by the objective 1, is split by a 50/50 Beam Splitter 1 to a PMT that records the intensity of the particle fluorescence signal. Another part of the emission light meets a 50/50 Beam Splitter 2. The emission light that passes the Beam Splitter 2 can form an intensity that can be focused through Lens 3 and Lens 4, and detected by Detector 2 (an avalanche photodiode). The signal detected by Detector 2 is sent to the control system for actuating the laser movement in the XY plane. The emission light reflected by Beam Splitter 2 is collected by Objective 2. A pinhole (see Section 2.4 for the function of the pinhole) is placed slightly behind the conjugate focal point of Objective 2. Lens 2 collects all the light coming out of the pinhole and focuses it at Detector 1 (an avalanche photodiode). It is noticed that when the particle moves in and out of the focus point, the intensity detected by Detector 1 is different from that of the particle on the focus point. The intensity signal that is collected by Detector 1 is sent to the control system actuator, which in turn controls the movement of the stage along the Z-axis direction.

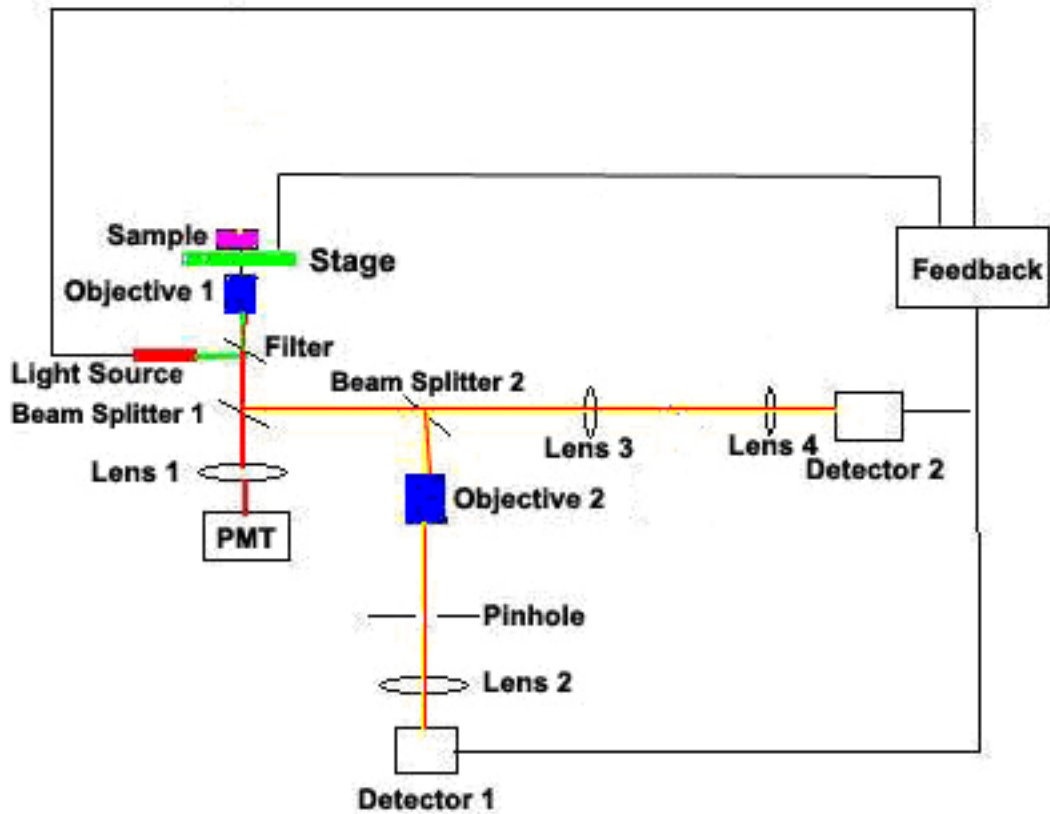


Figure 5.4: Laser scanning microscopy design for small particle tracking.

### 5.5 Evaluation of the Control System Based on Simulation

Evaluation of the proposed control system was done through simulation. In this simulation we used a common laser point diameter  $w = 5 \mu\text{m}$  and assumed that initially the laser was at an original position such that  $z_0 = 0$ ,  $\eta = 0$ , and  $\epsilon_0 = 0$ ;  $\omega$ ,  $\alpha$ ,  $\alpha_z$ , and  $\beta$  can be adjusted such that a suitable control system can be designed. In our simulation,  $\omega = \alpha = \alpha_z = 500$ , and  $\beta = 0.2$ . The diffusion coefficient of the fluid is  $5 \mu\text{m}^2/\text{s}$ . For this

diffusion coefficient, the maximum working period was found by Equation 5.27 to be about 0.3 s. In our simulation, the working period was assumed to be 0.2 s.

It is difficult to simulate the process of obtaining the position based on the intensity of the fluorescence signal of the particle. Therefore, the model of the Brownian motion was used to get the position of the particle in the simulation study. In order to get the position of the particle which is under the Brownian motion, Equation 2.11 in Chapter 2 can be applied. However, there were two reasons for not taking this equation. First, in the model of the Brownian motion, there is a need to know the forces acting on the particle, which is very difficult for our case. Second, in the tracking process, the tracking action at time  $k$  is based on the position of the particle at time  $k-1$ ; while in Equation 2.11, the reference coordinate system is associated with the time  $t=0$  (i.e., initial position). In order to make Equation 2.11 applicable to the tracking process, it needs to be revised.

For the above two reasons, eventually, a set of random functions provided in MATLAB was used for predicting the position of the particle. These functions were considered to be close to the Brownian motion, and they are given as follows [MATLAB Program]:

$$x(k+1) = x(k) + t\sigma\xi \quad (5.28)$$

$$y(k+1) = y(k) + t\sigma\xi \quad (5.29)$$

$$z(k+1) = z(k) + t\sigma\xi \quad (5.30)$$

where  $t$  is the working period;  $\sigma$  is a given constant;  $x(k)$ ,  $y(k)$ , and  $z(k)$  are the positions of the particle in the X, Y, and Z directions, respectively.

Figures 5.5–5.7 show the simulated positions of both the laser point and the particle. Figure 5.8 shows the error of the tracking in the XY coordinate plane. In particular, the error is calculated by the following equation:

$$E_{XY}(k) = |E_x(k)X(k)| + |E_y(k)Y(k)| \quad (5.31)$$

where:

$$E_x(k) = |X(k) - x(k)| \quad (5.32)$$

$$E_y(k) = |Y(k) - y(k)| \quad (5.33)$$

$X(k)$  and  $Y(k)$  are the positions of the laser point and the particle in the X and Y directions, respectively.  $x(k)$  and  $y(k)$  are the positions of the particle in the X and Y directions at working period  $k$ , respectively

Figure 5.9 shows the error of the tracking in the Z direction, which is calculated by the following equation:

$$E_z(k) = |Z(k) - z(k)| \quad (5.34)$$

where  $Z(k)$  and  $z(k)$  are the positions of the laser point and particle in the Z direction at working period  $k$ , respectively.

From Figures 5.8–5.9, the maximum position error is less than 200 nm for either the laser in XY plane or the stage in Z direction. In the worst scenario, if the position of the particle is 200 nm away the centre of the laser point in both the XY plane and Z directions, about 99% of the particle's can still be collected by using Equation 5.1 with a 514 nm excitation wavelength. Figure 5.10 shows the velocity of the laser movement in the XY plane, which is calculated by the following equation:

$$v_{XY}(k) = \sqrt{v_x^2(k) + v_y^2(k)} \quad (5.35)$$

where:

$$v_x(k) = \frac{|X(k) - X(k-1)|}{t} \quad (5.36)$$

$$v_Y(k) = \frac{|Y(k) - Y(k-1)|}{t} \quad (5.37)$$

In Equations 5.31 and 5.32,  $t$  is the working period and  $X(k)$  and  $Y(k)$  are the positions of the laser point in the  $X$  and  $Y$  directions at working period  $k$ , respectively.

Figure 5.11 shows the velocity of the stage movement in the  $Z$  direction which is calculated by the following equation:

$$v_Z(k) = \frac{|Z(k) - Z(k-1)|}{t} \quad (5.38)$$

Figures 5.10 and 5.11 show the velocities in the  $XY$  plane and  $Z$  direction that are needed to track the particle at each working period. Both velocities are less than 100  $\mu\text{m/s}$ , which are easily attainable by micro motors.

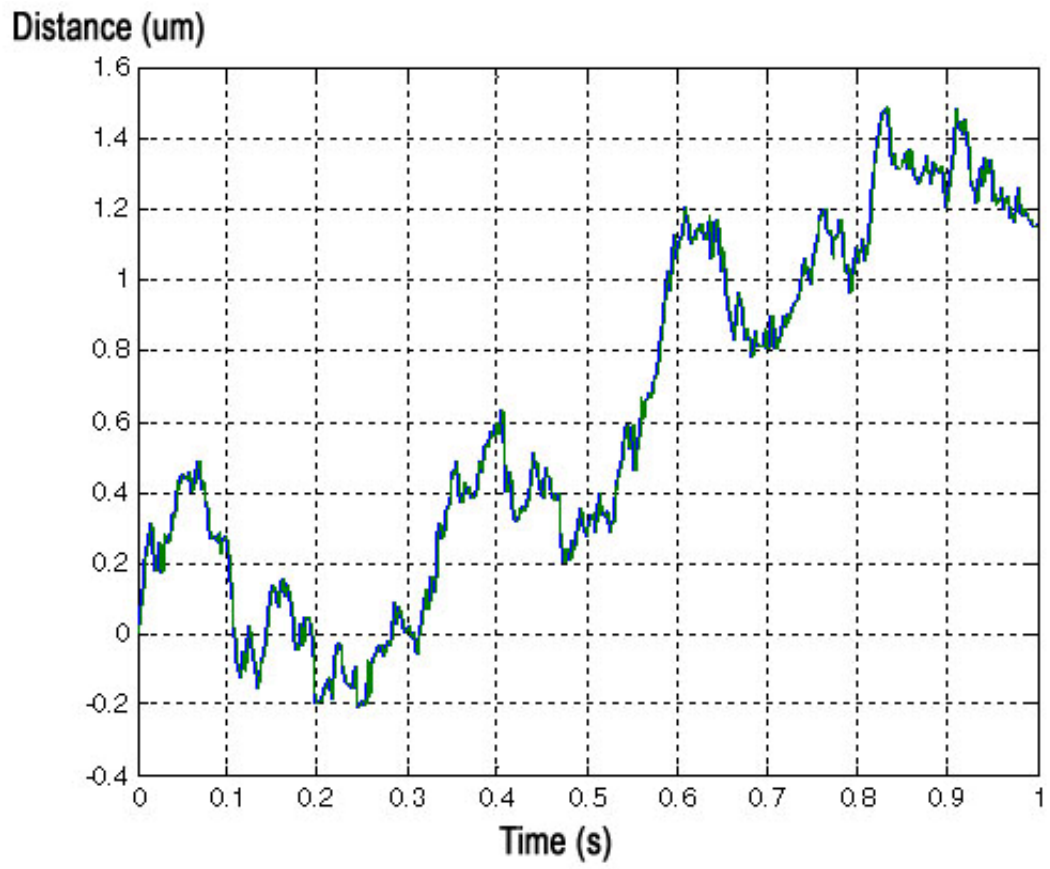


Figure 5.5: X-coordinate of the positions of the laser point and the particle (green curve: laser position; blue curve: particle position).

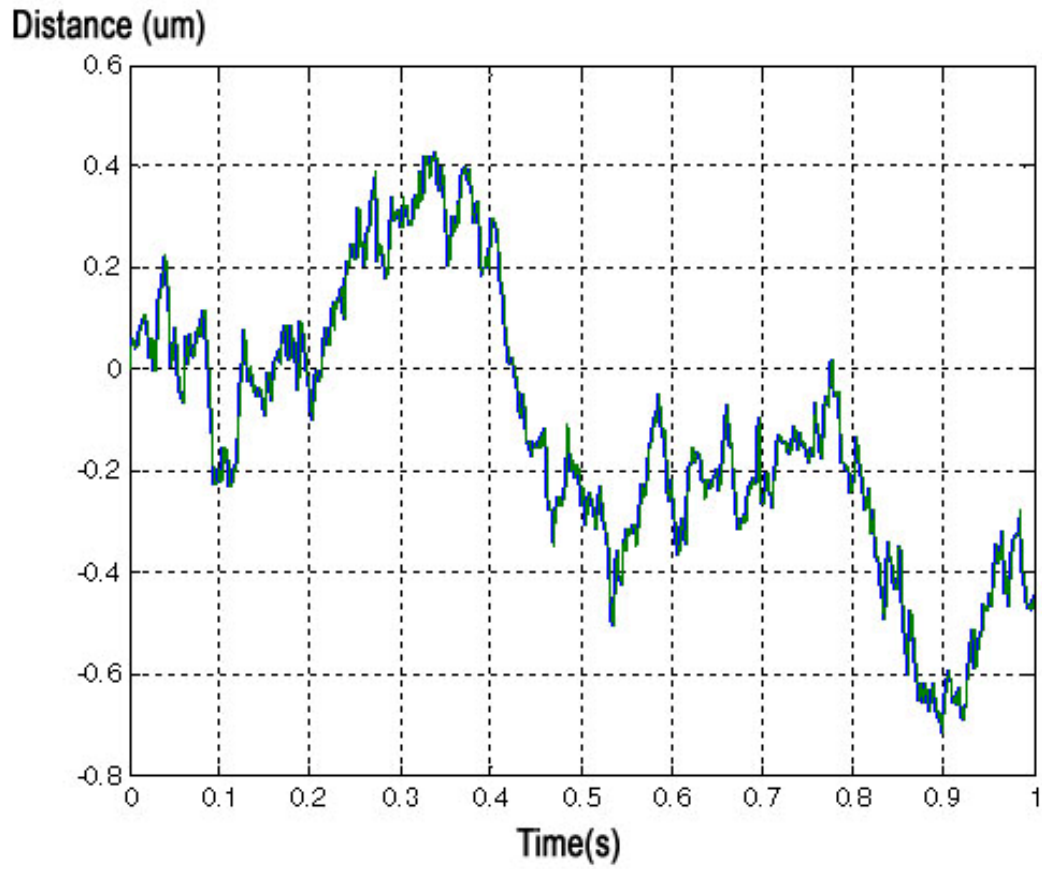


Figure 5.6: Y-coordinate of the positions of the laser point and the particle (green curve: laser position; blue curve: particle position).



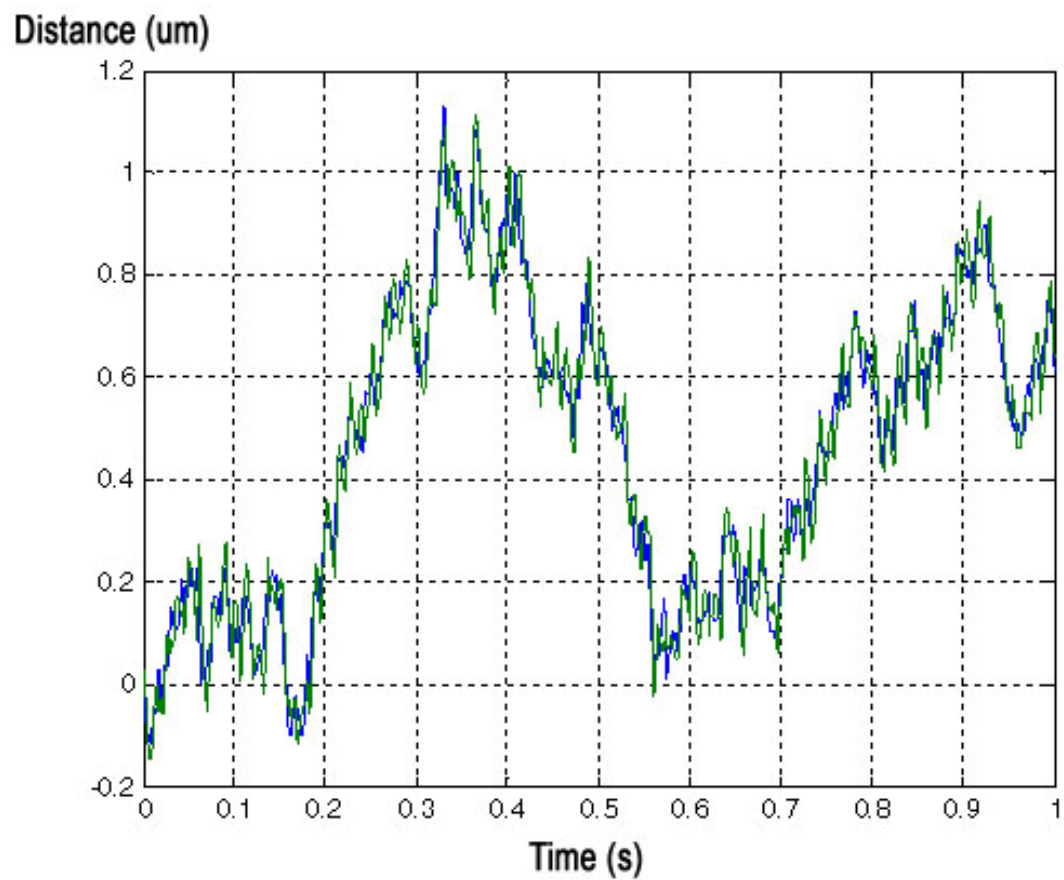


Figure 5.7: Z-coordinate of the positions of the laser point and the particle (green curve: laser position; blue curve: particle position).

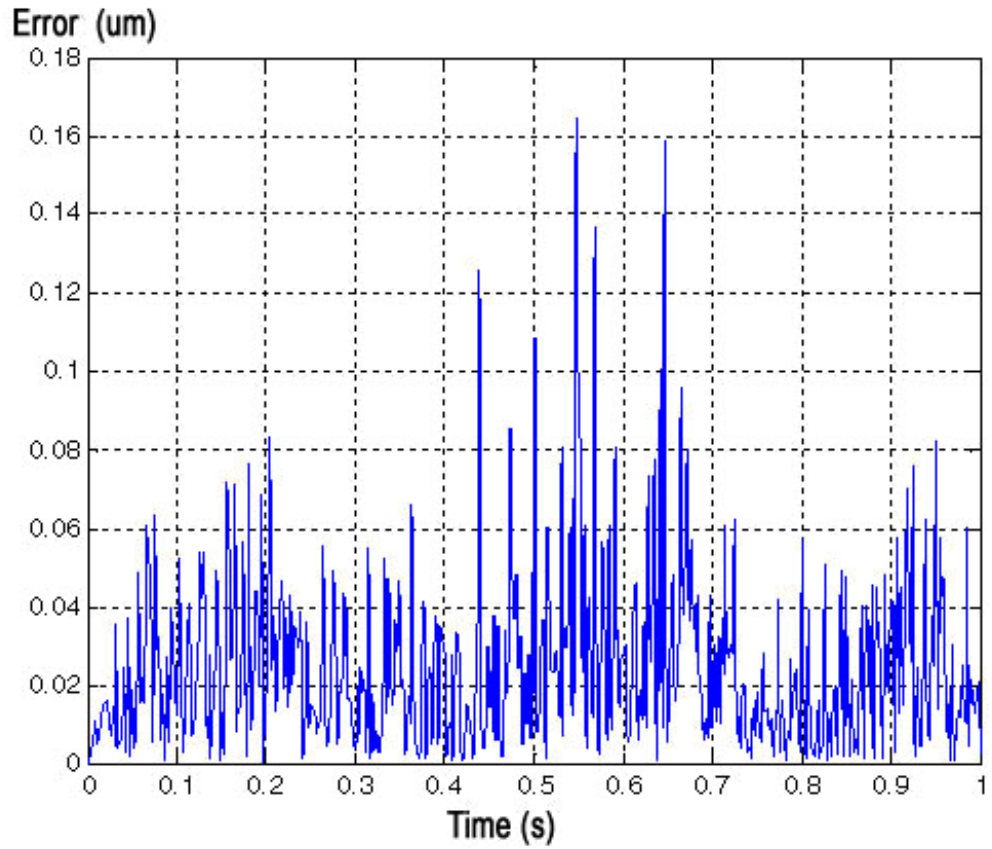


Figure 5.8: Position error of the control system in the XY plane (the maximum error is less than  $0.2 \mu\text{m}$ ).

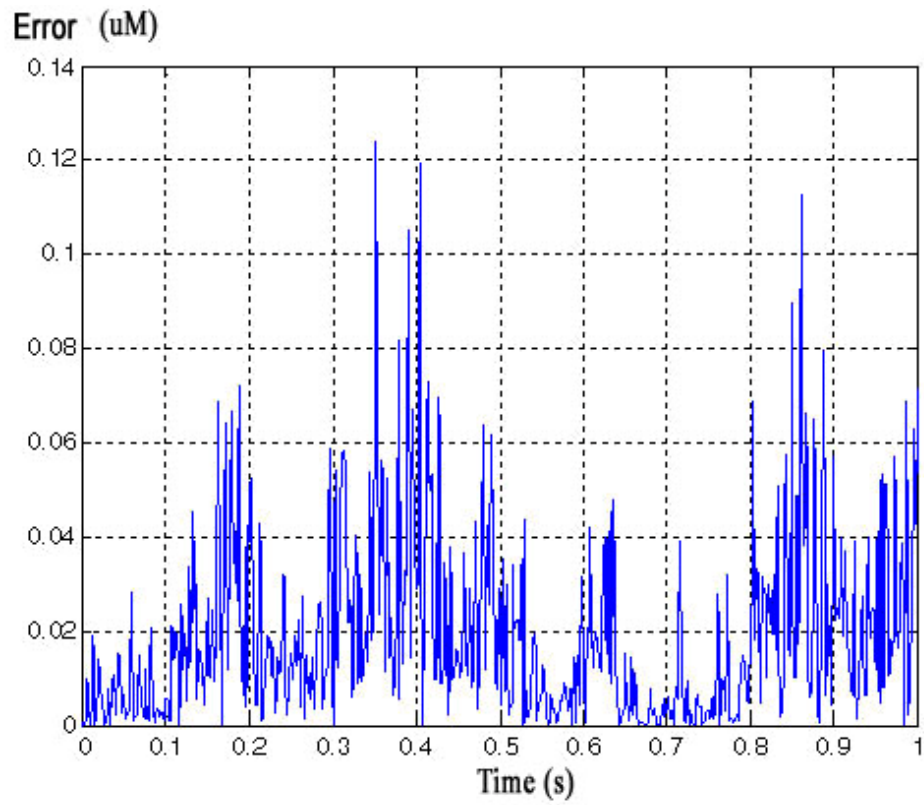


Figure 5.9: The position error of the control system in the Z direction (the maximum error is less than  $0.2 \mu\text{m}$ ).

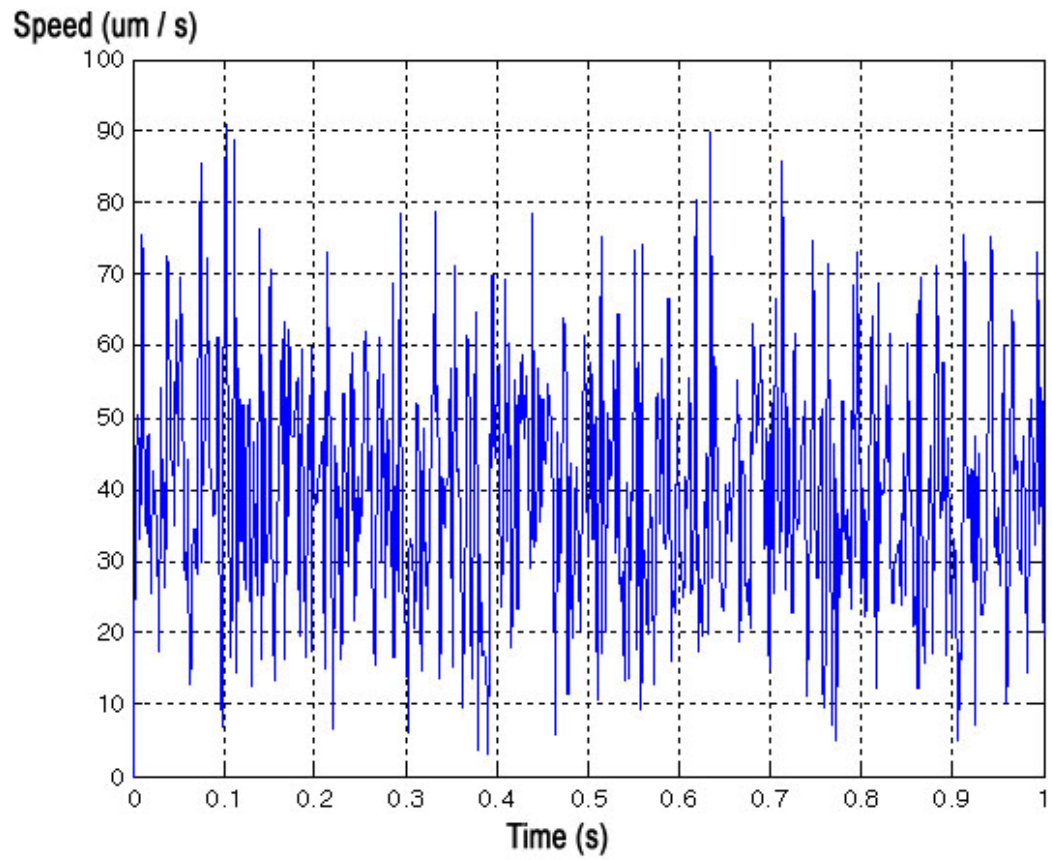


Figure 5.10: Velocity of the laser for tracking the particle in the XY plane.

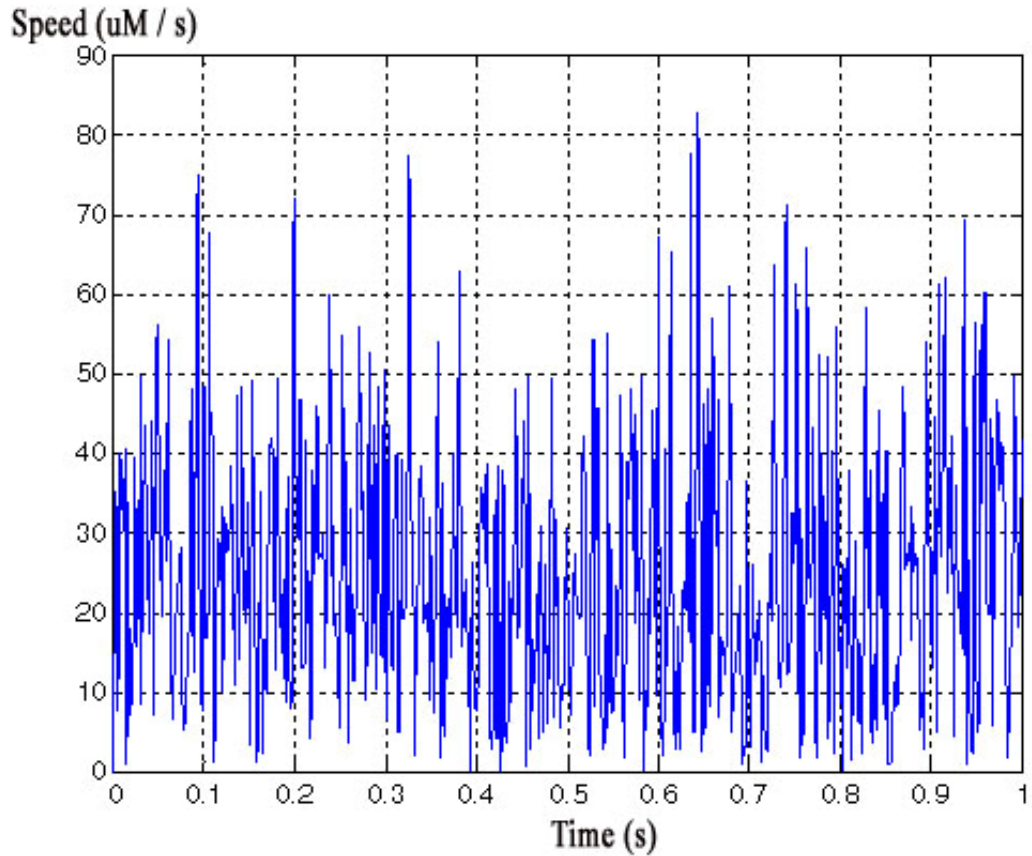


Figure 5.11: Velocity of the stage for tracking the particle in the Z direction.

## 5.6 Related Work

A popular idea for such a control system is to apply the vision system; however, the vision system has some difficulty in sensing a particle in a three dimensional space. For this reason, most of the techniques reported in the literature appear to be suitable for tracking particles in a two-dimensional space. Although there are some reported methods for tracking a particle in a three dimensional space [Timefeld et al., 2005; Peters et al., 1998], they either have limitation in accuracy or are operated in an off-line

manner. Cang et al. [2006] reported a study to use confocal laser scanning microscopy to track a small particle between two cover slips with the edges sealed with wax. In their design, movements of the particle in three dimensions were measured using a CCD camera for the position in the X-Y plane together with an adjusted focus system for the position in the Z-direction, and the position of the particle was then fed back to the controller which was a proportional-integral-derivative control law to determine the updated position of the laser.

## **5.7 Conclusion**

The basic idea behind the control system by which the laser can track the particle that is in Brownian motion was to make use of the feedback of the intensity of the particle's fluorescence signal to determine its position and then to update the position of the laser point. A proper working period needs to be set up beforehand, and the equation for computing the maximum working period must be developed. The selected working period should be less than the maximum working period.

The controller that was proposed and described in this dissertation can track a small particle in fluid with Brownian motion. The simulation of our control system shows that the position tracking error is less than  $0.2 \mu\text{m}$  at any working period. The velocities needed by the laser and stage to track the particle are less than  $100 \mu\text{m} / \text{s}$ , which can easily be achieved by micro motors commercially available.

## CHAPTER 6

### CONCLUSIONS AND FUTURE WORK

#### 6.1 Overview

The overall objective of the study presented in this dissertation was to study an alternative paradigm for measurement of H<sub>2</sub>S in the mammal body. A long-term goal of such a measurement method and its technique is that the measurement should be performed in a real-time, non-invasive, and *in-vivo* manner. A novel idea of the work presented in this dissertation was to take non-functionalized carbon nanotube as a transducer to sense H<sub>2</sub>S in the serum. This idea turns out to be a promising one; in particular, the study presented in this dissertation has successfully verified both experimentally and theoretically that non-functionalized carbon nanotube can bind with H<sub>2</sub>S in the serum with an excellent selectivity. While moving toward this long-term goal, this study successfully developed a novel method that was based on carbon nanotubes and Raman and confocal laser scanning microscopy instruments for measurement of H<sub>2</sub>S. With this method, one is able to measure H<sub>2</sub>S in water and serum using only a tiny amount of samples (e.g., a drop of blood). At present, the 10 μM concentration of H<sub>2</sub>S in water has been measured, and 20 μM concentration of H<sub>2</sub>S in the serum has been measured. This dissertation presents this method.

Specifically, Chapter 1 presented a literature review about H<sub>2</sub>S and its physiological effects, as well as existing measurement methods including their limitations. Chapter 1 thus laid down a foundation about the motivations and objectives for this study. To facilitate the understanding of the developments supporting this work, Chapter 2 discussed some important background knowledge, including activated carbon, carbon nanotube, blood and serum, Raman and laser scanning microscopes, adhesion theories, Brownian motion, and the feedback control system.

Chapter 3 presented the work regarding the measurement of H<sub>2</sub>S using carbon nanotube in aqueous solutions. The hypothesis, materials, and methods for conducting the experiment, as well as the experimental results and the discussion, were presented in detail. Chapter 3 also presented a mechanism that could account for the experimental result – i.e., H<sub>2</sub>S can bind to carbon nanotube in water. Subsequently, Chapter 4 presented the work regarding the measurement of H<sub>2</sub>S using carbon nanotube in serum. Since there are many proteins in serum, their influences over the measurement of H<sub>2</sub>S using carbon nanotubes were then discussed and presented. A side finding regarding the binding between hemoglobin and (non-functionalized) carbon nanotube was also presented in this chapter.

To develop the carbon nanotube approach to measurement of H<sub>2</sub>S, as proposed, into a technique for measurement of H<sub>2</sub>S continuously in a live cell, there is a need to make the laser of either Raman or confocal laser scanning microscopy track a carbon



nanotube in a fluid. The main difficulty for this was that carbon nanotube has an uncertain motion (i.e., Brownian motion) in a fluid, and therefore the carbon nanotube could move out of the laser point. . This demands the availability of a control system associated with microscopes to automatically track the carbon nanotube when it is put in a fluid. Chapter 5 presented a novel control system of that kind which is particularly tied with confocal laser scanning microscopy.

## 6.2 Conclusions

- (1) The use of non-functionalized carbon nanotube to absorb  $\text{H}_2\text{S}$  in distilled water is a valid concept. Because the main components  $\text{Ca}^{2+}$ ,  $\text{Mg}^{2+}$ ,  $\text{Na}^+$  in drinking water are usually inert in reaction with carbon nanotube compared with  $\text{H}_2\text{S}$ , the proposed method based in carbon nanotube offers very good possibility for its use in measurement of  $\text{H}_2\text{S}$  in drinking water at low concentrations.
- (2) The use of non-functionalized carbon nanotube to absorb  $\text{H}_2\text{S}$  in sera is a valid concept. Using the current state-of-the-art instruments for measuring proteins in sera, the proteins in sera (including total protein, albumin, alpha1-globulin, alpha2-globulin, beta globulin, and gamma globulin) do not bind to carbon nanotube.
- (3) The binding of non-functionalized carbon nanotube with methemoglobin can be measured by Raman spectrum; however, such a binding does not change Raman

luminescence. This may further lead to the conclusion that carbon nanotubes can be used to absorb H<sub>2</sub>S in blood, because there is methemoglobin in blood.

### **6.3 Contributions**

Contributions of this dissertation study can be summarized as follows:

- (1) The study has provided a new method to measure low concentration and nano quantity H<sub>2</sub>S in an aqueous solution or in serum. Two of the most important advantages of this method are that it needs only a trace amount of samples (e.g., a drop of serum) and it involves a very simple procedure.
- (2) The study presented a mechanism for the binding between non-functionalized carbon nanotube and H<sub>2</sub>S in aqueous solution and in sera.
- (3) The study discovered that non-functionalized carbon nanotube can bind with methemoglobin. This finding is significant in that it is possible to measure H<sub>2</sub>S in blood with the method developed for measurement of H<sub>2</sub>S in sera.
- (4) Finally, the study presented a method to track a nano-particle in fluids by using its emission luminescence as a means to determine its position in a 3 dimensional space.

## 6.4 Future Work

This study focuses on the measurement of H<sub>2</sub>S in aqueous solutions and in sera. Our ultimate goal is to measure H<sub>2</sub>S in the mammalian body in real time, *in-vivo* and non-invasively. To achieve this goal, many challenges still remain. Differently growing carbon nanotubes have different properties, especially different structures. Why and how these structures might affect the measurement of H<sub>2</sub>S is still unknown. The possible direction for generating answers to this question is to investigate the structures and defects of carbon nanotubes by instruments such as X-Ray and TEM. The response in diffraction information from these instruments can measure the distribution of carbon in the nanotube. TEM with EDS and EELS can be used to detect the elements that attach on the surface of carbon nanotubes.

Further, with these instruments we can observe the effects of certain elements in the adsorption that in turn can improve the adsorption capability of carbon nanotubes. Using TEM with EDS and EELS or GC/MS, we can come to understand the particles that attach to carbon nanotubes which in turn can help us to understand more about the mechanism of the adsorption between H<sub>2</sub>S and carbon nanotube.

The proteins in blood are more complex than the proteins in serum. In order to make use of the method developed in this study for the measurement of H<sub>2</sub>S in blood, the effects of these proteins must be studied. In this study, we used spectrophotometry

and electrophoresis to measure the proteins in serum before and after they interacted with carbon nanotubes in order to observe any change in the proteins. The resolutions of these instruments may not be high enough to reach the conclusion that these proteins do not bind to carbon nanotubes. There is a need to seek more accurate approaches for measurement of proteins in serum.

This dissertation studied only multi-wall carbon nanotubes with non-specific orientations for their binding with  $H_2S$  in water or serum. It would be worthwhile to study (1) single wall carbon nanotubes and/or (2) carbon nanotubes with specific orientations for their binding with  $H_2S$  in water or in serum. This is because multi-wall and single-wall carbon nanotubes are significantly different from each other with regard to the structural features that are relevant to their binding with  $H_2S$ .

Last, the nature of the study presented in this dissertation is to take carbon nanotube as a kind of transducer to observe its binding behaviour with  $H_2S$ . The instruments to make this observation are Raman and confocal laser scanning microscopy. In order to make the measurement based on these instruments in a continuous real-time manner, one straightforward idea is to put a carbon nanotube in the living cell and make the laser of these instruments target on the carbon nanotube. This idea was studied in Chapter 5 of the dissertation. The problem with this idea is that in general, the carbon nanotube has a Brownian motion in the living cell and the scale of such a motion can make the laser off-aligning the carbon nanotube. This problem led us to develop a tracking system on the top of these instruments. The implementation of the

tracking system requires the availability of the motorized stage or laser position of these instruments. A future work is meaningful to explore such an implementation.

Another possibility of instruments to achieve the real-time measurement in the living cell is to design a carbon nanotube transducer. This transducer is expected to have such architecture as composing a substrate which may follow a certain shape and form which are expected to have high sensitivity in terms of mechanical response. Particularly, when the H<sub>2</sub>S molecule binds with the carbon nanotube, mechanical properties of the substrate change, and these changes are then converted to the electronic signal through a certain way to a receiver electronic instrument for reading. The communication between the on-site carbon nanotube with the substrate and the receiver instrument may be via wireless technology.

## REFERENCES

1. Abe, K., and Kimura, H., 1996, "The possible role of hydrogen sulfide as an endogenous neuromodulator", *J. Neurosci.*, 16, 1066–1071.
2. Alireza, R., Johnson, R., Lefkow, A. R., and Healy, K. E., 1999, "Bioactivation of metal oxide surfaces. I. Surface characterization and cell response", *Langmuir*, 15, 6931–6939.
3. Allara, D. L., Fowkes, F. M., Noolandi, J., Rubloff, G. W., and Tirrell, M. V., 1986, "Bonding and Adhesion of Polymer Interfaces", *Materials Science & Engineering*, 83, 213–226.
4. Arp, A. J., and Childress, J. J., 1983, "Sulfide binding by the blood of the hydrothermal vent tube worm *Bifai pachyptifa*", *Science*, 219, 295-297.
5. Ashford, R. D., 1994, *Ashford's Dictionary of Industrial Chemicals*, Wavelength, London.
6. Atkins, P. W., and Paula, J. D., 2002, *Atkins' Physical Chemistry*, 7<sup>nd</sup> ed., Oxford University Press, New York.
7. Bagarinao, T., 1992, "Sulfide as an environmental factor and toxicant: Tolerance and adaptations in aquatic organisms", *Aquatic Toxicol.*, 24, 21–62.
8. Bair, H. E., Matsuoka, S., Vadimsky, R. G., and Wang, T. T., 1971, "Consideration of Energy Dissipation for the Strength of Adhesive Joints", *J. Adhesion*, 3, 89.
9. Baker, F. S., Miller, C. E., Repik, A. J., and Tolles, E. D., 1992, "Activated Carbon", *Kirk-Othmer Encyclopedia of Chemical Technology*, 4, 1015–1037.
10. Bao, L., Vlcek, C., Paces, V., and Kraus, J. P., 1998, "Identification and tissue distribution of human cystathionine beta-synthase mRNA isoforms", *Arch. Biochem. Biophys.*, 350, 95–103.
11. Beauchamp, R. O., Bus, J. S., and Popp, J. A., 1984, "A critical review of the literature on hydrogen sulfide toxicity", *Crit. Rev. Toxicol.*, 13, 25–97.

12. Berber, S., Kwon, Y. K., and Tomànek, D., “Unusually High Thermal Conductivity of Carbon Nanotubes”, *Phys. Rev. Lett.*, 2000, 84.
13. Berglund, A. J., 2007, “*Feedback Control of Brownian Motion for Single-Particle Fluorescence Spectroscopy*”, PhD diss., California Institute of Technology.
14. Bianco, J. H., Godefroy, S., Chaloin, O., Pantarotto, D., Briand, J. P., Muller, S., Prato, M., and Partidos, C. D., 2005, “Cationic Carbon Nanotubes Bind to CpG Oligodeoxynucleotides and Enhance Their Immunostimulatory Properties”, *J. Am. Chem. Soc.*, 127, 58.
15. Brown, S., 1997, “Metal-recognition by repeating polypeptides”, *Nat. Biotechnol.*, 15, 269–272.
16. Brzozka, Z., 2006, Chemical Sensors Research Group, Warsaw University of Technology, Online at <http://csrg.ch.pw.edu.pl> (October 2006).
17. Burtis, C. A., 1999, *Tietz Textbook of Clinical Chemistry*, 3<sup>rd</sup> ed., W. B. Saunders, Philadelphia, 1799–1839.
18. Buzaleh, A. M., Vazquez, E. S., and Carmen, B., 1990, “Cyanide intoxication—III. On the analogous and different effects provoked by non-lethal and lethal challenged doses”. *Gen. Pharmacol.*, 21, 27–32.
19. Canela, M. C., Alberici, R. M., and Jardim, W. F., 1998, “Gas-phase destruction of H<sub>2</sub>S using TiO<sub>2</sub>/UV–VIS”, *J. Photochem. Photobiol. A, Chem.*, 112, 73–80.
20. Cang, H., Wong, C. M., Xu, C. S., and Rizvi, A. H., 2006, “Confocal three dimensional tracking of a single nanoparticle with concurrent spectroscopic readouts”, *Appl. Phys. Letters*, 88, 223901.
21. Carroll, 1998, <http://www.telusplanet.net/public/jcarroll/ION.HTM>.
22. Carroll J. J., and Mather A.E., 1989, “The solubility of hydrogen sulphide in water from 0 to 90 degrees C and pressures to 1 MPa”, *Geochimica Cosmochimica Acta*, 53, 1163–1170.
23. Carroll, J.J. and A.E. Mather, 1989b, "Phase Equilibrium in the System Water-Hydrogen Sulfide: Experimental Determination of the LLV Locus", *Can. Journal of Chem. Eng.*, 67, 468-470.
24. Cassinelli, M. E., 1994, Hydrogen Sulfide, *NIOSH Manual of Analytical Methods (NMAM)*, 4<sup>th</sup> ed., U.S. National Institute of Occupational Safety and Health, Cincinnati.

25. Chen, P., Poddar, R., Tipa, E. V., Dibello, P. M., Moravec, C. D., Robinson, K., Green, R., Kruger, W. D., Garrow, T. A., and Jacobsen, D. W., 1999, "Homocysteine metabolism in cardiovascular cells and tissues: implications for hyperhomocysteinemia and cardiovascular disease", *Adv. Enzyme Regul.*, 39, 93–109.
26. Chen, Y. H., Yao, W. Z., Yao, Geng, B., Ding, Y. L., Lu, M., Zhao, M. W., and Tang, C. S., 2005, "Endogenous Hydrogen Sulfide in Patients With COPD", *Chest*, 128, 3205–3211.
27. Chien, S., Usami, S., Dellenback, R. J., and Gregersen, M. I., 1970, "Shear-dependent interaction of plasma proteins with erythrocytes in blood rheology", *Amer. J. Physiology*, 219, 143–153.
28. Craig, A. S., Shaker, A. M., and Robert M. P., 2006, "Differences in osseointegration rate due to implant surface geometry can be explained by local tissue strains", *J. Orthopaedic Research*, 19, 187–194.
29. Dekker, C., 1999, "Carbon Nanotubes as Molecular Quantum Wires", *Physics Today*, May, 22–28.
30. Dennis, G. S., and Michael, A. P., 2004, "Hydrogen sulfide consumption measured at low steady state concentrations using a sulfidostat", *Anal. Biochem.* 324, 269–75.
31. Deryaguin, B. V., 1955, *Research*, 8, 70.
32. Deryaguin, B. V., Krotova, N. A., Karassev, V. V., Kirillova, Y. M., and Aleinikova, I. N., 1957, *Proceedings of the 2<sup>nd</sup> international congress on Surface Activity–III*, Butterworths, London, 417.
33. Deryaguin, B. V., and Smilga, V. P., 1969, *Adhesion, Fundamentals and Practice*, Mcleren and Son, London, 152.
34. Desilva, F., 2000, "Activated Carbon Filtration", *Water Quality Products Magazine*, January.
35. Don, S., and Lemons, P., 2002, *An Introduction to Stochastic Processes in Physics*, Johns Hopkins University Press, Baltimore, Maryland.
36. Dorman, D. C., Moulin, F. J. M., McManus, B. E., Mahle, K. C., James, R. A., and Struve, M. F., 2002, "Cytochrome Oxidase Inhibition Induced by Acute Hydrogen Sulfide Inhalation: Correlation with Tissue Sulfide Concentrations in the Rat Brain, Liver, Lung, and Nasal Epithelium", *Toxicological Sciences*, 65, 18-25.



37. Dubinin, M. M, 1975a, *Adsorption and Porosity*, Military Technical Academy, Warsaw.
38. Dubinin, M. M, 1975b, *Progress in Surface and Membrane Science vol. 9*, Academic Press, New York.
39. Dujardin, E., Ebbesen, T. W., Krishnan, A., Ylanilos, P. N., and Treacy, M. M. J., 1998, “Young's Modulus of Single-Walled Nanotubes”, *Physical Review B*, 58, 14013–14019.
40. Eto, K., and Kimura, H., 2002, “The production of hydrogen sulfide is regulated by testosterone and S-adenosyl-L-methionine in mouse brain”, *J. Neurochem.*, 83, 80–86.
41. Evens, J. R., and Packham, D. E., 1979, “Adhesion of Polyethylene to Metals: The Role of Surface Topography”, *J. Adhesion*, 10, 177–191.
42. Everett, D. H., 1973, Part I: Definitions, Terminology and Symbols in Colloid and Surface Chemistry, *Pure Appl. Chem.*, 31, in *IUPAC Manual Appendix II*, 579–631.
43. Everett, D. H., 1976, Part II: Terminology in Heterogeneous Catalysis, *Pure Appl. Chem.* 45, in *IUPAC Manual Appendix II*, 71–90.
44. Feng, W., 2005, “Hydrogen sulfide adsorption/oxidation on carbonaceous surfaces and its application in vapor phase mercury control”, PhD. diss. University of Pittsburgh.
45. Fowkes, F. M., 1987, “Role of Acid-Base Interfacial Bonding in Adhesion”, *J. Adhesion Science and Technology*, 1, 7–27.
46. Fraissard, J. P., 1997, *Physical Adsorption: Experiment, Theory and Applications*, Springer, New York.
47. Frank, S., Poncharal, P., Wang, Z. L., and Heer, W. A., 1998, “Carbon Nanotube Quantum Resistors”, *Science*, 280, 1744.
48. Furimsky, E., 1997, “Activity of spent hydroprocessing catalysts and carbon supported catalysts for conversion of hydrogen sulphide”. *Appl. Catal. A: Gen.* 156, 207–218.
49. Gernerden, H., Van Tughan, C. S., De Wit, R., and Herbert, R. A., 1989, “Laminated microbial ecosystems on sheltered beaches in Scapa Flow, Orkney Islands FEMS (Fed. Eur. Microbial. Soc.)”, *Microbiol. Ecol.* 62, 87.

50. Glass, D. C., 1990, "A review of the health effects of hydrogen sulphide exposure". *Ann. Occup. Hyg.*, 34, 323–327.
51. Gleason, N. J., Nodes, C. J., Higham, E. M., Guchert, N., Aksay, I. A., Schwarzbauer, J. E., and Carbeck, J. D., 2003, "Patterning proteins and cells using two-dimensional arrays of colloids", *Langmuir*, 19, 513–518.
52. Gledhill, R. A., Kinloch, A. J., and Shaw, S. J., 1980, "A Model for Predicting Joint Durability", *J. Adhesion*, 11, 3–5.
53. Guidotti, T. L., 1996, "Hydrogen sulphide", *Occup. Med.* 46, 367–371.
54. Gunina, A. I., 1959, "Oxidation of hydrogen sulfide in the organism", *U.S. Atomic Energy Commission, Report No. AEC*, 3661, 534–541.
55. Hannestad, U., Margheri S., and Sörbo, B., 1989, "A sensitive gas chromatographic method for determination of protein-associated sulfur", *Anal. Biochem.*, 178, 394–398.
56. Hansen, K. M., Ji, H. F., Wu, G. H., Datar, R., Cote, R., Majumdar, A., and Thundat, T., 2001, "Cantilever-based optical deflection assay for discrimination of DNA single-nucleotide mismatches", *Anal. Chem.*, 73, 1567–1571.
57. He, X. M., and Carter, D. C., 1992, "Atomic structure and chemistry of human serum albumin", *Nature*, 358, 209–215.
58. Hedden, K., Huber, L., and Rao, B. R., 1976, "Adsorptive Reinigung von schwefelwasserstoffhaltigen Abgasen", in *Technische Sorptionverfahren zur Reinhaltung der Luft. Tagung Nurnberg 1975*, 6, VDI-Verlag, Dusseldorf.
59. Hine, P. J., Muddarris, S. E., and Packham, D. E., 1984, "Surface Pretreatment of Zinc and its Adhesion to Epoxy Resins", *J. Adhesion*, 17, 207.
60. Hone, J., Whitney, M., and Zettl, A., 1999, "Thermal conductivity of single-walled carbon nanotubes", *Synthetic Metals*, 103, 2498–2499.
61. Hosoki, R., Matsuki, N., and Kimura, H., 1997, "The possible role of hydrogen sulfide as an endogenous *smooth muscle* relaxant in synergy with nitric oxide", *Biochem Biophys Res Commun*, 237, 527–531.
62. Howard, P. H., and Meylan, W. M., 1992, *Henry's Law Constant Program*, CRC Press, Boca Raton, FL.
63. HSDB, 1998, *Hazardous Substances Data Bank*, National Library of Medicine, Bethesda, MD.

64. Huang, K., 2005, *Lectures on statistical physics and protein folding*, World Scientific, Hackensack, N.J.
65. Imamura, T., Kage, S., and Kudo, K., 1996, "A case of drowning linked to ingested sulfides: a report with animal experiments", *Int. J. Legal Med.*, 109, 42–44.
66. Jacobs, O. L. R., 1996, *Introduction to Control Theory*, 2<sup>nd</sup> ed., Oxford University Press, New York.
67. Jennings, C. W., 1972, "Surface Roughness and Bond Strength of Adhesives", *J. Adhesion*, 4, 25.
68. Jiang, K., Schadler, L. S., Siegel, R. W., Zhang, X., Zhang, H., and Terrones, M., 2004, "Protein immobilization on carbon nanotubes via a two-step process of diimide-activated amidation", *J. Materials Chemistry*, 14, 37–39.
69. Kage, S., Nagata, T., and Kimura, K., 1992, "The usefulness of thiosulfate as an indicator of hydrogen sulfide poisoning in forensic toxicological examination: A study with animal experiments", *Jpn. J. Forensic Toxicol.*, 10, 223–227.
70. Kam, N. W. S., and Dai, H., 2005, "Carbon Nanotubes as Intracellular Protein Transporters: Generality and Biological Functionality", *J. Am. Chem. Soc.*, 127, 6021–6026.
71. Kangas, J., and Savolainen, H., 1987, "Urinary thiosulphate as an indicator of exposure to hydrogen sulphide vapour", *Clinica. Chimica. Acta.*, 164: 7–10.
72. Karatzas, I., and Schreve, S. E., 1988, *Brownian Motion and Stochastic Calculus*, Springer–Verlag, New York.
73. Katoh, H., Kuniyoshi, I., Hirai, M., and Shoda, M., 1995, "Studies of the oxidation mechanism of sulfur containing gases on wet activated carbon fibre", *Appl. Catal. B: Env.*, 6, 255–262.
74. Kerker, M., Wang, D. S., Chew, H., Siiman, O., and Bumm, L.A., 1982, *Surface Enhanced Raman Scattering*, edited by Chang, R. K., and Furtak, T. E., Plenum Press, New York, 109–128.
75. Khalil, H., 1996, *Nonlinear System*, 2<sup>nd</sup> ed., Macmillan, New York.
76. Kim, S. R., 2000, "Surface Modification of Poly (tetrafluoroethylene) Film by Chemical Etching, Plasma, and Ion Beam Treatments", *J. Applied Polymer Science*, 77, 1913.

77. Kinloch, A. J., 1987, *Adhesion and Adhesives: Science and Technology*, Springer, New York.
78. Kinloch, A. J., 1980, "The Science of Adhesion", *J. Materials Science*, 15, 216.
79. Kinloch, A. J., 1979, "Interfacial Fracture Mechanical Aspects of Adhesive Bonded Joints—A Review", *J. Adhesion*, 10, 193–219.
80. Klein, J., and Henning, K. D, 1984, "Catalytic oxidation of hydrogen sulphide on activated carbons", *Fuel Mag.*, 63, 1064–1067.
81. Knezovich, J. P., Jelinski, J. A., Anderson, S. L., and Steichen, D. J., 1994, "Sulfide tolerance of four marine bioassay test species used to evaluate sediment toxicity", Paper presented at 15th annual meeting of Society of Environmental Toxicology and Chemistry or Ecological Risk: Science, Policy, Law, and Perception, 30 Oct.—3 Nov., Denver, CO.
82. Kosmider, S., Rogala, E., and Pacholek, A., 1967, "Electrocardiographic and histochemical studies of the heart muscle in acute experimental hydrogen sulfide poisoning", *Arch. Immun. Ther. Exp.*, 15, 731–740.
83. Lambiotte, A., 1942, Process of continuous carbonation of cellulosic materials, US patent # 2,289,917.
84. Lavrik, N. V., Tipple, C. A., Sepaniak, M. J., and Datskos, P. G., 2001, "Gold nano-structures for transduction of biomolecular interactions into micrometer scale movements", *Biomedical Microdevices*, 3, 35–44.
85. Lee, L. H., 1991, *Fundamentals of Adhesion*, 1<sup>st</sup> ed., Springer, New York.
86. Levinson, S. O., and Finkelstein, R., 1942, "Blood Serum and Plasma Transfusions", *The American Journal of Nursing*, 42, 35–38.
87. Levonen, A. L., Lapatto, R., Saksela, M., and Raivio, K. O., 2000, "Human cystathionine gamma-lyase: Developmental and in vitro expression of two isoforms", *Biochem. J.*, 347, 291–295.
88. Loader, J., 1970, *Basic Laser Raman Spectroscopy*, Heyden & Son, London.
89. Long, D., 1971, *Raman Spectroscopy*, McGraw-Hill, New York.
90. Lorans, E., 1996, "Contribution à la caractérisation de la qualité de l'air des ouvrages souterrains de la RATP. Les sources de composés volatils et leur impact olfactif", Ph.D. diss., Université de Rennes.

91. Lu, Q., Moore, J. M., Huang, G., Mount, A. S., Rao, A. M., Larcom, L. L., and Ke, P. C., 2004, "RNA polymer translocation with single-walled carbon nanotubes", *Nano Lett.*, 4, 2473.
92. Lu, Y., O'Dowd, B. F., Orrego, H., and Isreal, Y., 1992, "Cloning and nucleotide sequence of human liver cDNA encoding for cystathionine gamma-lyase", *Biochem. Biophys. Res. Commun.*, 189, 749–758.
93. Marsh, H., and Rodrigues, F., 2006, *Activated Carbon*, Elsevier, UK.
94. Masuda, J., Fukuyama, J., and Fujii, S., 1999, "Influence of concurrent substances on removal of hydrogen sulfide by activated carbon", *Chemosphere*, 39, 1611–1616.
95. Matlab Program, <http://www-math.bgsu.edu/~zirbel/sde>
96. Mattson, J. S., and Mark, H. B. Jr., 1971, *Activated Carbon*, Dekker, New York.
97. McBain, J.W., and Hopkins, D.G., 1925, "On adhesives and adhesive action", *J. Phys. Chem.*, 29, 188.
98. Mehlman, M. A., 1994, "Dangerous and cancer-causing properties of products and chemicals in the oil refining and petrochemical industry. Part VII: Adverse health effects and toxic manifestations caused by exposure to hydrogen sulfide, a component of crude oil", *J. Clean Technol. Environ. Sci.*, 4.
99. Meier, M., Janosik, M., Kery, V., Kraus, J. P., and Burkhard, P., 2001, "Structure of human cystathionine beta-synthase: A unique pyridoxal 5-phosphate-dependent heme protein", *EMBO J.*, 20, 3910–3916.
100. Michael L., 2000, *Clinical Chemistry: Principles, Procedures, Correlations*, Lippincott Williams & Wilkins, Philadelphia, 25.
101. Milby, T. H., and Baselt, R. C., 1999a, "Health hazards of hydrogen sulfide: current status and future directions", *Environ. Epidemiol. Toxicol.*, 1, 262–269.
102. Miller, J. M., 2005, *Chromatography: Concepts and Contrasts*, 2<sup>nd</sup> ed., Wiley, NJ.
103. Miron, G., and Kristensen, E., 1993, "Behavioral response of three nereid polychaetes to injection of sulfide inside burrows", *Mar. Ecol. Prog. Ser.*, 101, 147–155.

104. Mitchell, T. W., Savage, J. C., and Gould, D. H., 1993, "High-performance liquid chromatography detection of sulfide in tissues from sulfide-treated mice", *J. Appl. Toxicol.*, 13, 389–394.
105. Moore, P. K., Bhatia, M., and Moochhala, S., 2003, "Hydrogen sulfide: from the smell of the past to the mediator of the future?" *Trends Pharmacol. Sci.*, 24, 609–611.
106. Morris, M. D., 1992, Chapter 6 in *Applied Laser Spectroscopy*; edited by Andrews, D. L., VCH Publishers, New York.
107. Myers, A. B., and Mathies, R. A., 1987, Chapter 1 in "*Biological Applications of Raman Spectroscopy*", Vol. 2 *Resonance Raman Spectra of Polyenes and Aromatics*, edited by Spiro, T. G., John Wiley and Sons, New York.
108. Nebergall, W. H., 1968, *Generaal Chemistry*, D. C. Health and Company, Lexington, MA.
109. Nihlstrand, A., 1996, "Plasma modification of polypropylene materials for improved adhesion". Ph.D. diss, Goteborg: Chalmers University of Technology.
110. NIOSH, 1979, *NIOSH Manual of Analytical Methods (NMAM)*, 2<sup>nd</sup> ed., U.S. National Institute of Occupational Safety and Health, Cincinnati.
111. Odom, T. W., Huang, J. L., Kim, P., and Lieber, C. M., 1998, "Atomic structure and electronic properties of single-walled carbon nanotubes", *Nature*, 391, 6662–6664.
112. Olivieri, J. R., and Craievich, A. F., 1995, "The subdomain structure of human serum albumin in solution under different pH conditions studied by small angle X-ray scattering", *European Biophysics Journal*, 77–84.
113. Oscik, J., 1982, *Adsorption*, Ellis Horwood, Warsaw.
114. Oseid, D. M., and Smith, L. L., 1974a, "J. Factors influencing acute toxicity estimates of hydrogen sulfide to freshwater invertebrates", *Water Res.*, 8, 739–746.
115. Oseid, D. M., and Smith, L. L., 1974b, "Chronic toxicity of hydrogen sulfide to *Gammarus pseudolimnaeus*", *Trans. Amer. Fish. Soc.*, 4, 819–822.
116. Pace, N. R., 1997, "A molecular view of microbial diversity and the biosphere", *Science*, 276, 734–740.

117. Packham, D. E., 1981, *Developments in Adhesives*, 2<sup>nd</sup>, Applied Science Pub., London, 315.
118. Packham, D. E., 1983, *Adhesion Aspects of Polymeric Coatings*, Plenum, New York, 19.
119. Pantarotto, D., Briand, M., and Prato, A. B., 2004, “Translocation of Bioactive Peptides across Cell Membranes by Carbon Nanotubes”, *A. Chem. Comm.* 1, 16.
120. Patacchini, R., Santicoli, P., Giuliani, S., and Maggi, C. A., 2005, “Pharmacological investigation of hydrogen sulfide (H<sub>2</sub>S) contractile activity in rat detrusor muscle”, *Eur J Pharmacol*, 509, 171–177.
121. Pearson, T. H., and Rosenberg, R., 1978, “Macrobenthic succession in relation to organic enrichment and pollution of the marine environment”, *Oceanogr. Mar. Biol. Ann. Rev.*, 16, 229–311.
122. Persson, B. N. J., 1992, “Ordered structures and phase transitions in adsorbed layers”, *Surface Science Reports*, 15, 1–135.
123. Peters, L. M., Grooth, B. de, Schins, J. M., Figdor, C. G., and Greve, J., 1998, “Three dimensional single-particle tracking with nanometer resolution”, *Rev. Sci. Instrum.*, 69, 2762–2766.
124. Pilarczyk, E, Henning, K-D., and Knoblauch, K., 1987, “Natural gas from landfill gases Resources Conservation”, *International symposium on materials and energy*, 14, 283–294.
125. Poor, H.V., 1994, *An Introduction to Signal Detection and Estimation*, 2<sup>nd</sup> ed., Springer, New York.
126. Primavera, A., Trovarelli, A., Andreussi, P., and Dolcetti, G., 1998, “The effect of water in the low-temperature catalytic oxidation of hydrogen sulfide to sulfur over activated carbon”, *Appl. Catal. A, Gen.*, 173, 185–192.
127. Rampling, M. W., 1988, “Red cell aggregation and yield stress” in *Clinical Blood Rheology*, Vol. 1, edited. by G. D. O. Lowe, CRC Press, Boca Ration, Florida, 65–86.
128. Reiffenstein, R. J., Hulbert, W. C., and Roth, S. H., 1992, “Toxicology of hydrogen sulfide”, *Annu. Rev. Pharmacol. Toxicol.*, 32, 109–134.
129. Richardson, C. J., Magee, E. A., and Cummings, J. H., 2000, “A new method for the determination of sulphide in gastrointestinal contents and whole blood

- by microdistillation and ion chromatography”, *Clin. Chim. Acta*, 293, 115–125.
130. Robert, B. E., and Tremaine, P. R., 1985, “Vapour Liquid Equilibrium Calculations for Dilute Aqueous Solutions of CO<sub>2</sub>, H<sub>2</sub>S, NH<sub>3</sub> and NaOH to 300°C”, *Can. J. Chem. Eng.*, 63, 294-300.
  131. Rodriguez-Reinoso, F., and Linares-Solano, A., 1989, *Chemistry and physics of carbon: A series of advances*, edited by P. A. Thrower, Marcel Dekker, New York.
  132. Roth, S. H., Skrajny, B., and Reiffenstein, R. J., 1995, “Alteration of the morphology and neurochemistry of the developing mammalian nervous system by hydrogen sulfide”, *Clin. Exp. Pharmacol. Physiol.*, 22, 379–380.
  133. Rudee, M. L., and Price, T. M., 1985, “The initial stages of adsorption of plasma derived proteins on artificial surfaces in a controlled flow environment”, *J. Biomed. Mater. Res.*, 19, 57–66.
  134. Sakurai, T., and Watanabe, Y., 2000, *Advances in Scanning Probe Microscopy*, Springer Verlag, London, UK.
  135. Salvador-Morales, E., Flahaut, E., Sim, J., Sloan, M. L. H., Green, R., and Sim, B., 2006, “Complement activation and protein adsorption by carbon nanotubes”, *Molec. Immun.*, 43, 193–201.
  136. Schewe, P. F., and Stein, B., 1996, “Physics News Update”, *The American Institute of Physics Bulletin of Physics News*, 279.
  137. Scott, F. G., 1997, *Developmental Biology*, 5<sup>th</sup> ed., Sinauer Associates, Sunderland, MA.
  138. Schrader, B., 1995, Chapter 4 in *Infrared and Raman Spectroscopy*; edited by Schrader, B., VCH Publishers, New York.
  139. Searcy, D. G., and Lee, S. H., 1998, “Sulfur reduction by human erythrocytes”, *J. Exp. Zool.*, 282, 310–322.
  140. Shier, D., Lewis, R., and Butler, J., 2002, *Hole's Human Anatomy & Physiology*, 9<sup>th</sup> ed., McGraw Hill.
  141. Skoog, D. A., Holler, F. Z., and Neiman, T. A., 1998, *Principles of Instrumental Analysis*, 5<sup>th</sup> ed., Harcourt Brace, Philadelphia, PA..
  142. Smith, J. R., 1980, *Theory of Chemisorption*, Springer, New York.



143. Smith, R. P., and Gosselin, R. E., 1979, "Hydrogen sulfide poisoning", *J. Occup. Med.*, 21, 93–97.
144. Smith, R. P., and Abbanat, R. A., 1966, "Protective effect of oxidized glutathione in acute sulfide poisoning", *Toxicol. Appl. Pharmacol.*, 9, 209–217.
145. Spires, T., and Brown, R. M., 1996, High Resolution TEM Observations of Single-Walled Carbon Nanotubes, Jr. Department of Botany, University of Texas at Austin.
146. Stipanuk, M. H., and Beck, P. W., 1982, "Characterization of the enzymic capacity for cysteine desulphhydration in liver and kidney of the rat". *J. Biochem*, 206, 267–277.
147. Stoney, G., 1909, "The tension of metallic films deposited by electrolysis", *Proc. Roy. Soc., London*, A, 82, 172.
148. Stuart, J., 1988, "Erythrocyte deformability", *Clinical Blood Rheology*, Vol.1, edited. by G. D. O. Lowe, CRC Press, Boca Ration, Florida, 65-86.
149. Thess, A., Lee, R., Nikolaev, P., Dai, H., Petit, P., Robert, J., Xu, C., Lee, Y. H., Kim, S. G., Rinzler, A. G., Colbert, D. T., Scuseria, G., Tománek, D., Fischer, J. E., and Smalley, R. E., 1996, "Crystalline Ropes of Metallic Carbon Nanotubes", *Science*, 273, 483.
150. Thurston, G. B., 1972, "The viscoelasticity of human blood", *Biophysical Journal*, 12, 1205–1217.
151. Thurston, G. B., 1996, *Viscoelastic properties of blood and blood analogs*, *Advances in Hemodynamics and Hemorheology*, edited by T. C. Howe, JAI Press, Greenwich, CT, 1–30.
152. Timefeld, P., and Sauer, M., 2005, Branching Out of Single-Molecule Fluorescence Spectroscopy: Challenges for Chemistry and Influence on Biology, *Angew.Chem. int. Ed.*, 44, 2642-2671.
153. Toth, J., 2002, *Adsorption Theory, Modeling, and Analysis*, Marcel Dekker, New York.
154. Tres, P. A., 2000, *Designing Plastic Parts for Assembly*, 4<sup>th</sup> ed., Hanser Gardbner, Cincinnati, Ohio, XXV + 262
155. Trupper, H. G., and Schlegel, H. G., 1964, "Sulphur metabolism in Thiorhodaceae: 1. Quantitative measurements on growing cells of *Chromatium okenii*. Antonie van Leeuwenhoek", *J. Microbial. Serol.*, 30, 225.

156. Tsai, J. H., Jeng, F. T., and Chiang, H. L., 2001, "Removal of H<sub>2</sub>S from Exhaust Gas by Use of Alkaline Activated Carbon", *Adsorption*, 7, 357–366.
157. Ubuka T., 2002, "Assay methods and biological roles of labile sulfur in animal tissues", *J. Chromatography B*, 781, 227–249.
158. Van der Molen, E. F., Hiipakka, M. J., van Lith-Zanders, H., Boers, G. H., van den Heuvel, L. P., Monnens, L. A., and Blom, H. J., 1997, "Homocysteine metabolism in endothelial cells of a patient homozygous for cystathionine beta-synthase (CS) deficiency", *Thromb. Haemost.*, 78, 827–833.
159. Varadan, V. K., and Xie, J., 2002, "Large-scale synthesis of multiwalled carbon nanotubes by microwave CVD", *Smart Mater. Struct.*, 11, 610–616.
160. Veiseh, M., Zareie, M. H., and Zhang, M., 2002, "Highly selective protein patterning on gold-silicon substrates for biosensor applications", *Langmuir* 18, 6671–6678.
161. Wagner, P., Nock, S., Spudich, J. A., Volkmuth, W. D., Chu, S., Cicero, R. L., Wade, C. P., Linford, M. R., and Chidsey, C. E., 1997, "Bioreactive self-assembled monolayers on hydrogen-passivated Si(111) as a new class of atomically flat substrates for biological scanning probe microscopy", *J. Struct. Biol.*, 119, 189–201.
162. Wake, W. C., 1982, *Adhesion and the Formulation of Adhesives*, Applied Science Pubs., London.
163. Wang, R., 2004, *Signal Transduction and the Gasotransmitters: NO, CO, and H<sub>2</sub>S in Biology and Medicine*, Humana Press, Totowa, N.J.
164. Wang R, 2002, "Two's company, three's a crowd—can H<sub>2</sub>S be the third endogenous gaseous transmitter", *FASEB J.*, 16, 1792–1798.
165. Wang, R., 1998, "Resurgence of carbon monoxide: an endogenous gaseous vasorelaxing factor", *Can. J. Physiol. Pharmacol.*, 76, 1–15.
166. Wang, R., Wu, L., and Wang, Z. Z., 1997, "The direct effect of carbon monoxide on KCa channels in vascular smooth muscle cells", *Pflugers Arch.*, 434, 285–291.
167. Wang, R., Wang, Z. Z., and Wu, L., 1991, "Carbon monoxide-induced vasorelaxation and the underlying mechanisms". *Br. J. Pharmacol.*, 121, 927–934.

168. Wang, T. T., and Vazirani, H. N., 1972, "Peel Strength and Failure Mechanisms in Oxidized Copper-Polyethylene Lap Joints Bonded with Flexible Epoxy", *J. Adhesion*, 4, 353.
169. Warenycia, M. W., Goodwin, L. R., Benishin, C. G., Reiffenstein, R. J., Francom, D. M., Taylor, J. D., and Dieken, F. P., 1989, "Acute hydrogen sulfide poisoning: Demonstration of selective uptake of sulfide by the brainstem by measurement of brain sulfide levels", *Biochem. Pharmacol.*, 38, 973–981.
170. Weidner, C. L., 1963, "Pressure-Sensitive Adhesive Compounds from Rubber, Tackifying Resins, Polyamines and Peroxides", *Adhesives Age*, 6, 30.
171. Westely, A. M., and Westley, J., 1991, "Biological sulfane sulfur". *Biochemistry*, 195, 63–67.
172. Whaley, S., English, D. S., Hu, E. L., Barbara, P. F., and Belcher, A. M., 2000, "Selection of peptides with semi-conductor binding specificity for directed nanocrystal assembly", *Nature*, 405, 665–668.
173. Wheeler, L. A., 1998, *Clinical Laboratory Instrumentation, Medical Instrumentation: Application and Design*, Wiley, New York, 486.
174. Wieckowska, J., 1995, "Catalytic and adsorptive desulphurization of gases". *Catal. Today*, 24, 405–465.
175. Wildoer, J. W. G., Venema, L. C., Rinzler, A. G., Smalley, R. E., and Dekker, C., 1998, "Electronic structure of atomically resolved carbon nanotubes", *Nature*, 391, 59–62.
176. Willett, R. L., Baldwin, K. W., West, K. W., and Pfeiffer, L. N., 2005, "Differential adhesion of amino acids to inorganic surfaces", *PNAS*, 102, 7817-7822.
177. Winder, C. V., and Winder, H. O., 1933, "The seat of action of sul@de on pulmonary ventilation", *Am. J. Physiol.*, 105, 337-352.
178. Wu, D. Q., 2006, "An Experimental study of the measurement of low concentration hydrogen sulfide in an aqueous solution", MSc. thesis. Biomedical Engineering, University of Saskatchewan.
179. Wu, J. F., 2004, "Modeling Adsorption of Organic Compounds on Activated Carbon", Ph.D. dissertation, Analytical Chemistry, Department of Chemistry, Umeå University.

180. Wu, X. C., Wu, D. Q., Sammynaiken, R., Zhang, W. J., Yang, W., and Wang, R., 2005, "A New Paradigm for Measurement of Hydrogen sulfide in Blood or Serum", *Experimental & Clinical Cardiology*, 10, 53.
181. Wu, X. C., Zhang, W. J., Wu, D. Q., Sammynaiken, R., Wang, R., and Yang, Q., 2006, "Using Carbon Nanotubes To Absorb Low Concentration Hydrogen Sulfide In Fluid", *IEEE Transaction of NanoBioScience*, 5, 204–209.
182. Wu, X. C., Zhang, W. J., Wang, R., Meng, Q. H., Wu, D. Q., Sammynaiken, R., Yang, Q., Yang, W., and Zhang, E. M., 2007, "Measurement of Low Concentration and Nano Quantity Hydrogen Sulfide in Serum Using the Carbon Nanotubes", *IEEE Transaction of NanoBioScience*, accept.
183. Wu, X. C., Sammynaiken, R., Zhang, W. J., Wu, D. Q., Yang, Q., Yang, W., and Wang, R., 2007, "Measurement of low concentration and nano-quantity hydrogen sulfide in aqueous solution: Measurement mechanisms and limitations", *Meas. Sci. Technol.*, 18, 1315–1320.
184. Yang, Q., Xiao, C., Chen, W., Singh, A. K., Asai, T., and Hirose, A., 2003, "Growth mechanism and orientation control of well-aligned carbon nanotubes", *Diamond and Related Materials*, 12, 1482–1487.
185. Yap, S., Naughten, E. R., Wilcken, B., Wilcken, D. E., and Boers, G. H., 2000, "Vascular complications of severe hyperhomocysteinemia in patients with homocystinuria due to cystathionine beta-synthase deficiency: Effects of homocysteine-lowering therapy", *Semin. Thromb. Hemost.*, 26, 335–340.
186. Yeo, W. S., Yousaf, M. N., and Mrksich, M., 2003, "Dynamic interfaces between cells and surfaces: Electroactive substrates that sequentially release and attach cells", *J. Am. Chem. Soc.*, 125, 14994–14995.
187. Yu, M. F., Files, B. S., Arepalli, S., and Ruoff, R. S., 2000, "Tensile Loading of Ropes of Single Wall Carbon Nanotubes and their Mechanical Properties", *Phys. Rev. Lett.*, 84, 5552.
188. Zhao, W., Ndisang, J. F., and Wang, R., 2003, "Modulation of endogenous production of H<sub>2</sub>S in rat tissues", *Can. J. Physiol. Pharmacol.*, 81, 848-853.
189. Zhao, W., Zhang, J., Lu, Y., and Wang, R., 2001, "The vasorelaxant effect of H<sub>2</sub>S as a novel endogenous gaseous K<sub>ATP</sub> channel opener", *EMBO J.*, 20, 6008–6016.

## APPENDIX A: MOST LIKELIHOOD ESTIMATOR

Maximum likelihood estimation (MLE) is a popular statistical method used to calculate the best way of fitting a mathematical model to some data. The propose of using maximum likelihood parameter estimation is to determine the parameters that maximize the probability (likelihood) of the sample data. From a statistical point of view, the method of maximum likelihood, which yields estimators with good statistical properties, is considered to be more robust and apply to most models. From this method, one can get uncertainty through confidence bounds.

If  $x$  is a continuous random variable with probability density function (pdf):

$$f(x; \theta_1, \theta_2, \dots, \theta_k) \tag{A1}$$

where  $\theta_1$  to  $\theta_k$  are  $k$  unknown constant parameters which need to be estimated; and  $N$  is numbers of independent observations. Then the likelihood function is given by the following product:

$$L(x_1, x_2, \dots, x_N | \theta_1, \theta_2, \dots, \theta_k) = \prod_{i=1}^N f(x_i; \theta_1, \theta_2, \dots, \theta_k) \tag{A2}$$

$i = 1, 2, \dots, N$

The logarithmic likelihood function is given by:

$$\Lambda = \ln L = \sum_{i=1}^N \ln f(x_i; \theta_1, \theta_2, \dots, \theta_k) \quad (\text{A3})$$

The maximum likelihood estimators (MLE) of  $\theta_1$  to  $\theta_k$  are obtained by maximizing  $\Lambda$ . The maximized  $\Lambda$  for  $\theta_1$  to  $\theta_k$  are:

$$\frac{\partial(\Lambda)}{\partial\theta_j} = 0, \quad j = 1, 2, \dots, k \quad (\text{A4})$$

Let  $P(I(n), \mathbf{A})$  denote the probability density of the measurements given the location of the source  $\mathbf{A}$  and assuming that each measurement is independent. The  $P(I(n), \mathbf{A})$  is an N-dimensional Gaussian distribution with the probability density function  $I(n)$ :

$$P(I(n), \mathbf{A}) = \frac{1}{\sigma\sqrt{2\pi}} e^{-\frac{(I(n) - \mathbf{A})^2}{2\sigma^2}} \quad (\text{A5})$$

where  $\mathbf{A}$  is the position of the particle,  $\sigma$  is the spread of the function.  $\sigma^2$  is the variance .

The probability of  $I$  in period  $t$  becomes

$$P(I, \mathbf{A}) = \prod_{n=0}^{N-1} P(I(n), \mathbf{A}) = \frac{1}{\sigma\sqrt{2\pi}} e^{-\frac{1}{2\sigma^2} \sum_{n=0}^{N-1} (I(n) - A)^2} \quad (\text{A6})$$

$$\ln P(I, \mathbf{A}) = -N \ln(\sigma\sqrt{2\pi}) - \frac{1}{2\sigma^2} \sum_{n=0}^{N-1} (I(n) - A)^2 \quad (\text{A7})$$

and the maximum likelihood estimator is the maximum of the nature logarithm of P(I, A) [Poor, 1994],

$$\hat{\mathbf{A}} = \arg \max \ln P(I, \mathbf{A}) \quad (\text{A8})$$

The differential of the Equation A7, we have:

$$\frac{\partial}{\partial A} \ln P(I, \mathbf{A}) = \frac{1}{\sigma^2} [\sum_{n=0}^{N-1} (I(n) - A)] = \frac{1}{\sigma^2} [\sum_{n=0}^{N-1} I(n) - NA] \quad (\text{A9})$$

and setting it to zero

$$0 = \frac{1}{\sigma^2} [\sum_{n=0}^{N-1} I(n) - NA] = [\sum_{n=0}^{N-1} I(n) - NA] \quad (\text{A10})$$

This results in the maximum likelihood estimator

$$\hat{\mathbf{A}} = \frac{1}{N} \sum_0^{N-1} I(n) \quad (\text{A11})$$

which is simply the mean of I.

## APPENDIX B: MATLAB SIMULATION

### A Plot the simulation in x direction

```
N=500;           % number of steps to take
T=1;            % maximum time
h=T/N;         % time step
t=(0:h:T);     % t is the vector
sigma = 1.0;   % strength of noise

x=zeros(size(t)); % place to store x locations
y=zeros(size(t)); % place to store y locations
z=zeros(size(t)); % place to store z locations
errorZ=zeros(size(t)); % place to store y locations
XYTotalError=zeros(size(t)); % place to store z locations
Sx(1)=0.0;      % initial Sx location
Sy(1)=0.0;      % initial Sy location
Sz(1)=0.0;      % initial Sz location
Zx(1)=0.0;      % initial x location
Zy(1)=0.0;      % initial y location
Zz(1)=0.0;      % initial z location
Ex(1)=0.0;      % initial error in x direction
Ey(1)=0.0;      % initial error in y direction
Ez(1)=0.0;      % initial error in z direction
vx(1)=0.0;      % initial speed in x direction
vy(1)=0.0;      % initial speed in y direction
vz(1)=0.0;      % initial speed in z direction

Sx0=0;
A=500;
B=0.2;
w=5;
wz=500;
Az=500;
x(1)=0.0;      % initial x location
y(1)=0.0;      % initial y location
z(1)=0.0;      % initial z location
for i=1:N      % take N steps
    x(i+1)=x(i)+sigma*h*randn; %Brownian motion in x direction;
    y(i+1)=y(i)+sigma*h*randn; %Brownian motion in y direction;
    z(i+1)=z(i)+sigma*h*randn; %Brownian motion in z direction;

    Sx(i+1)=Sx0+(Sx(i)-Sx0)*exp(-A*h); %r in cylindrical coordinate
    Sy(i+1)=Sy(i)+(w/(2*A))*logm((exp(2*A*h)+B*(Sx(i)-
Sx0)^2)/(1+B*(Sx(i)-Sx0)^2)); %angle in cylindrical coordinate
```



```

Sz(i+1)= Sz(i)+(Sz(i)-Sz0)*exp(-Az*h); %z direction

Zx(i+1)=Sx(i+1)*cos(Sy(i+1))+x(i); %controller in x direction
Zy(i+1)=Sx(i+1)*sin(Sy(i+1))+y(i); %controller in y direction
Zz(i+1)=Sz(i+1)+z(i); %controller in z direction

plot(t, x); % plot Brownian motion in x direction
hold all;
plot(t, Zx); % plot controller motion in x direction

hold off;

end;

grid on % add a grid to axes

```

## B Plot the simulation in y direction

```

N=500; % number of steps to take
T=1; % maximum time
h=T/N; % time step
t=(0:h:T); % t is the vector
sigma = 1.0; % strength of noise

x=zeros(size(t)); % place to store x locations
y=zeros(size(t)); % place to store y locations
z=zeros(size(t)); % place to store z locations
errorZ=zeros(size(t)); % place to store y locations
XYTotalError=zeros(size(t)); % place to store z locations
Sx(1)=0.0; % initial Sx location
Sy(1)=0.0; % initial Sy location
Sz(1)=0.0; % initial Sz location
Zx(1)=0.0; % initial x location
Zy(1)=0.0; % initial y location
Zz(1)=0.0; % initial z location
Ex(1)=0.0; % initial error in x direction
Ey(1)=0.0; % initial error in y direction
Ez(1)=0.0; % initial error in z direction
vx(1)=0.0; % initial speed in x direction
vy(1)=0.0; % initial speed in y direction
vz(1)=0.0; % initial speed in z direction

Sx0=0;
A=500;
B=0.2;
w=5;
wz=500;
Az=500;
x(1)=0.0; % initial x location
y(1)=0.0; % initial y location
z(1)=0.0; % initial z location

```

```

for i=1:N          % take N steps
    x(i+1)=x(i)+sigma*h*randn;    %Brownian motion in x direction;
    y(i+1)=y(i)+sigma*h*randn;    %Brownian motion in y direction;
    z(i+1)=z(i)+sigma*h*randn;    %Brownian motion in z direction;

    Sx(i+1)=Sx0+(Sx(i)-Sx0)*exp(-A*h); %r in cylindrical coordinate
    Sy(i+1)=Sy(i)+(w/(2*A))*logm((exp(2*A*h)+B*(Sx(i)-
Sx0)^2)/(1+B*(Sx(i)-Sx0)^2)); %angle in cylindrical coordinate
    Sz(i+1)= Sz(i)+(Sz(i)-Sz0)*exp(-Az*h); %z direction

    Zx(i+1)=Sx(i+1)*cos(Sy(i+1))+x(i); %controller in x direction
    Zy(i+1)=Sx(i+1)*sin(Sy(i+1))+y(i); %controller in y direction
    Zz(i+1)=Sz(i+1)+z(i); %controller in z direction

    plot(t, y); % plot Brownian motion in y direction
    hold all;
    plot(t, Zy); % plot controller motion in y direction

    hold off;

end;

grid on % add a grid to axes

```

### C Plot the simulation in z direction

```

N=500; % number of steps to take
T=1; % maximum time
h=T/N; % time step
t=(0:h:T); % t is the vector
sigma = 1.0; % strength of noise

x=zeros(size(t)); % place to store x locations
y=zeros(size(t)); % place to store y locations
z=zeros(size(t)); % place to store z locations
errorZ=zeros(size(t)); % place to store y locations
XYTotalError=zeros(size(t)); % place to store z locations
Sx(1)=0.0; % initial Sx location
Sy(1)=0.0; % initial Sy location
Sz(1)=0.0; % initial Sz location
Zx(1)=0.0; % initial x location
Zy(1)=0.0; % initial y location
Zz(1)=0.0; % initial z location
Ex(1)=0.0; % initial error in x direction
Ey(1)=0.0; % initial error in y direction
Ez(1)=0.0; % initial error in z direction
vx(1)=0.0; % initial speed in x direction
vy(1)=0.0; % initial speed in y direction
vz(1)=0.0; % initial speed in z direction

Sx0=0;

```

```

A=500;
B=0.2;
w=5;
wz=500;
Az=500;
x(1)=0.0;           % initial x location
y(1)=0.0;           % initial y location
z(1)=0.0;           % initial z location
for i=1:N            % take N steps
    x(i+1)=x(i)+sigma*h*randn;    %Brownian motion in x direction;
    y(i+1)=y(i)+sigma*h*randn;    %Brownian motion in y direction;
    z(i+1)=z(i)+sigma*h*randn;    %Brownian motion in z direction;

    Sx(i+1)=Sx0+(Sx(i)-Sx0)*exp(-A*h); %r in cylindrical coordinate
    Sy(i+1)=Sy(i)+(w/(2*A))*logm((exp(2*A*h)+B*(Sx(i)-
Sx0)^2)/(1+B*(Sx(i)-Sx0)^2)); %angle in cylindrical coordinate
    Sz(i+1)= Sz(i)+(Sz(i)-Sz0)*exp(-Az*h); %z direction

    Zx(i+1)=Sx(i+1)*cos(Sy(i+1))+x(i); %controller in x direction
    Zy(i+1)=Sx(i+1)*sin(Sy(i+1))+y(i); %controller in y direction
    Zz(i+1)=Sz(i+1)+z(i);           %controller in z direction

    plot(t, z);                    % plot Brownian motion in z direction
    hold all;
    plot(t, Zz);                   % plot controller motion in z direction

    hold off;

end;

grid on                          % add a grid to axes

```

## D Plot the simulation speed in XY plane

```

N=500;                % number of steps to take
T=1;                  % maximum time
h=T/N;                % time step
t=(0:h:T);           % t is the vector
sigma = 1.0;         % strength of noise

x=zeros(size(t));    % place to store x locations
y=zeros(size(t));    % place to store y locations
z=zeros(size(t));    % place to store z locations
errorZ=zeros(size(t)); % place to store y locations
XYTotalError=zeros(size(t)); % place to store z locations
Sx(1)=0.0;           % initial Sx location
Sy(1)=0.0;           % initial Sy location
Sz(1)=0.0;           % initial Sz location
Zx(1)=0.0;           % initial x location
Zy(1)=0.0;           % initial y location
Zz(1)=0.0;           % initial z location
Ex(1)=0.0;           % initial error in x direction
Ey(1)=0.0;           % initial error in y direction

```

```

Ez(1)=0.0;           % initial error in z direction
vx(1)=0.0;          % initial speed in x direction
vy(1)=0.0;          % initial speed in y direction
vz(1)=0.0;          % initial speed in z direction

Sx0=0;
A=500;
B=0.2;
w=5;
wz=500;
Az=500;
x(1)=0.0;           % initial x location
y(1)=0.0;           % initial y location
z(1)=0.0;           % initial z location
for i=1:N            % take N steps
    x(i+1)=x(i)+sigma*h*randn; %Brownian motion in x direction;
    y(i+1)=y(i)+sigma*h*randn; %Brownian motion in y direction;
    z(i+1)=z(i)+sigma*h*randn; %Brownian motion in z direction;

    Sx(i+1)=Sx0+(Sx(i)-Sx0)*exp(-A*h); %r in cylindrical coordinate
    Sy(i+1)=Sy(i)+(w/(2*A))*logm((exp(2*A*h)+B*(Sx(i)-
Sx0)^2)/(1+B*(Sx(i)-Sx0)^2)); %angle in cylindrical coordinate
    Sz(i+1)= Sz(i)+(Sz(i)-Sz0)*exp(-Az*h); %z direction

    Zx(i+1)=Sx(i+1)*cos(Sy(i+1))+x(i); %controller in x direction
    Zy(i+1)=Sx(i+1)*sin(Sy(i+1))+y(i); %controller in y direction
    Zz(i+1)=Sz(i+1)+z(i); %controller in z direction

    vx=(zx(i+1)-zx(i))/h; %speed in x direction
    vy=(zy(i+1)-zy(i))/h; %speed in y direction
    vxy=sqrt(vx^2+vy^2); %speed in XY plane
    vz=(zx(i+1)-zx(i))/h; %speed in z direction

    plot(t, vxy); % plot laser move speed in xy plane

end;

grid on % add a grid to axes

```

## E Plot the simulation in x direction

```

N=500; % number of steps to take
T=1; % maximum time
h=T/N; % time step
t=(0:h:T); % t is the vector
sigma = 1.0; % strength of noise

x=zeros(size(t)); % place to store x locations
y=zeros(size(t)); % place to store y locations
z=zeros(size(t)); % place to store z locations
errorZ=zeros(size(t)); % place to store y locations

```

```

XYTotalError=zeros(size(t)); % place to store z locations
Sx(1)=0.0; % initial Sx location
Sy(1)=0.0; % initial Sy location
Sz(1)=0.0; % initial Sz location
Zx(1)=0.0; % initial x location
Zy(1)=0.0; % initial y location
Zz(1)=0.0; % initial z location
Ex(1)=0.0; % initial error in x direction
Ey(1)=0.0; % initial error in y direction
Ez(1)=0.0; % initial error in z direction
vx(1)=0.0; % initial speed in x direction
vy(1)=0.0; % initial speed in y direction
vz(1)=0.0; % initial speed in z direction

Sx0=0;
A=500;
B=0.2;
w=5;
wz=500;
Az=500;
x(1)=0.0; % initial x location
y(1)=0.0; % initial y location
z(1)=0.0; % initial z location
for i=1:N % take N steps
    x(i+1)=x(i)+sigma*h*randn; %Brownian motion in x direction;
    y(i+1)=y(i)+sigma*h*randn; %Brownian motion in y direction;
    z(i+1)=z(i)+sigma*h*randn; %Brownian motion in z direction;

    Sx(i+1)=Sx0+(Sx(i)-Sx0)*exp(-A*h); %r in cylindrical coordinate
    Sy(i+1)=Sy(i)+(w/(2*A))*logm((exp(2*A*h)+B*(Sx(i)-
Sx0)^2)/(1+B*(Sx(i)-Sx0)^2)); %angle in cylindrical coordinate
    Sz(i+1)= Sz(i)+(Sz(i)-Sz0)*exp(-Az*h); %z direction

    Zx(i+1)=Sx(i+1)*cos(Sy(i+1))+x(i); %controller in x direction
    Zy(i+1)=Sx(i+1)*sin(Sy(i+1))+y(i); %controller in y direction
    Zz(i+1)=Sz(i+1)+z(i); %controller in z direction

    vx=(zx(i+1)-zx(i))/h; %speed in x direction
    vy=(zy(i+1)-zy(i))/h; %speed in y direction
    vz=(zz(i+1)-zz(i))/h; %speed in z direction

    plot(t, vz); % plot stage speed in z direction

end;

grid on % add a grid to axes

```

## F Plot the simulation error in XY plane

```

N=500;           % number of steps to take
T=1;            % maximum time
h=T/N;         % time step
t=(0:h:T);     % t is the vector
sigma = 1.0;   % strength of noise

x=zeros(size(t)); % place to store x locations
y=zeros(size(t)); % place to store y locations
z=zeros(size(t)); % place to store z locations
errorZ=zeros(size(t)); % place to store y locations
XYTotalError=zeros(size(t)); % place to store z locations
Sx(1)=0.0;      % initial Sx location
Sy(1)=0.0;      % initial Sy location
Sz(1)=0.0;      % initial Sz location
Zx(1)=0.0;      % initial x location
Zy(1)=0.0;      % initial y location
Zz(1)=0.0;      % initial z location
Ex(1)=0.0;      % initial error in x direction
Ey(1)=0.0;      % initial error in y direction
Ez(1)=0.0;      % initial error in z direction
vx(1)=0.0;      % initial speed in x direction
vy(1)=0.0;      % initial speed in y direction
vz(1)=0.0;      % initial speed in z direction

Sx0=0;
A=500;
B=0.2;
w=5;
wz=500;
Az=500;
x(1)=0.0;      % initial x location
y(1)=0.0;      % initial y location
z(1)=0.0;      % initial z location
for i=1:N      % take N steps
    x(i+1)=x(i)+sigma*h*randn; %Brownian motion in x direction;
    y(i+1)=y(i)+sigma*h*randn; %Brownian motion in y direction;
    z(i+1)=z(i)+sigma*h*randn; %Brownian motion in z direction;

    Sx(i+1)=Sx0+(Sx(i)-Sx0)*exp(-A*h); %r in cylindrical coordinate
    Sy(i+1)=Sy(i)+(w/(2*A))*logm((exp(2*A*h)+B*(Sx(i)-
Sx0)^2)/(1+B*(Sx(i)-Sx0)^2)); %angle in cylindrical coordinate
    Sz(i+1)= Sz(i)+(Sz(i)-Sz0)*exp(-Az*h); %z direction

    Zx(i+1)=Sx(i+1)*cos(Sy(i+1))+x(i); %controller in x direction
    Zy(i+1)=Sx(i+1)*sin(Sy(i+1))+y(i); %controller in y direction
    Zz(i+1)=Sz(i+1)+z(i); %controller in z direction

    Ex(i+1)=abs(Zx(i+1)-x(i+1)); %error in x direction
    Ey(i+1)=abs(Zy(i+1)-y(i+1)); %error in y direction
    Ez(i+1)=abs(Zz(i+1)-z(i+1)); %error in z direction
end

```

```

        XYTotalError(i+1)=(Zx(i+1)*Ex(i+1)+Zy(i+1)*Ey(i+1)); error in XY
Plane

        plot(t,XYTotalError);          % plot XY plane total error

end;

grid on                                % add a grid to axes

```

## G Plot the simulation error in z direction

```

N=500;                                % number of steps to take
T=1;                                   % maximum time
h=T/N;                                 % time step
t=(0:h:T);                             % t is the vector
sigma = 1.0;                           % strength of noise

x=zeros(size(t));                      % place to store x locations
y=zeros(size(t));                      % place to store y locations
z=zeros(size(t));                      % place to store z locations
errorZ=zeros(size(t));                 % place to store y locations
XYTotalError=zeros(size(t));          % place to store z locations
Sx(1)=0.0;                             % initial Sx location
Sy(1)=0.0;                             % initial Sy location
Sz(1)=0.0;                             % initial Sz location
Zx(1)=0.0;                             % initial x location
Zy(1)=0.0;                             % initial y location
Zz(1)=0.0;                             % initial z location
Ex(1)=0.0;                             % initial error in x direction
Ey(1)=0.0;                             % initial error in y direction
Ez(1)=0.0;                             % initial error in z direction
vx(1)=0.0;                             % initial speed in x direction
vy(1)=0.0;                             % initial speed in y direction
vz(1)=0.0;                             % initial speed in z direction

Sx0=0;
A=500;
B=0.2;
w=5;
wz=500;
Az=500;
x(1)=0.0;                              % initial x location
y(1)=0.0;                              % initial y location
z(1)=0.0;                              % initial z location
for i=1:N                                % take N steps
    x(i+1)=x(i)+sigma*h*randn;          %Brownian motion in x direction;
    y(i+1)=y(i)+sigma*h*randn;          %Brownian motion in y direction;
    z(i+1)=z(i)+sigma*h*randn;          %Brownian motion in z direction;
end

```

```

    Sx(i+1)=Sx0+(Sx(i)-Sx0)*exp(-A*h); %r in cylindrical coordinate
    Sy(i+1)=Sy(i)+(w/(2*A))*logm((exp(2*A*h)+B*(Sx(i)-
Sx0)^2)/(1+B*(Sx(i)-Sx0)^2)); %angle in cylindrical coordinate
    Sz(i+1)= Sz(i)+(Sz(i)-Sz0)*exp(-Az*h); %z direction

    Zx(i+1)=Sx(i+1)*cos(Sy(i+1))+x(i); %controller in x direction
    Zy(i+1)=Sx(i+1)*sin(Sy(i+1))+y(i); %controller in y direction
    Zz(i+1)=Sz(i+1)+z(i); %controller in z direction

    vx=(zx(i+1)-zx(i))/h; %speed in x direction
    vy=(zy(i+1)-zy(i))/h; %speed in y direction
    vz=(zz(i+1)-zz(i))/h; %speed in z direction

    Ex(i+1)=abs(Zx(i+1)-x(i+1)); %error in x direction
    Ey(i+1)=abs(Zy(i+1)-y(i+1)); %error in y direction
    Ez(i+1)=abs(Zz(i+1)-z(i+1)); %error in z direction

    plot(t,Ez); % plot error in z direction

end;

grid on % add a grid to axes

```